Food-Sorting Jet Arrays And Target Impact Properties

Paul Edward Westwood

University College London

University of London

A thesis submitted for the degree of

Doctor of Philosophy

Supervisor: Professor F. T. Smith, FRS

February 2005

ProQuest LLC
789 East Eisenhower Parkway
P.O. Box 1346
Ann Arbor, MI 48106-1346

To my son, Josh

- an apology to a little boy who has, over the past few years, learnt to dislike mathematics.

Abstract

This thesis uses numerical techniques and analysis to study the development and interactions between multiple in-line slender air jets. Consideration is given to two- and three-dimensional flow regimes, but the emphasis is on the latter. The applications (and mechanisms) involved in high-speed machine sorting of small food items, such as grains of rice, are explained. The underpinning mathematics required to develop the mathematical model are stated. In Chapter 2 an analytical solution for the two-dimensional steady jet is demonstrated and used to provide a far-downstream asymptote for validation of the numerical scheme, for steady and unsteady jets. A numerical scheme is demonstrated to be versatile and reasonably accurate. Small-distance analysis complements the numerical scheme and limitations are discussed. A comprehensive small-time analysis is undertaken, results from which support later work on three-dimensional jets. Interference between in-line jets is considered in Chapter 3, which applies methods previously used to study two-dimensional in-parallel wakes. The conclusions from this chapter support and help explain results in later chapters. The numerical scheme is extended to three-dimensional steady and unsteady jets. Issuing nozzles of various cross-sections are considered with the aim of obtaining pressure data for comparison with physical data. Small-distance analysis is again investigated, enabling a weakness in the numerical solution to be highlighted. Potential flow theory is used to model interference aspects of multiple in-line unsteady three-dimensional jets. The emphasis is placed on jets from nozzles

of either circular or rectangular cross-section but, in fact, the analysis applies for any cross-section. The impact properties of a typical jet when it hits one of the particles such as a grain of rice being sorted are discussed briefly, and final comments are made.

Acknowledgements

I would like to express my sincere thanks to many people. In particular, I am indebted to the following members of Keele University Mathematics Department. Professor Graham Wilks and Dr. Jonathan Healey who were instrumental in introducing me to my supervisor and who gave me a favourable recommendation; Professor Andrew Willmott and Dr. John Chapman whose enthusiasm for mathematics and eagerness to help me will always be remembered and much appreciated and, finally, my good friend Mr Andrew Looms, for the times he rescued me computationally.

This research was funded by the Engineering and Physical Science Research Council and Sortex Ltd of London (by way of The Smith Institute, Faraday Partnership). I am grateful to these bodies for their financial support and for the interaction and guidance they gave throughout. Notably, I would like to thank Dr. Mark Honeywood and Dr. Sarah Bee of Sortex for helping to direct the project.

Throughout the course of this research I have encountered periods marked by tremendous highs accompanied by feelings of great personal achievement. At these times my supervisor, Professor Frank Smith, shared in my delight but kept my feet firmly on the ground. At other times, when I experienced what seemed like insurmountable difficulties his, often jovial and always wise, words of encouragement picked me up and spurred me on. His enthusiasm was contagious, his insight and understanding astounding (and often frightening) and his friendship one that I will truly treasure for the rest of my life. Thank you Frank, for all that you have done for me.

Contents

1 Introduction 8

1.1 Overview of sorting technology 8

1.2 Governing equations 18

1.2.1 Newton's law of viscosity 18

1.2.2 Reynolds number 19

1.2.3 Continuity equation 20

1.2.4 Navier-Stokes equations 22

1.2.5 The boundary layer and the jet 23

1.2.6 Sortex jets 25

1.2.7 Boundary layer equations 26

2 Two-dimensional Jets 28

2.1 Similarity solution (steady symmetric jet) 28

2.2 Numerical solution (steady jet) 32

2.2.1 Introduction 32

2.2.2 Semi-implicit finite difference model for the two-dimensional steady jet 33

2.2.3 Testing the scheme 36

2.2.4 Non-symmetric steady two-dimensional jet 40
2.3 Small-distance analysis 43
2.3.1 Analysis of a simple spread-out initial profile 44
2.3.2 Analysis of a smoothed 'unit-pulse' profile 47
2.3.3 Lock's solution to the free-shear layer problem 50
2.4 Pressure calculation 53
2.5 Small-time analysis of the unsteady jet 55
2.5.1 Jet velocity 59
2.5.2 Jet shape 60
2.5.3 Viscous effects 63
2.6 Summary 66

3 Interference Between Steady in-line Jets 68
3.1 Introduction 68
3.2 Numerical investigation 69
3.3 Analysing the numerical results 72
3.4 Small-x analysis 73
3.5 Summary 73

4 Three-Dimensional Steady Jets 75
4.1 Introduction 75
4.2 Governing equations 76
4.3 Numerical solution 80
4.3.1 Gauss-Jacobi iterative scheme 81
4.3.2 Solution of the three-dimensional jet 82
4.4 Validation of the numerical scheme 84

4.5 Leading order small-x analysis of a smooth initial profile . . . 87
4.6 Obtaining the pressure equation 89
4.7 Small-distance analysis 92
4.7.1 Boundary conditions 95
4.8 Cross-planar stream function formulation for three-dimensional jets 97
4.9 Swirl 102
4.10 Non-square rectangular jets 106
4.11 Summary 108

5 Three-Dimensional Unsteady Jets 110

5.1 Introduction 110
5.2 Governing equations 110
5.3 Numerical solution 113
5.4 The pressure equation 114
5.5 Physical pressure data 115
5.6 Comparing numerical solutions with physical test data 118
5.7 Summary 119

6 Interference in three-dimensional Jets 120

6.1 Introduction 120
6.2 Potential flow solution of the steady rectangular discontinuous case 122
6.3 The axisymmetric case and far-field conditions 124
6.3.1 Comparison of cross-flow prediction with numerical solution of smooth profiles 127

6.4 Multiple in-line steady rectangular jets 129
6.5 In-parallel steady round jets 138
6.6 Comparing steady rectangular and round jet solutions 139
6.7 Unsteady round jets 143
6.8 Unsteady rectangular jets 147
6.8.1 Effects of unsteady firing 148
6.8.2 Inter-nozzle spacing effects 150
6.9 Summary 153

7 Target Impact Properties **155**
7.1 Impact by a horizontal jet 157
7.2 Impact by an inclined jet 159
7.3 Comparison with physical study 161
7.4 Summary 163

8 Summary **164**

Appendices **170**

A Examples of Interference Between Round Jets **171**

B Interference Between Rectangular Jets **176**

List of Figures

1.1 Schematic view of a typical sorting machine taken from an illustration by Sortex Ltd. 10

2.1 half profile for $u_0 = sech(y)$ at stations $x = 0.1, 1.0, 10.0$. . . . 37

2.2 Streamwise velocity at a fixed x-station for varying Δy. 38

2.3 Streamwise velocity at a fixed x-station for varying Δx. 39

2.4 Simulation of two jets merging downstream 40

2.5 Symmetric (ideal)case. 41

2.6 Non-symmetric case. 41

2.7 centreline velocity at x = 0.005 45

2.8 centreline velocity at x = 0.05 46

2.9 centreline velocity at x = 0.1 47

2.10 comparison of numerical and small-x solution at $x = 0.0005$ for $N = 10$. 48

2.11 comparison of numerical and small-x solution at $x = 0.005$ for $N = 10$. 49

2.12 comparison of numerical and small-x solution at $x = 0.01$ for $N = 10$. 49

2.13 revised smoothed unit-pulse problem. 51

2.14 X against U, $D_2 = 0$. 57

2.15 X against U, $D_2 > 0$. 58

2.16 X against U, $D_2 < 0$. 58

2.17 U against X. Upstream $(0 < X < X_1)$: $U(0) = b$.
Downstream $(X > X_1)$: $U \equiv 0$. 59

2.18 The jet's velocity decreases to a minimum value of $2X_{max}$. . . 60

2.19 slender jet (symmetric about x-axis). 62

2.20 inviscid jet 'blow-up'. 62

2.21 inviscid jet and Euler region. 63

2.22 Viscous layer. 66

3.1 Schematic of full $3D$ ejector set-up. 68

3.2 $u_0 = \left[1 + \left(6\sin\left(\frac{y}{2}\right)\right)^2\right]^{-1}$, $-9\pi \leq y \leq 9\pi$, $x = 0, 0.1, 0.5$. . . . 70

3.3 $u_0 = \left[1 + \left(6\sin\left(\frac{y}{2}\right)\right)^2\right]^{-1}$, $-9\pi \leq y \leq 9\pi$, $x = 0.8, 1.6, 3.0, 4.0$. 71

3.4 ψ_1 vs y for $u_0 = \frac{1}{(1+(6\sin(\frac{y}{2}))^2)}$, $0 \leq y \leq N$, $N = 9\pi$. 72

3.5 u_1 vs y for $u_0 = \frac{1}{(1+6\sin^2(\frac{y}{2}))}$, $0 \leq y \leq N$, $N = 9\pi$. 73

4.1 Maximum gauge pressures between 2.5mm and 15mm from the nozzle exit supplied by Sortex. 76

4.2 Fixed solution domain, increasing Δy and Δz at prescribed x-station. Horizontal axis gives Δy and Δz values; vertical axis gives centreline velocity. 85

4.3 Fixed solution domain, increasing Δx at prescribed x-station. 85

4.4 centreline velocities produced by refining Δy and Δz. 86

4.5 comparison of numerical solution with analytical solution at small x for relatively smooth initial profile 88

4.6 Non-dimensional centre-line pressure curve produced by the numerical solution with a smoothed unit-pulse initial profile. . 91

4.7 Contour plot of ψ in the y, z plane. 99

4.8 Contour plot of v_0 (on the left) and Contour plot of w_0 (on the right). 100

4.9 Dimensionalized centreline pressure up to 15mm from exit. . . 101

4.10 Dimensionalized pressure comparison at discrete points up to 15mm from exit. 102

4.11 v velocity components ten steps downstream. (No induced swirl). 103

4.12 v velocity components ten steps downstream.(Swirl given by $v_0 = \frac{z}{r^2}$, $w_0 = \frac{-y}{r^2}$). 104

4.13 Comparison of centreline velocity with and without swirl. . . . 105

4.14 Comparison of centreline pressure with and without swirl. . . 105

4.15 Pressure solutions for a square unit-pulse initial profile at $x = 150mm$. 106

4.16 Pressure solutions for a square unit-pulse initial profile at $x = 150mm$, arbitrary swirl imposed. 106

4.17 Streamwise velocity profiles with and without swirl at x = 25mm. 107

4.18 Pressure profiles with and without swirl. 108

5.1 Maximum pressure values recorded at 2.5mm intervals along the flow for three distinct samples, at four different times. . . 116

5.2 Contour plots of pressure data recorded at 3 milliseconds on 10mm x 10mm (y,z) planes. Highest values are white, lowest values are black. 117

5.3 Maximum pressure values at t = 3ms, recorded at 2.5mm intervals along the flow 118

6.1 Effect on crossflow as u_0 approaches discontinuous case. 121

6.2 Potential flow problem specification, shown for a rectangular nozzle. C is the core-edge, on which the jump condition must be satisfied. 123

6.3 ϕ vs y $(z = 0)$ at various Δy, ∞ fixed at ± 6. 124

6.4 $\phi vs\, y(z = 0)$ for various Δy, ∞ fixed at ± 6, far-field conditions given by $\phi = -n \ln r + k$. 126

6.5 Normalised crossflow results for smooth cases. 128

6.6 Comparison of crossflow prediction from smooth result at large n with potential flow solution. 129

6.7 Comparison of v against r and asymptote c/r at $\theta = \pi$ (square nozzle). 130

6.8 Comparison of v against r and asymptote c/r at $\theta = \pi$ (rectangular nozzle). 131

6.9 Comparison of v against r and asymptote c/r at $\theta = 3\pi/4$ (square nozzle). 132

6.10 v dependence on θ, θ measured clockwise. 133

6.11 Comparison of v against r and asymptote at $\theta = 3\pi/4$ with θ correction. 134

6.12 Contour plots of (restricted solution domain) potential flow solution for 1x1mm and 3x1mm nozzles and solutions with extrapolated data placed in larger arrays. 135

6.13 Crossflow solutions for steady jets issuing from 3x1mm nozzles. 137

6.14 Solution for a single round jet with $k = -10$. 140

6.15 Multiple steady round jet examples. $k = -10$. 141

6.16 (Top) single square jet and single round jet crossflow solutions. (Bottom) Comparison of crossflow solutions for five neighbouring square jets and five neighbouring round jets. 142

6.17 Crossflow predictions for two unsteady jets of 2mm diameter, separated by 0.5mm gap and lag = 0.5, at various times over complete solution cycle. 145

6.18 Example of a single unsteady rectangular jet developing subject to condition ??. 148

6.19 Two jets issuing from 3x1mm nozzles subject to a time-lag of 0.3 and separated by 0.5mm gaps 149

6.20 Two unsteady 3x1mm jets separated by a 1mm gap and time-lag of 0.3. The ringed areas highlight the 'inter-jet region'.. . . 151

7.1 Above: typical Sortex ejector nozzles. Below: Jet impact with rice (particle). 156

7.2 Horizontal velocity of grain v m/s plotted against jet speed on impact W m/s. 159

7.3 Angle of deflection from vertical downward direction against angle of jet inclination α (scales are in radians). 160

7.4 Schematic of a typical particle deflection test set-up. 162

A.1 Eight round jets with firing order: 4, 1, 2, 8, 3, 5, 7, 6 and time lags: 0.1, 0.2, 0.4, 0.6, 0.7, 0.9, 1.2, respectively. 172

A.2 (Top) two neighbouring steady jets. (Bottom) two steady jets, separated by an intermediate nozzle. 173

A.3 (Top) three steady jets at positions 1, 2 and 4. (Bottom) three steady jets at positions 1, 2 and 5. 174

A.4 (Top) four steady jets at positions 1, 2, 3 and 4. (Bottom) four steady jets at positions 1, 2, 4 and 5. 175

B.1 4x1mm jets separated by 0.5mm gaps. Jets 3, 2, 4 fired at t = 0, t = 0.2 and t = 0.5, respectively (illustration up to t = 0.6). 177

B.2 4x1mm jets separated by 0.5mm gaps. Jets 3, 2, 4 fired at t = 0, t = 0.2 and t = 0.5, respectively (illustration from t = 0.6 to t = 1.3). 178

B.3 6x1mm jets separated by 0.5mm gaps. Jets 1, 2, 3 fired at t = 0, t = 0.1 and t = 0.3, respectively (illustration up to t = 0.6). 179

B.4 6x1mm jets separated by 0.5mm gaps. Jets 1, 2, 3 fired at t = 0, t = 0.1 and t = 0.3, respectively (illustration from t = 0.6 to t = 1.2). 180

Chapter 1

Introduction

This thesis is concerned with the relatively rapid flow of a thin jet of slightly viscous fluid, or an array of such jets, and the industrial application to food sorting in particular. The research was motivated by a need within the food-sorting industry to better understand the **interference** aspects associated with multiple in-line slender air jets. The jets issue from rectangular nozzles of 3x1mm, 4x1mm or 6x1mm cross-sectional dimensions, typically, and operate over a 150mm range in the axial direction of the jet. Results from the research will be used to help guide future design considerations prior to manufacturing new generations of sorting-machines.

1.1 Overview of sorting technology

Food sorting, like most other industrial sorting, was primarily done by hand and eye until relatively recently; that is until around 1930, when the first automated colour-sorting machines were developed by Westinghouse in the

USA (see [30]).

Over a comparatively short period of time, the need to maximize profitability led to rapid advances in technology and machines employing air-jets, capable of sorting larger and larger quantities of products, were developed. The technology used in these machines has built on the pioneering research of Norris [31] and Schaub [32] and continues to improve. Today's sorting machines are capable of sorting up to twelve tons of produce every hour (the figure quoted refers to the Sortex 90000 series sorting machine when sorting rice). These modern machines still combine visual inspection and targeted response as the method of sorting; however they are capable of viewing the product from all sides simultaneously, and can eject unwanted items in milliseconds.

The machine sorting process generally follows the format outlined in [30], namely: feed and spread; accelerate; illuminate and view; classify and finally eject or accept.

Referring to figure 1.1, the produce is introduced to the machine via a vibrating hopper. This helps to spread the produce, for example rice grains or coffee beans, across the entire width of the machine's feed chute so that it is, ultimately, in a single uniform layer. These particles then fall down a gravity chute so that they accelerate to a high velocity before entering the viewing area; whereupon they are illuminated evenly by high-intensity fluorescent lamps and viewed from different angles by two or three cameras. Optical filters placed in front of the cameras allow only selected wavelengths to pass through. Undesirable items are identified by selectively comparing the mag-

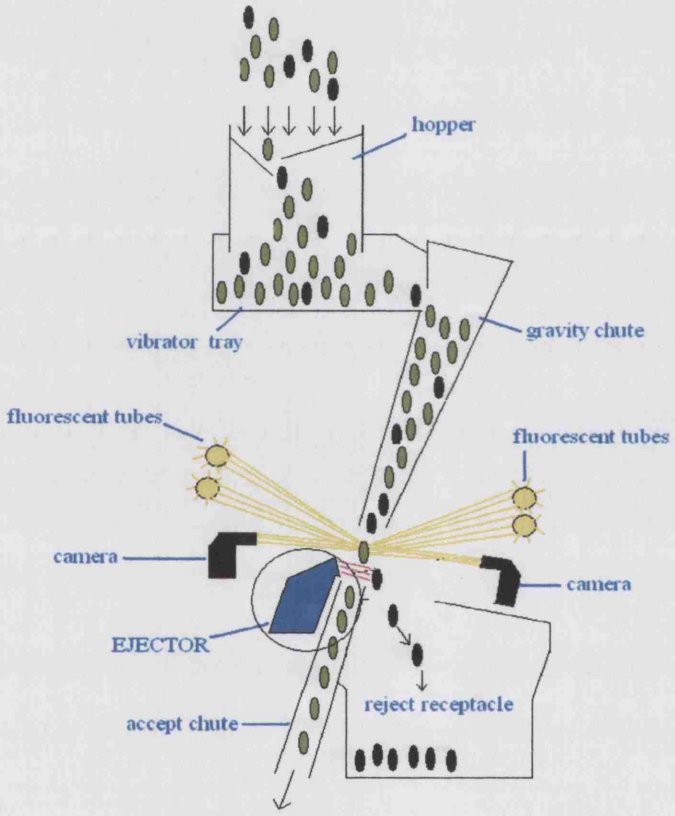

Figure 1.1: Schematic view of a typical sorting machine taken from an illustration by Sortex Ltd.

nitudes of reflected light at particular wavelengths. The reflected light from each particle of the product is measured and compared to an index in order to determine whether it should be accepted or rejected.

Once a particle has been identified for rejection an electronic signal activates an ejector, which releases a blast of air as the particle passes by. The timing of the ejector's firing assumes that the product is moving with constant velocity. Ejected particles are knocked beyond a separation plate and into a reject receptacle.

Clearly, based on the volume throughput quoted, today's sorting machines are highly advanced and appear to be extremely efficient. However, the sorting processes outlined above portray an ideal scenario which, in practice, is virtually unattainable. For instance, it can never be guaranteed that the particles being sorted will enter the viewing area in a single uniform layer with each particle travelling at precisely the same velocity. Furthermore, the processing of such large volumes requires the machine's ejectors to fire in response to defective particles hundreds of times every second. The spread of the air-jets coupled with the close proximity with which the particles fall in relation to one another invariably means that particles other than the actual target particle will also be affected by the air blast and hence rejected particles from a single batch of produce may have to be re-sorted several times.

Improvements to machine design to enable sort-rates to increase still further necessarily require an 'optimized' particle delivery system and a reduction in

the number of good particles being wrongly ejected. Of central importance to both of these is an understanding of the impacting properties and the evolution and interference between the fluid jets. Neve, Nelson and Kotsiopolous [2] and Neve and Kotsiopoulos [3] have studied the deflecting force (drag) associated with spherical objects subjected to thin air jets. Neve [33] has considered impacting properties of circular and rectangular jets on spherical and cylindrical targets, respectively, and results from [33] may be used to draft design guidelines based on the deflecting force predicted for particles that approximate the shapes of these two cases. There are also huge bodies of literature on turbulent flow in jets (see, for instance, [40], [41], [42], all of which address the effects of turbulence on drag; [43, pp 39-73], which discusses similarity forms and their limitations regarding turbulent jets; and [44], which provides an excellent reference for the general study of turbulent flow) and on laminar-turbulent transition in jets (see, for instance, [48], [49]). In contrast, there appears to be very little work related directly to interference between in-line jets apart from the research on interference between in-line wakes described by Smith [9].

In later work [34], [35], Neve used a CFD approach to produce velocity predictions for a limited number of neighbouring jets in the Sortex 90000 series machine. In these reports he assumed that the flow of fluid within the ducts feeding the jets would be laminar, producing fully developed parabolic initial jet profiles with an exit velocity of $20m/s$. He concluded from his results that there would be a significant increase in jet width in the target area compared to initial jet width; that the amount of momentum flux residing

in the target area after the initial impact would be enough to deflect the next one or two particles arriving there; that, in terms of centreline velocity, individual jets are, to a great extent, not affected by their neighbours and that, to a first approximation, the jets' velocity profiles in the target area could be obtained by adding together profiles for individual jets.

At the same time that Neve was working on the external jet flow mentioned above, Smith, [19], [20], investigated the internal steady and unsteady flow solutions through the complex slender ducts of the ejector for the same sorting machine. The aims were to predict the jet velocity and shape at the nozzle exit for the current duct geometry and input pressure and then for modified geometries and input pressures, so that recommendations could be made which would improve sorting efficiency. It is found in Smith's work that a smooth parabolic exit velocity profile is not achievable with the current duct set-up nor, indeed, with an ideal duct set-up; in that case the exit velocity profile tends towards a 'smoothed unit-pulse' or 'top-hat'. Furthermore, with the current duct geometry the exit velocity profile is skewed and misdirected and this, therefore, could have implications regarding the applicability of Neve's results, particularly close to the nozzle exit. Smith recommends that the bends in the ducting should be minimized in order to reduce the skewing and misdirection of the developing jet. Straightening, shortening or narrowing the duct is also beneficial, increasing the exit velocity.

The present thesis explores the development and interactions of closely packed

multiple independent in-line slender air jets as they emerge and develop from an array of rectangular ducts. The study is believed to have direct industrial significance, as the above is precisely the situation that exists in the food-sorting machines mentioned earlier. Clearly, in light of [19] and [20], the 'top-hat' case is of central importance, as this represents an ideal scenario, even though at present in the industrial setting the nozzle velocity profiles are almost certainly quite various and nonuniform, as reported in [19], [20] and [22]. A main emphasis throughout the thesis will be on **interference**, which results from the interactions between the jets as they suck (entrain) fluid from their environs and in particular their neighbours, in order to sustain themselves.

We will assume throughout that the fluid being studied is effectively incompressible, and note that the complete model will necessarily be three-dimensional and unsteady. We begin however, in Chapter 2, by considering a similarity solution for a single steady incompressible two-dimensional jet (see, for example, [15, pp 344], [25] and [6, pp 112]) which is symmetrical about its central axis, and which will be used as a far-downstream asymptote for the numerical investigation of the same or similar cases. The numerical solution is achieved by using a semi-implicit finite-difference scheme as in [21], which is solved employing a tri-diagonal matrix algorithm described in [36]. Adjustments to the numerical scheme necessary to accommodate non-symmetric initial profiles are also briefly discussed.

The constraints imposed on the jets by the physical aspects of the sorting

machines, as described later in 1.2.6, suggest small-distance analysis should be considered. This is done for both the 'smooth' and 'non-smooth' cases, i.e. for jets developing from smooth spread-out initial profiles such as the fully developed parabolic initial profiles considered by Neve [34], [35] and those developing from near-discontinuous 'top-hat' initial profiles, predicted by Smith [19], [20]. The analysis is shown to provide an excellent complement to the numerical solution of jets developing from smooth initial profiles. However, it is found to be generally inappropriate for non-smooth cases since, as the limiting case of a discontinuous initial profile is approached, a Blasius-type free-shear layer develops which cannot be resolved by leading-order analysis. Three distinct regions then exist and Lock's solution (see [7]) is required to solve for the free-shear layer region.

Chapter 2 concludes with a comprehensive small-time analysis of the two-dimensional unsteady jet, which combined with the analysis just described gives a great deal of insight into the steady and unsteady three-dimensional jets discussed in later chapters.

Chapter 3 applies the numerical and analytical methods described in Chapter 2 to investigate interference between close-neighbouring jets. In a similar study [9], Smith was able to demonstrate that even if the initial streamwise velocity profile of in-line wakes is periodic the lateral velocity components will be non-zero and non-periodic. This result is mirrored in the current study of jets. Edge effects are also seen to play a 'nontrivial' role in the interference. Results from the current chapter have clear implications in later chapters.

In Chapter 4 we consider three-dimensional jets issuing from rectangular nozzles. The governing equations as derived from the three-dimensional Navier-Stokes momentum equations are stated and then solved using what is essentially a vorticity-velocity formulation. The numerical solution of Chapter 2 is supplemented with a Gauss-Jacobi iterative scheme to solve for the lateral velocity components, and this is shown to provide a reasonably accurate approximate solution. Leading order small-distance analysis is found, once again, to provide a helpful complement to the numerical solution when considering relatively smooth initial profiles. The pressure equation is next derived and solved using the same type of iterative process as above. A weakness in the numerical solution at small axial (streamwise) distances x, which is explained by the earlier two-dimensional small-distance analysis, is discussed and an attempt to overcome this using further small-distance analysis of the lateral velocity components and a cross-planar stream function formulation is made. Although unsuccessful, the analysis seems to provide some insight and proves to be of benefit to the later study of interference.

By making the streamwise grid step smaller, numerical pressure data is captured close enough to the nozzle exit for a comparison with the physical data in [38] to be made, and the results are shown to be in good agreement. Imposed swirl is also considered and is shown to have very little effect on the jet's development. However, the swirl does appear to help concentrate the jet's pressure into a narrower band surrounding the central streamwise axis.

Time-dependence is considered in Chapter 5, where pressure comparisons

are made with data supplied by Sortex Ltd [39] for a variety of times and at various distances from the issuing nozzle.

Chapter 6 investigates the major issue of interference between multiple in-line three-dimensional jets. By considering small-distance analysis for the case of an irrotational (zero-swirl) smooth three-dimensional incident flow we are able to better understand what happens to the lateral velocity components as the initial velocity profile is transformed (by means of adjustment of a particular parameter) from being very smooth to being near-discontinuous. It is shown, in agreement with the earlier small-distance analysis of the two-dimensional case, that the cross-flow grows massively as the discontinuous 'top-hat' scenario is approached through variation of the above parameter. A defining characteristic of the discontinuous case is that the streamwise velocity component, u, is constant both within the jet's core region and without, making potential flow theory applicable both within and without; this is subject to a jump condition on the core-edge of the jet which is given by the small-distance analysis. The potential-flow-like property of the single jet solution is of much importance to our study of multiple close-neighbouring similar jets since it means that, once the solution for a single jet has been obtained, that solution can be added linearly (subject to a displacement of its axis) to provide the solution for the many jet case. This elegant and powerful result is equally applicable to jets of any cross-section and this fact is used here to demonstrate interference aspects of various different rectangular and circular, steady and unsteady jets.

Chapter 7 gives a simple and brief exposition of the overall target impact properties. A summary of the main points of each chapter is then given in Chapter 8 along with recommendations for possible sorting-jet design improvements and further research. To the best of our knowledge, the majority of the study in all of chapters 2 - 7 is novel work.

In the remainder of our first chapter we present the underpinning mathematics used to construct the mathematical model developed throughout the remainder of the thesis.

1.2 Governing equations

Fundamental to the study of fluid mechanics in general are certain underlying principles, which are described by most texts in much the same manner. We refer the reader to the following: [1], [4], [11], [12], [13], which, amongst other texts, have been consulted and which we suggest provide a clear but perhaps fuller explanation of the subject matter in sections 1.2.1 through 1.2.3.

1.2.1 Newton's law of viscosity

All fluids are characterized by an inability to resist shear; that is to say, they deform continuously while under the influence of an applied force. If one considers an arbitrary control volume of fluid, which has a shearing force applied to one surface, then the force per unit area is referred to as the *shear stress*, τ, and the angle ϕ, by which the control volume deforms while the force is applied, is referred to as the *shear strain*. ϕ increases continuously

while τ is applied, as a result of which the fluid flows.

Not all fluids flow at the same rate relative to the same shearing force however; and the measure of a fluid's resistance to shear, when in motion, is called the viscosity of the fluid. In a simplistic sense, consider a fluid particle at some maintained height, y, above the base of the above control volume, and which travels a horizontal distance x, say, with the flow while a shearing force is applied. Then small values of ϕ are approximately equal to x/y and, therefore, the rate of shear strain ϕ/t is approximately $(x/y)/t$ or $(x/t)/y$, which is the rate of change of velocity of the particle with respect to y. This is consistent with the relation

$$\tau = \mu \frac{du}{dy} \tag{1.1}$$

where μ is the constant of proportionality referred to as *dynamic viscosity.* Fluids which obey (1.1), for instance air, are termed *Newtonian fluids.*

We note, choosing basic dimensions M (Mass), L (Length) and T (Time), since τ is equal to the applied force per unit area divided by the velocity of the fluid particle per unit distance travelled, that μ has dimension M/LT.

1.2.2 Reynolds number

In 1883, Osborne Reynolds [5] demonstrated that two completely different kinds of fluid flow can exist. Generally, at small velocities the particles within a volume of fluid will tend to flow smoothly, maintaining the same relative positions in successive cross-sections of fluid. This is often termed *laminar,*

viscous or *streamlined* flow. Beyond a critical velocity fluid particles move in a less orderly fashion, occupying different relative positions in successive cross-sections of the fluid. This is referred to as *turbulent* flow since it is characterized by continuous fluctuations in the magnitude and direction of the velocity of the fluid particles, accompanied by fluctuations in pressure.

In viscous-dominated flows the viscous shear stresses that exist between neighbouring particles are sufficient to balance any inertial effects caused by applied disturbances and so the motion remains uniform. However, in turbulent flows the viscous forces are weaker and are unable to overcome the induced inertial forces, resulting in chaotic motion. Clearly then, it is the ratio of inertial forces to viscous forces that (among other factors) helps determine whether a particular flow is laminar or turbulent.

Considering Newton's second law of motion, i.e. that inertial force is equal to the product of a body's mass and its acceleration, it follows that inertial force can be represented dimensionally as $\rho L^4/T^2$, where ρ is mass density. Similarly, the viscous force is equal to the viscous shear stress multiplied by the area on which this acts. Hence viscous force may be represented as $\mu L^2/T$. Therefore, the ratio of inertial forces to viscous forces is $\frac{\rho UL}{\mu}$, and this is a pure number (since it is the ratio of two forces) known as the Reynolds number, which we will denote by Re.

1.2.3 Continuity equation

Conservation of mass requires that the nett flow of fluid out of a control volume in unit time must be equal to the change in mass within the control volume in unit time. Therefore, considering an arbitrary but small volume of fluid of dimensions δx, δy, δz, relative to the Cartesian coordinates x, y, z, with corresponding velocity components u, v, w, the flow of fluid into the control volume in the x-direction is equal to the mass of flow into the control volume in the x-direction in unit time, which equals $\rho u \delta y \delta z$. Since the mass density and velocity may vary in the direction of flow, the nett outflow of fluid in the x-direction will be $\frac{\partial(\rho u)}{\partial x}\delta x \delta y \delta z$, to leading order. Similar expressions apply in the y and z directions, and it follows that the nett outflow in unit time is given by: $\{\frac{\partial(\rho u)}{\partial x} + \frac{\partial(\rho v)}{\partial y} + \frac{\partial(\rho w)}{\partial z}\}\delta x \delta y \delta z$. This is equal to the change in mass in the control volume in unit time: $-\frac{\partial \rho}{\partial t}\delta x \delta y \delta z$, to leading order. Hence, $\frac{\partial(\rho u)}{\partial x} + \frac{\partial(\rho v)}{\partial y} + \frac{\partial(\rho w)}{\partial z} = -\frac{\partial \rho}{\partial t}$, or in vector notation

$$\nabla.(\rho \underline{u}) = -\frac{\partial \rho}{\partial t},$$

where $\underline{u} = (u, v, w)$.

This is the three-dimensional continuity equation for compressible unsteady fluids. The present study concerns incompressible fluids only. Therefore the mass density, ρ, is constant and so

$$\nabla.\underline{u} = 0.$$

Furthermore, in the two-dimensional case, which is discussed first, we can

omit the spatial variable in the z-direction, and so the continuity equation is

$$\frac{\partial u}{\partial x} + \frac{\partial v}{\partial y} = 0. \tag{1.2}$$

1.2.4 Navier-Stokes equations

Applying Newton's second law of motion to our control volume of fluid in the x-direction, and neglecting gravitational effects, implies that the pressure in the x-direction $-p$ is equal to the product of the mass of the fluid and its acceleration in the x direction divided by the area over which this is acting. Therefore $a(x) = \frac{-1}{\rho}\frac{\partial p}{\partial x}$. Similarly, $a(y) = \frac{-1}{\rho}\frac{\partial p}{\partial y}$ and $a(z) = \frac{-1}{\rho}\frac{\partial p}{\partial z}$. However, the substantive acceleration $\underline{a}$ equals $\frac{D\underline{u}}{Dt}$ which is equal to $\frac{\partial \underline{u}}{\partial t} + (\underline{u}.\nabla)\underline{u}$. So, upon neglect of the viscous forces, the above suggests that

$$\frac{\partial u}{\partial t} + u\frac{\partial u}{\partial x} + v\frac{\partial u}{\partial y} + w\frac{\partial u}{\partial z} = \frac{-1}{\rho}\frac{\partial p}{\partial x}, \tag{1.3}$$

$$\frac{\partial v}{\partial t} + u\frac{\partial v}{\partial x} + v\frac{\partial v}{\partial y} + w\frac{\partial v}{\partial z} = \frac{-1}{\rho}\frac{\partial p}{\partial y}, \tag{1.4}$$

$$\frac{\partial w}{\partial t} + u\frac{\partial w}{\partial x} + v\frac{\partial w}{\partial y} + w\frac{\partial w}{\partial z} = \frac{-1}{\rho}\frac{\partial p}{\partial z}. \tag{1.5}$$

In viscous fluids, however, there are tangential and normal forces associated with each surface element. Consideration of these (see [10]) leads to the Navier-Stokes momentum equations:

$$\frac{\partial u}{\partial t}+u\frac{\partial u}{\partial x}+v\frac{\partial u}{\partial y}+w\frac{\partial u}{\partial z}=\frac{-1}{\rho}\frac{\partial p}{\partial x}+\frac{\mu}{\rho}\{\frac{\partial^2 u}{\partial x^2}+\frac{\partial^2 u}{\partial y^2}+\frac{\partial^2 u}{\partial z^2}\}, \qquad (1.6)$$

$$\frac{\partial v}{\partial t}+u\frac{\partial v}{\partial x}+v\frac{\partial v}{\partial y}+w\frac{\partial v}{\partial z}=\frac{-1}{\rho}\frac{\partial p}{\partial y}+\frac{\mu}{\rho}\{\frac{\partial^2 v}{\partial x^2}+\frac{\partial^2 v}{\partial y^2}+\frac{\partial^2 v}{\partial z^2}\}, \qquad (1.7)$$

$$\frac{\partial w}{\partial t}+u\frac{\partial w}{\partial x}+v\frac{\partial w}{\partial y}+w\frac{\partial w}{\partial z}=\frac{-1}{\rho}\frac{\partial p}{\partial z}+\frac{\mu}{\rho}\{\frac{\partial^2 w}{\partial x^2}+\frac{\partial^2 w}{\partial y^2}+\frac{\partial^2 w}{\partial z^2}\}. \qquad (1.8)$$

Once again, for the present initially two-dimensional study, only two spatial variables are required. Therefore, neglecting the z-direction, the governing Navier-Stokes equations are then

$$\frac{\partial u}{\partial t}+u\frac{\partial u}{\partial x}+v\frac{\partial u}{\partial y}=\frac{-1}{\rho}\frac{\partial p}{\partial x}+\frac{\mu}{\rho}\{\frac{\partial^2 u}{\partial x^2}+\frac{\partial^2 u}{\partial y^2}\}, \qquad (1.9)$$

and

$$\frac{\partial v}{\partial t}+u\frac{\partial v}{\partial x}+v\frac{\partial v}{\partial y}=\frac{-1}{\rho}\frac{\partial p}{\partial y}+\frac{\mu}{\rho}\{\frac{\partial^2 v}{\partial x^2}+\frac{\partial^2 v}{\partial y^2}\}. \qquad (1.10)$$

Nevertheless (1.6), (1.7) and (1.8) will be required in later chapters, when the three-dimensional jet is considered.

1.2.5 The boundary layer and the jet

The Navier-Stokes equations are, in general, extremely difficult to solve with accuracy, and any solutions that do exist tend to be limited in their application. However, it is often possible to derive and use approximate forms of the equations which are much simpler and therefore easier to solve. For instance, Prandtl [16] proposed that at high Reynolds numbers (e.g. small viscosity) the majority of the flow past a bluff body, for example, is in effect inviscid; any viscous effects are confined to a relatively thin layer, of thickness δ say, immediately adjacent to the body. This can be justified as follows.

For a relatively slender body of length L immersed in a fluid with velocity U, the time taken by a fluid particle to pass the body will be L/U. However the time needed for viscous effects to spread across streamlines will be of order $O(\nu L/U^3)^{\frac{1}{2}}$, where ν is the kinematic viscosity μ/ρ, since $(L/\delta)^2 \sim O(Re)$ (see [14, pp 304]). Therefore there will be a thin viscous region close to the body if $(\nu L/U^3)^{\frac{1}{2}} << L/U$ or $UL/\nu >> 1$. This thin region is the *boundary layer.* In the boundary layer the velocity of the fluid at the boundary is taken to be 'zero' or, more precisely, the velocity of the boundary, and the fluid velocity increases rapidly from that boundary value to approach the freestream velocity asymptotically within a very small distance, δ say, from the surface. This, therefore, is a region in which effects associated with the viscous shear stress $\mu\frac{du}{dy}$ cannot be ignored, even when μ is small.

It should be noted though that solid boundaries are not essential for the formation of boundary layers or boundary-layer-like layers (see, for instance

[17], [50]). The interaction of two parallel streams of fluid with appreciably different velocities, for example, produces a free boundary layer or free shear layer. This is similar to the situation that exists when a narrow jet of fluid issues into relatively still but like fluid. The velocity of the fluid changes rapidly away from the jet's axis, and this leads to a *free jet layer.* Furthermore, Birkhoff and Zarantonello [18, pp298] contend that, in most engineering (real) situations, the flow within the jet will probably be turbulent if $Re > 10^3$. The present study is concerned with slender jets of air issuing from narrow ducts into relatively still ambient air. Therefore the arguments above underpin the work in this thesis; however, we will assume for definiteness throughout that the jets are laminar, at least within the axial distances of interest here.

1.2.6 Sortex jets

In reports [19] and [20] to Sortex, Smith has shown that the jets of interest here have an initial velocity of between 20 and $40ms^{-1}$. Henceforth we will assume a representative initial velocity of $20ms^{-1}$; justification for this is suggested by the very good data fit for the pressure solution at the end of chapter 4. Published figures indicate that for air under standard conditions ν is $1.46 \times 10^{-5}m^2s^{-1}$. The jets emerge from rectangular nozzles, which we will consider for the moment to have a characteristic width of $2mm$. This implies a boundary layer thickness, δ, equal to $1mm$, this being the semi-width of the issuing jet. It follows, since $(L/\delta)^2 \sim O(Re)$ and $Re = UL/\nu$, where L is the characteristic streamwise length of the system and U is the

initial velocity, that L is approximately $1.37m$ and Re_L is in the region of 1.8×10^6. It should be noted, in contrast, that within the industrial setting of food-sorting machines we are only concerned with the development and interactions of jets over a distance of $150mm$ or less than $0.11L$, which is a comparatively small distance.

1.2.7 Boundary layer equations

If L is a characteristic length in the direction of flow, U is a characteristic velocity and δ is a typical length normal to the direction of flow then, in terms of orders of magnitude, $\frac{\partial u}{\partial x} \sim O(\frac{U}{L})$ and $v \sim O(\frac{U\delta}{L})$, from continuity. The continuity equation also implies that the normal velocity component is small compared with U if $\frac{\delta}{L}$ is small. Furthermore, if we take a typical value for p as (ρU^2), then the terms of equation (1.9) are in the following proportions: $1 : 1 : 1 : 1 : \frac{1}{Re} : \frac{1}{Re}(\frac{L}{\delta})^2$. These indicate that, for large Reynolds numbers, the viscous terms are both small if δ and L are of the same magnitude. However, across the boundary layer (or jet or other thin layer) the y derivatives are generally much larger than derivatives with respect to x. Therefore the $\frac{\partial^2 u}{\partial x^2}$ term is very much smaller than the $\frac{\partial^2 u}{\partial y^2}$ term and can be ignored. Hence, within the boundary layer, the full equation (1.9) should be replaced by

$$\frac{\partial u}{\partial t} + u\frac{\partial u}{\partial x} + v\frac{\partial u}{\partial y} = -\frac{\partial p}{\partial x} + \nu\frac{\partial^2 u}{\partial y^2} \tag{1.11}$$

where ν is the *kinematic viscosity* $\frac{\mu}{\rho}$. Similar analysis of equation (1.10) shows that all terms are relatively small compared with the pressure derivative with respect to y, indicating that the normal pressure gradient has to be very small

and hence the total pressure change across the boundary layer is so small that the change can be ignored. The continuity equation remains unchanged within the boundary layer.

The problem specification, its industrial relevance and the underpinning mathematics needed to investigate it have now been described and we are in a position to begin to build the mathematical model.

Chapter 2

Two-dimensional Jets

2.1 Similarity solution (steady symmetric jet)

We consider here a slender symmetric two-dimensional steady incompressible jet of air, which discharges from a narrow slit into still ambient air, and we demonstrate the analytical solution of Schlichting [25]. This will be of use later on.

There are no bounding walls, so the pressure gradient in the stationary outside fluid is expected to be zero. This then imposes a zero pressure gradient throughout the flow within the jet. Hence (1.9) becomes

$$u\frac{\partial u}{\partial x} + v\frac{\partial u}{\partial y} = \nu\frac{\partial^2 u}{\partial y^2} \tag{2.1}$$

and (1.2), (2.1) form the governing equations for the jet. Note that x denotes the direction of total force acting on the fluid at the point of origin. Clearly the boundary conditions are that $u \to 0$ as $|y| \to \infty$ and $\frac{\partial u}{\partial y} = 0$ at $y = 0$.

To solve, we integrate (2.1) with respect to y:

$$\int_{-\infty}^{\infty} u\frac{\partial u}{\partial x}dy + \int_{-\infty}^{\infty} v\frac{\partial u}{\partial y}dy = \nu \int_{-\infty}^{\infty} \frac{\partial^2 u}{\partial y^2}dy, \tag{2.2}$$

which implies

$$2\int_{-\infty}^{\infty} u\frac{\partial u}{\partial x}dy = \left[\nu\frac{\partial u}{\partial y}\right]_{-\infty}^{\infty} = 0. \tag{2.3}$$

Hence

$$\frac{\partial}{\partial x}\int_{-\infty}^{\infty} u^2 dy = 0, \tag{2.4}$$

so that

$$\int_{-\infty}^{\infty} u^2 dy = constant\ \forall x. \tag{2.5}$$

Hence the momentum flux over any cross-section of the jet is constant.

Let $\psi = \psi(x,y)$ be the *stream function*, such that $u = \frac{\partial\psi}{\partial y}$ and $v = -\frac{\partial\psi}{\partial x}$ with $\psi = 0$ at $y = 0$. Then the continuity equation (1.2) is satisfied by ψ and, considering the momentum equation (2.1), we seek a solution in which successive velocity profiles are supposed to have the same shape, so that ψ is of the form $\psi(x,y) \propto x^p f(\eta)$, say, where $\eta = \frac{y}{x^q}$, with p and q constants to be determined. Then (2.1) can be rewritten in terms of the new variables, and the momentum equation is replaced by the following equation:

$$x^{p-1}\{(p-q)f'^2 - pff''\} = \nu x^{-q} f'''. \tag{2.6}$$

To satisfy consistency with (2.6), $p+q = 1$. Also, rewriting (2.5) in terms of

the new variable we find

$$\frac{\partial}{\partial x}\int_{-\infty}^{\infty} x^{2p-q} f'^2 d\eta = 0.$$

Hence $2p - q = 0$ and it follows immediately that $p = \frac{1}{3}$ and $q = \frac{2}{3}$. Hence the solution is

$$\psi(x,y) = x^{\frac{1}{3}} f(\eta), \quad \eta = y x^{\frac{-2}{3}} \tag{2.7}$$

and (2.1) is replaced by the ordinary differential equation

$$f''' + \frac{1}{3\nu}\{ff'' + f'^2\} = 0 \tag{2.8}$$

with boundary conditions: $f'(\eta) \to 0$ as $\eta \to \pm\infty$ and $f'(\eta) = f'(-\eta)$.

Integrating (2.8) twice with respect to η and rearranging then gives

$$\int \frac{df}{6c\nu - f^2} = \frac{1}{6\nu}\int d\eta \tag{2.9}$$

which, after making the substitution $f = \sqrt{6c\nu}\tanh\theta$, gives the result

$$f = \sqrt{6c\nu}\tanh\left(\sqrt{\frac{c}{6\nu}}\eta\right) \tag{2.10}$$

with f set to zero at $\eta = 0$.

The jet velocity profile, then, is given by Bickley's solution [24]

$$f' = \frac{c}{\cosh^2(\sqrt{\frac{c}{6\nu}}\eta)}, \quad \eta = \frac{y}{x^{\frac{2}{3}}}. \tag{2.11}$$

This agrees with the classical $sech^2 y$ profile described by Schlichting [25].

By making the substitution $u = x^{\frac{-1}{3}} f'$, which is implied above, it is possible to evaluate the momentum flux $M = \rho \int_{-\infty}^{\infty} u^2 dy$ and obtain a value for c. Thus

$$M = \rho \int_{-\infty}^{\infty} \left[\frac{c}{x^{\frac{1}{3}}} sech^2 (\sqrt{\frac{c}{6\nu}} \frac{y}{x^{\frac{2}{3}}}) \right]^2 dy,$$

which, after integrating, gives

$$M = \frac{4}{3} \rho c^2 \sqrt{\frac{6\nu}{c}},$$

and hence

$$c \simeq 0.4543 (\frac{M^2}{\rho\mu})^{\frac{1}{3}}.$$

Therefore the centreline velocity is $u_c \simeq 0.4543 (\frac{M^2}{\rho\mu x})^{\frac{1}{3}}$, suggesting that for a given momentum flux and fluid the centreline velocity decreases as $x^{\frac{-1}{3}}$.

Further, the mass rate of flow across any perpendicular plane is $\dot{m} = \rho \int_{-\infty}^{\infty} u dy$, giving

$$\dot{m} = \rho \int_{-\infty}^{\infty} \frac{c}{x^{\frac{1}{3}}} sech^2 (\sqrt{\frac{c}{6\nu}} \frac{y}{x^{\frac{2}{3}}}) dy$$

$$\simeq 3.302 (\mu\rho M x)^{\frac{1}{3}}. \qquad (2.12)$$

Thus $\dot{m}$ increases like $x^{\frac{1}{3}}$, as ambient fluid is entrained by the jet.

The appropriate Reynolds number here may be taken to be $\frac{\dot{m}}{\mu} \sim (\frac{M\rho x}{\mu^2})^{\frac{1}{3}}$. Therefore in a sense the accuracy of the solution improves as x increases,

but on the other hand small values of x indicate a small Reynolds number and, hence, close to the origin of the jet there might exist a region where the boundary layer equations are not valid. Furthermore, the solution is restricted in its application simply because it assumes and imposes a self-similar form, which would not usually be appropriate for jets with a predefined initial velocity profile. Since the accuracy of the solution improves with increased Reynolds number and hence with greater distance downstream, it is generally regarded as a far-downstream asymptote, and we will use it as such in the sections that follow.

2.2 Numerical solution (steady jet)

2.2.1 Introduction

Since the validity of the similarity solution described above is limited sufficiently close to the jet's origin, an alternative method of solution is required if we are to understand the development and interactions between jets over the relatively short distance of interest to Sortex (see 1.2.6 above). Several numerical schemes exist which could be employed and which could give the level of accuracy needed. However, probably one of the simplest and easiest to program is the following scheme employing finite differences to represent the terms of the given differential equations.

In the case of the two-dimensional steady jet, dimensional analysis of the Navier-Stokes equations showed the second order derivatives with respect to x to be small enough to be ignored. Hence the governing boundary-layer

equations are parabolic in x, provided u remains positive, and so the numerical scheme used to solve them is of the downstream-marching type. By this it is meant that previously known values are used to compute the unknown solution values required at the next station in the streamwise direction. These, in turn, are used to calculate the values at the next station, and so on.

Finite difference schemes can be sub-classified as either implicit or explicit. Explicit schemes are the simplest to implement and they calculate the required downstream profiles immediately from known upstream data. However, they require very small streamwise steps in order to maintain accuracy as well as numerical stability and therefore a greater number of steps to reach the desired x-station downstream. Implicit schemes employ matrix inversion to solve at points on the downstream profile simultaneously and iterate to account for the non-linearity of the system. These schemes are numerically stable and therefore, unlike the explicit schemes, do not require the steps to be very small. The scheme adopted here is loosely termed 'semi-implicit' (see, for instance, [21]) since some of the terms at the next station are used to approximate the derivatives.

2.2.2 Semi-implicit finite difference model for the two-dimensional steady jet

Once again, we take as our starting point equations (1.2) and (2.1),

subject to

$$u \to 0 \ as \ |y| \to \infty \tag{2.13}$$

$$\frac{\partial u}{\partial y} = 0 \ at \ y = 0, \tag{2.14}$$

$$v = 0 \ at \ y = 0. \tag{2.15}$$

We consider a smooth symmetrical initial profile $u = u_0 = sech(y)$ at $x = 0$.

The numerical/computer solution is obtained by employing a semi-implicit finite-differencing approach, which marches forward in x (in small steps Δx) from the chosen starting profile u_0 at $x = 0$, with all v velocity components initially set to zero. In this scheme the undifferentiated terms in (2.1) are taken to be the known values from the previous station. A *forward* difference in x is used to model $\frac{\partial u}{\partial x}$ at the current station and *central* differences in y are used to model $\frac{\partial u}{\partial y}$ and $\frac{\partial^2 u}{\partial y^2}$ at the next station. This gives a solution for u at the next x-station. The continuity equation (1.2) is then employed to find the corresponding v components. The computer variables are then updated with these new values and the program marches forward to solve at the next x-station.

Replacing the terms of (2.1) with the corresponding difference terms yields the following finite difference equation:

$$u_{m,n}\left[\frac{u_{m+1,n} - u_{m,n}}{\Delta x}\right] + v_{m,n}\left[\frac{u_{m+1,n+1} - u_{m+1,n-1}}{2\Delta y}\right]$$

$$= \nu\left[\frac{u_{m+1,n+1} - 2u_{m+1,n} + u_{m+1,n-1}}{(\Delta y)^2}\right], \tag{2.16}$$

which we need to solve for $u_{m+1,n}$.

Let $\alpha_n = \frac{\nu \Delta x}{u_{m,n}(\Delta y)^2}$ and $\beta_n = \frac{v_{m,n}\Delta x}{2u_{m,n}\Delta y}$. Then (2.16) reads

$$(\beta_n - \alpha_n)u_{m+1,n+1} + (1 + 2\alpha_n)u_{m+1,n} - (\alpha_n + \beta_n)u_{m+1,n-1} = u_{m,n} \quad (2.17)$$

where $u_{m,n}$ is known from the previous x-station.

Considering a finite difference grid that is N nodes wide, with $y = y_{-\infty}$ (modelling $-\infty$) at $n = 0$ and $y = y_{\infty}$ (modelling $+\infty$) at $n = N - 1$, then (2.17) produces $N - 2$ equations, each containing three unknowns. The coefficients of these equations form a tridiagonal matrix, in which $a_j = -(\alpha_j + \beta_j)$; $b_j = 1 + 2\alpha_j$ and $c_j = \beta_j - \alpha_j$, which may be solved simply, since b_0 and b_{N-1} are zero, using a variation on Gaussian elimination known as the Tri-Diagonal Matrix Algorithm. The matrix equation is depicted below, a_j, b_j and c_j are those described above and $\overline{u}_j$ is the specified initial condition.

$$\begin{bmatrix} 1 & 0 & 0 & 0 & \dots & 0 \\ a_1 & b_1 & c_1 & 0 & \dots & 0 \\ 0 & a_2 & b_2 & c_2 & \dots & 0 \\ 0 & \ddots & \ddots & \ddots & \ddots & \vdots \\ 0 & \ddots & \ddots & a_{N-1} & b_{N-1} & c_{N-1} \\ 0 & 0 & 0 & 0 & 0 & 1 \end{bmatrix} \begin{bmatrix} u_{m+1,0} \\ u_{m+1,1} \\ \vdots \\ \vdots \\ u_{m+1,N-2} \\ u_{m+1,N-1} \end{bmatrix} = \begin{bmatrix} u_{m,0} \\ u_{m,1} \\ \vdots \\ \vdots \\ u_{m,N-2} \\ u_{m,N-1} \end{bmatrix} . \quad (2.18)$$

The u values obtained from (2.18), along with known values from previous x-stations, are then substituted into the following finite difference representation of the continuity equation (1.2) to obtain values for v.

Taking Wu's difference equation [8]:

$$\left[\frac{u_{m+1,n} - u_{m,n}}{2\Delta x} + \frac{u_{m+1,n-1} - u_{m,n-1}}{2\Delta x}\right] + \left[\frac{v_{m+1,n} - v_{m+1,n-1}}{\Delta y}\right] = 0 \quad (2.19)$$

and rearranging for $v_{m+1,n}$, we obtain

$$v_{m+1,n} = \frac{\Delta y}{2\Delta x}\left[u_{m,n} + u_{m,n-1} - u_{m+1,n} - u_{m+1,n-1}\right] + v_{m+1,n-1}, \quad (2.20)$$

in which m again represents the previous x-station.

The v values can then be obtained in two parts, employing either (2.20) or the following equation (2.21), splitting the finite difference grid into two halves along the freestream axis and working from this axis out to the outer boundaries.

$$v_{m+1,n} = \frac{\Delta y}{2\Delta x}\left[u_{m,n} + u_{m,n-1} - u_{m+1,n} - u_{m+1,n-1}\right] + v_{m+1,n+1}. \quad (2.21)$$

2.2.3 Testing the scheme

Before moving on to use the numerical solution as a means to gain a greater understanding of the behaviour and development of more realistic jets, it is obviously important to make sure that the scheme employed is valid and that it has been programmed correctly. Therefore the following tests were carried out.

Comparison with similarity solution

The velocity profile of any steady two dimensional jet dispersing into a surrounding of like fluid is expected to eventually tend towards the similarity solution of (Section 2.1). Therefore the numerical solution was programmed and then run with an arbitrary initial profile, which was symmetric about the (streamwise) x-axis. A coarse grid containing 75 y-stations, with $\Delta y = 0.1$ and $\Delta x = 0.01$ produced results close to those of the similarity solution. Refining the grid, so that it contained 2001 y-stations with $\Delta y = 0.01$ and marching forward over 1000 x steps at $\Delta x = 0.0005$ further improved the approximation. Figure 2.1 illustrates the velocity profiles produced for a smooth initial profile at $x = 0.1, 1.0$, and 10.0. The approximation seems to tend towards the $sech^2 y$ velocity profile of (2.11).

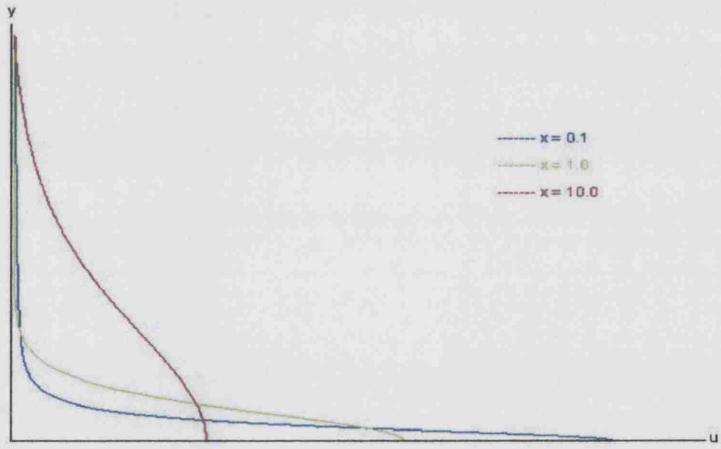

Figure 2.1: half profile for $u_0 = sech(y)$ at stations $x = 0.1, 1.0, 10.0$.

The initial profile was replaced with a Bickley-like ($sech^2 y$) profile, in which

initial us and vs were obtained from the solution in (Section 2.1), and the program was run again. The Bickley profile was maintained, and the computed value for $u|_{y=centreline}$ was compared directly with that obtained from the analytical solution. For a grid containing 2001 y-stations at $\Delta y = 0.01$, with $\Delta x = 0.0005$, the numerical approximation remained correct to within $< 1\%$ error over 14,000 steps; and correct to within 4% error over 20,000 steps (where the error was taken to be the difference between the solutions expressed as a percentage of the analytical solution). It was further found that the numerical approximation remained accurate to within less than 0.035% over 20,000 steps if the number of y-stations was increased to 4001.

Grid effects

In the finite difference scheme used, the accuracy in terms of Δy was of second order. Therefore, for a fixed solution domain with constant Δx, and at a prescribed x-station, plotting $u|_{y=0}$ for increasing values of Δy should produce a parabolic curve. This is confirmed in figure 2.2.

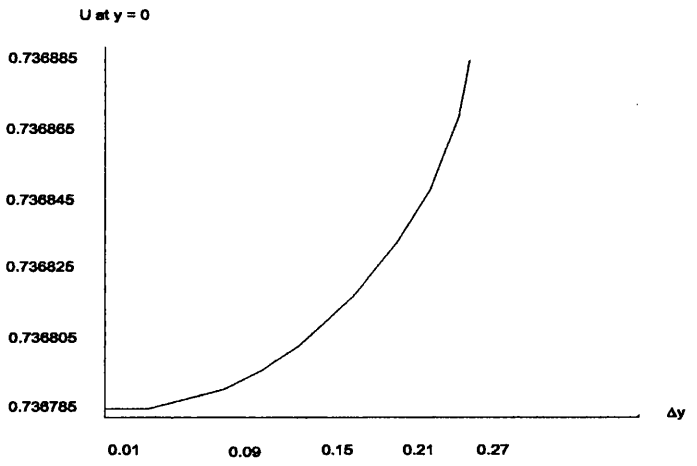

Figure 2.2: Streamwise velocity at a fixed x-station for varying Δy.

Similarly, within the scheme, the accuracy in terms of Δx was of first order. Therefore, fixing Δy whilst varying Δx should produce a straight-line plot of the streamwise velocity. This is confirmed in figure 2.3.

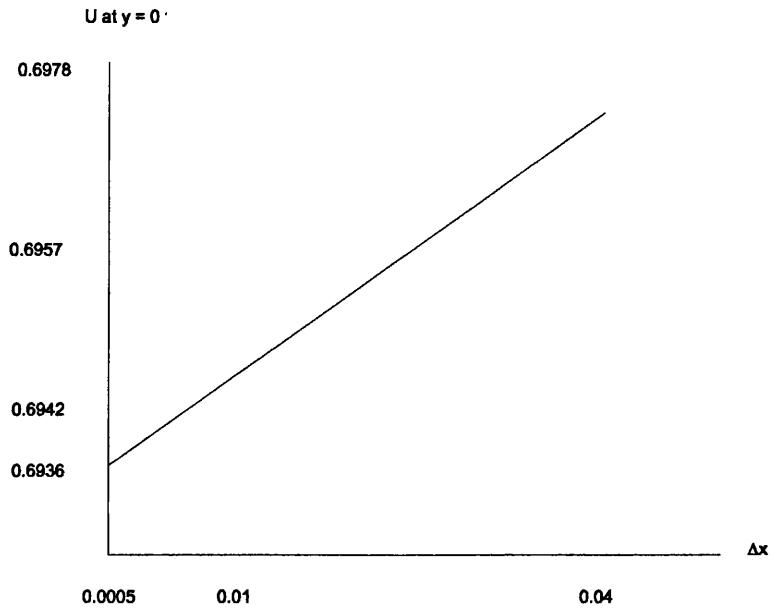

Figure 2.3: Streamwise velocity at a fixed x-station for varying Δx.

Action of several jets

By changing the initial profile it was possible to simulate multiple jets issuing simultaneously from neighbouring ducts. This is of interest in the industrial application as outlined in the introduction, and provides a preliminary check prior to the more complex three-dimensional study to follow. Figure 2.4 illustrates how separate but identical jets coalesce and assume the Bickley jet form far downstream.

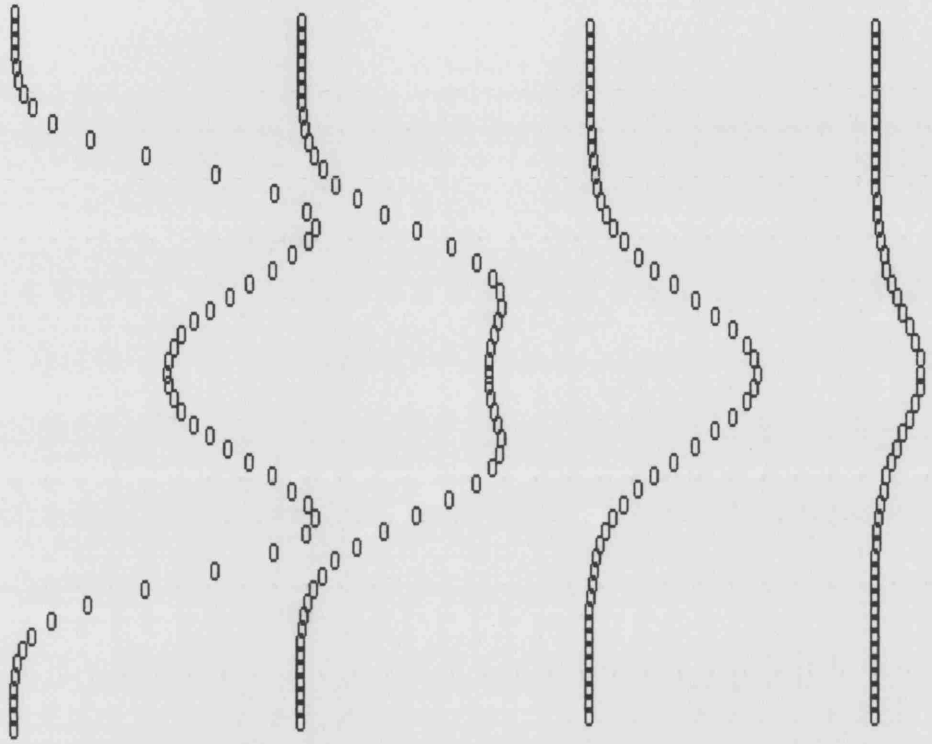

Figure 2.4: Simulation of two jets merging downstream

2.2.4 Non-symmetric steady two-dimensional jet

All realistic jet velocity profiles have a point of inflection (which means in practical terms that they are unstable and are likely to become turbulent at quite low Reynolds number). In many realistic configurations it is likely that the jet will also be non-symmetric about the freestream axis, $y = 0$. This subsection considers such a non-symmetric jet and outlines the modifications necessary in order to obtain a valid finite-difference solution scheme, which can be implemented on a computer.

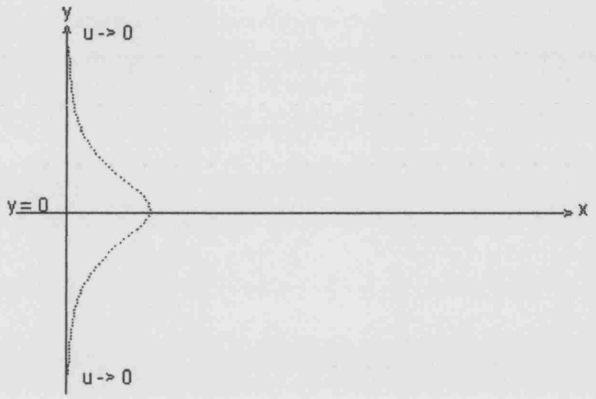

Figure 2.5: Symmetric (ideal)case.

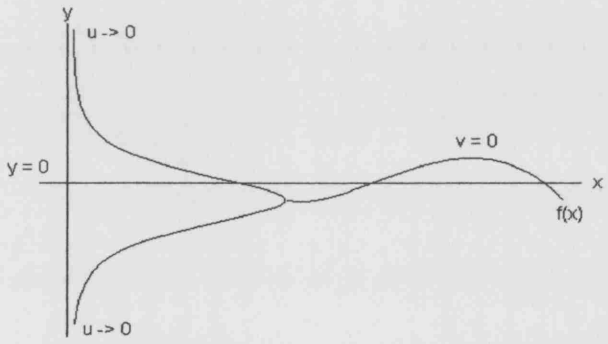

Figure 2.6: Non-symmetric case.

Prandtl transposition

In order to solve such a non-symmetric problem, the Prandtl transposition can be applied to the original (x, y) co-ordinates to give a new set of co-ordinates, (ζ, η) say, which follow the curve $f(x)$. Considering the continuity

and momentum equations, we may transpose variables from x, y to ζ, η, where $\zeta = x$ and $\eta = y - f(x)$.

Hence,

$$u_x = \frac{\partial u}{\partial \zeta} - f'(x)\frac{\partial u}{\partial \eta}, \quad u_y = \frac{\partial u}{\partial \eta}, \quad \frac{\partial v}{\partial y} = \frac{\partial v}{\partial \eta}, \text{ and } \frac{\partial^2 u}{\partial y^2} = \frac{\partial^2 u}{\partial \eta^2},$$

and the continuity equation becomes

$$\frac{\partial u}{\partial \zeta} - \frac{\partial u}{\partial \eta} f'(x) + \frac{\partial v}{\partial \eta} = 0. \tag{2.22}$$

This may be rewritten as

$$\frac{\partial u}{\partial \zeta} + (v - uf'(x))\frac{\partial}{\partial \eta} = 0. \tag{2.23}$$

Then, letting $\overline{v} = v - uf'(x)$ yields

$$\frac{\partial u}{\partial \zeta} + \frac{\partial \overline{v}}{\partial \eta} = 0. \tag{2.24}$$

The momentum equation is replaced by

$$u\{\frac{\partial u}{\partial \zeta} - \frac{\partial u}{\partial \eta} f'(x)\} + v\frac{\partial u}{\partial \eta} = \nu \frac{\partial^2 u}{\partial \eta^2},$$

which after rearranging and substituting for $\overline{v}$, from above, reads

$$u\frac{\partial u}{\partial \zeta} + \overline{v}\frac{\partial u}{\partial \eta} = \nu\frac{\partial^2 u}{\partial \eta^2}. \tag{2.25}$$

The boundary conditions become: $u \to 0$ as $|\eta| \to \infty$ and
$\overline{v} + uf'(x) = 0$ at $\eta = 0$.

Thus, after the transposition, we are left with essentially the same problem but in terms of the new variables and with new boundary conditions relative to these. This can be programmed in an exactly similar way to the symmetric problem of (2.2.2).

2.3 Small-distance analysis

In section 1.2.5 it was shown that the jet model system's characteristic streamwise length is approximately $1.37m$ in practical terms. Therefore, although the numerical approximation seems to produce very good results, the length scale is by far in excess of that required for a full description of the jet properties over an active range of $150mm$ (this being the typical active range of jets employed in sorting machines, such as those manufactured by Sortex Ltd). Hence small-distance analysis should be considered, since it may provide an economical and accurate analytical solution to complement the numerical work.

2.3.1 Analysis of a simple spread-out initial profile

Since the distance over which the Sortex jets operate is less than 0.11 × the characteristic length, small-x analysis may be appropriate. In that case the flow solutions expand as

$$(u, \psi) = (u_0, \psi_0) + x\,(u_1, \psi_1) + \ldots \textit{ for small positive } x. \tag{2.26}$$

Then $u_0 = \psi_0'$, $u_1 = \psi_1'$, etc, and the non-dimensionalised momentum equation (2.1) becomes

$u_0 u_1 - \psi_1 u_0' = u_0''$ at leading order. Therefore $u_0\psi_1' - \psi_1 u_0' = u_0''$, implying that

$$\psi_1 = u_0 \int_0^y \frac{u_0''}{u_0^2} dy, \tag{2.27}$$

where we assume throughout that $u_0 > 0$.

Then u_1 follows as

$$u_1 = \psi_1' = u_0 \frac{u_0''}{u_0^2} + u_0' \int_0^y \frac{u_0''}{u_0^2} dy. \tag{2.28}$$

Therefore, if we consider the initial profile $u_0 = sech(y)$, say, as an example which is smooth and symmetric about the freestream axis, so that $u_0' = -sech(y)\tanh(y)$ and $u_0'' = sech(y)\,[1 - 2sech^2(y)]$, we obtain

$$u_1 = [1 - 2sech^2(y)] - sech(y)\tanh(y) \int_0^y [\cosh(y) - 2sech(y)]\, dy \tag{2.29}$$

which, after performing the integration, gives

$$u_1 = \left[1 - 2sech^2(y)\right] - sech(y)\tanh(y)\left[\sinh(y) - 4\tan^{-1}(e^y) + \pi\right]. \quad (2.30)$$

Figures 2.7 and 2.8 compare the numerical approximation of centreline velocity with that obtained by the small-distance analysis, at a particular x station. It can be seen clearly that the solutions remain very close. This trend continues even as $x \to 0.1$ (the distance of industrial interest to Sortex).

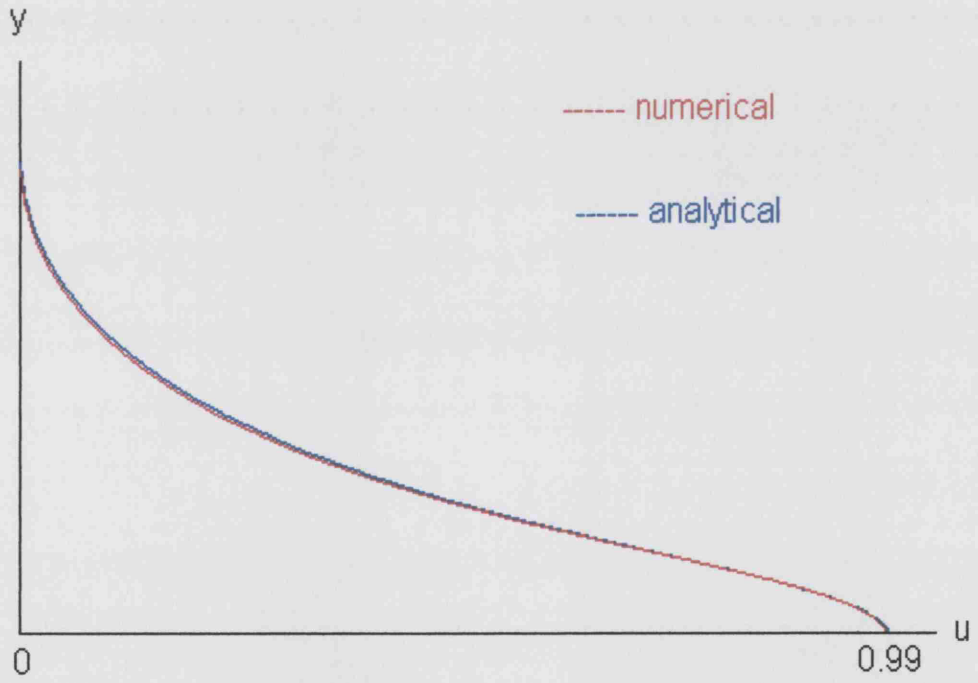

Figure 2.7: centreline velocity at x = 0.005

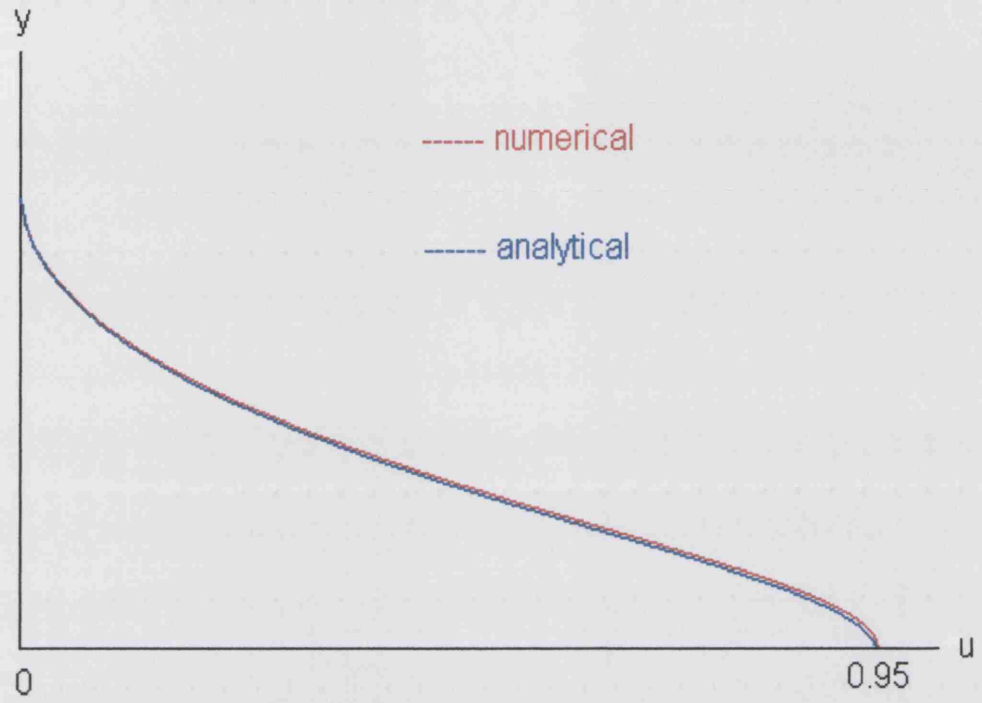

Figure 2.8: centreline velocity at x = 0.05

The next graph shows the difference between the values obtained for centreline velocity at $x = 0.1$. Initial inspection may seem to suggest that the two solutions are markedly different but closer inspection reveals that the difference between the two solutions is still only approximately 2% of the analytical solution at that x station.

Based on these comparisons, then, it seems promising that small-distance analysis may well provide an entirely accurate analytical tool. There are limitations though, and these are highlighted next.

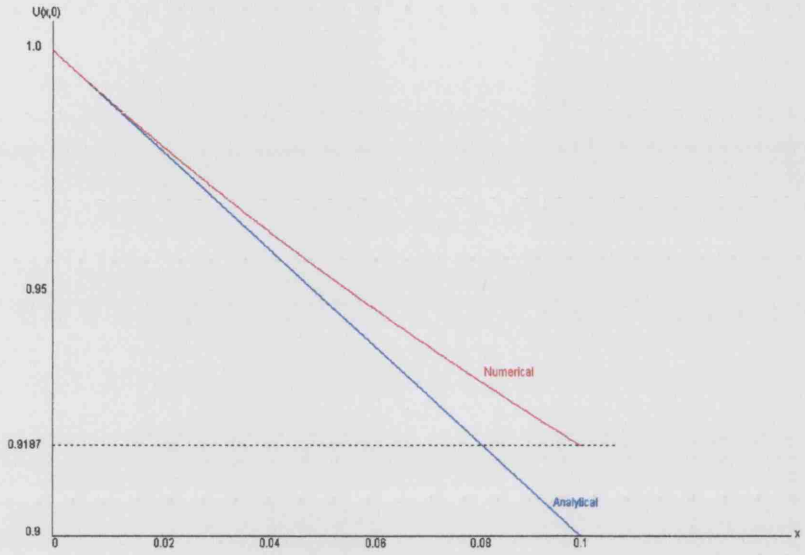

Figure 2.9: centreline velocity at x = 0.1

2.3.2 Analysis of a smoothed 'unit-pulse' profile

Having shown that a leading order small-distance analysis works well for a simple spread-out initial profile such as $u_0(y) = sech(y)$, we now consider the initial profile $u_0 = (1 + y^N)^{-1}$ (with N typically large), which is a smoothed unit-pulse, and which might be more typical of initial profiles produced from fully developed flows from ducts of the type considered here (albeit in two dimensions). This profile hints at being discontinuous (and becomes so in the limit as N tends to infinity), since the profile remains close to unity for $0 \leq y < 1$, but decays rapidly towards zero as y increases through the value 1.

Once again the flow solutions expand as in (2.26), so that $u_1(y)$ is given by (2.28) and it follows that, in this case with N taken as 10, the perturbation effect is given by

$$u_1(y) = \frac{10y^8}{(1+y^{10})^2}\left[(11y^{10}-9) - y\int_0^y \frac{10y^8(11y^{10}-9)}{1+y^{10}}dy\right]. \qquad (2.31)$$

At very small x there is generally very good agreement, as shown in figure 2.10; see also the comments concerning large y later in this subsection. In figure 2.11 the solution obtained by leading order small-distance analysis can be seen to depart from the numerical solution after just 10 steps (less than 7mm in Sortex terms). The poor agreement becomes more pronounced as we march forward in x, as seen in figure 2.12. However, we would expect the velocity profile to get ever closer to the similarity form of (2.11), and, hence, we must conclude that the small-x solution is inappropriate in this case.

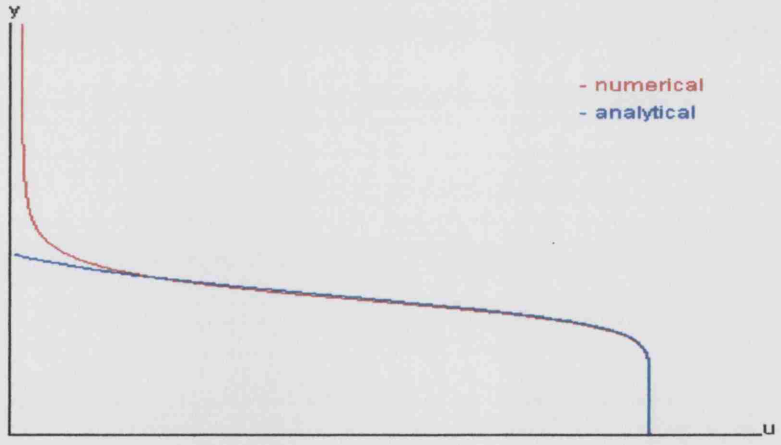

Figure 2.10: comparison of numerical and small-x solution at $x = 0.0005$ for $N = 10$.

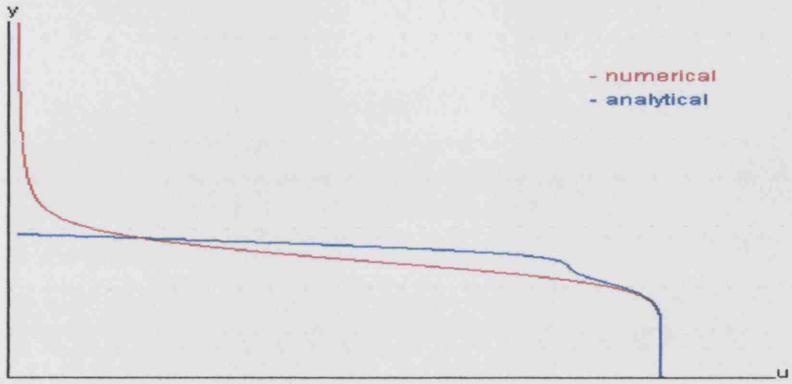

Figure 2.11: comparison of numerical and small-x solution at $x = 0.005$ for $N = 10$.

The poor agreement exhibited in figure 2.12 becomes even more pronounced as the initial profile under consideration becomes less smooth, being especially pronounced in the limit of a discontinuous initial profile. This is because a region of non-linearity then exists, in which there is a free-shear layer of Blasius type, which cannot be resolved by the above leading order analysis. The resolution, as well as the behaviour at large y values in all of figures 2.10 - 2.12, can be explained analytically or approximately as follows.

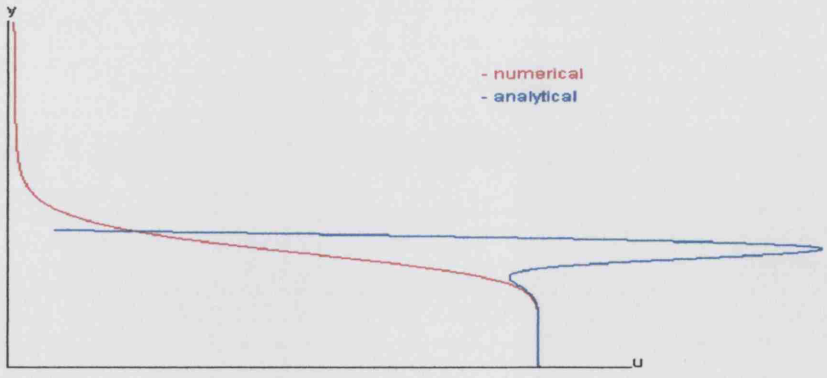

Figure 2.12: comparison of numerical and small-x solution at $x = 0.01$ for $N = 10$.

Firstly, for the above initial profile, at sufficiently large y, $u_0 = \frac{1}{1+y^{10}} \sim O(y^{-10})$, so that

$$\psi_1 \simeq y^{-10} \int_0^y \frac{y^{-12}}{y^{-20}} dy \sim O(y^{-1}).$$

Therefore $u_1 \sim \frac{y^{-12}}{y^{-10}} + y^{-12} \sim O(y^{-2})$ since the term y^{-12} on its own here is negligible. Combining the terms u_0 and xu_1 therefore we have $u \simeq y^{-10} + xy^{-2}$. Hence there is a distinct new outer region where $y \sim x^{\frac{-1}{8}}$ is large (since $x << 1$). The extra outer region is in fact associated with the dominance of the inertial term $v\frac{\partial u}{\partial y}$ at sufficiently large y where u decays towards zero of course but v tends to a (negative) function of x, corresponding to the jet entrainment. Secondly, Lock's solution to the free-shear layer problem, which is documented in [7], must be used near $y = 1$ in order to overcome the local difficulties there; this leads to the next sub-section.

2.3.3 Lock's solution to the free-shear layer problem

Here we demonstrate how the free-shear layer may be resolved by employing Lock's solution in region III (the viscous shear-layer) of figure 2.13, which then has to be matched-up to the solutions obtained in regions I and II outside of the free-shear-layer.

In regions I and II of figure 2.13, the stream function expands as

$$\psi = \psi_0(y) + x^m \psi_1(y) + ..., \; say \tag{2.32}$$

similarly to that in section 2.3.1, but here m is to be found.

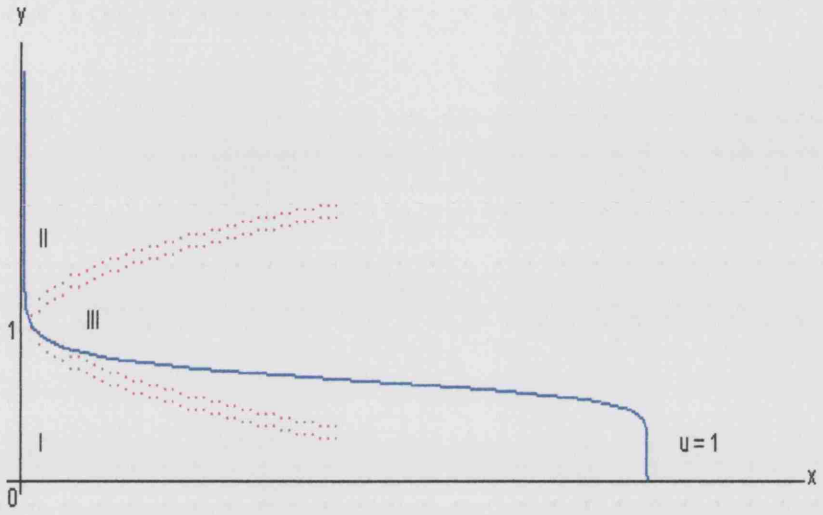

Figure 2.13: revised smoothed unit-pulse problem.

Along with the above, in the Lock region III, the expansion is

$$\psi = C_1 + x^{\frac{1}{2}} f(\eta) + ..., \tag{2.33}$$

where $\eta = (y - H)x^{\frac{-1}{2}}$ and C_1 is the O(1) value of $\psi_0(H)$. The scalings involved are found from an order-of-magnitude argument, and here we take H as 1 without loss of generality.

Therefore in III we have $u = \frac{\partial \psi}{\partial y} = f'(\eta)$; $v = \frac{-1}{2} x^{\frac{-1}{2}} \{f(\eta) - x^{\frac{-1}{2}}(y-H)f'(\eta)\}$; $\frac{\partial u}{\partial x} = \frac{-1}{2}(y - H)x^{\frac{-3}{2}} f''(\eta)$; $\frac{\partial u}{\partial y} = x^{\frac{-1}{2}} f''(\eta)$ and $\frac{\partial^2 u}{\partial y^2} = x^{-1} f'''(\eta)$.

Hence the momentum equation can be rewritten as follows:

$$\frac{-1}{2}(y - H)x^{\frac{-3}{2}} f' f'' - \frac{x^{\frac{-1}{2}}}{2}\{f - x^{\frac{-1}{2}}(y - H)f'\}x^{\frac{-1}{2}} f'' = x^{-1} f'''. \tag{2.34}$$

This reduces to the Blasius equation $f'''+\frac{1}{2}ff''=0$, as expected, but with the boundary conditions (as in Lock) being $f'(-\infty)=u_0(H-)$ and $f'(+\infty)=0$ to match with the solutions in regions I and II.

No analytical solution to equation 2.34 exists. However, an approximate solution with these boundary conditions in [7] gives $f(+\infty)=C_2=1.24$ as the positive entrainment constant and this has also been confirmed numerically.

Also, in II, $\psi_0 = C_1$ remains constant to leading order (corresponding to the existence of only small flow velocities). Therefore matching (2.32) and (2.33) yields $m=\frac{1}{2}$ and $\psi(H+)=f(+\infty)=C_2$.

Furthermore, balancing $C_1+(y-H)u_0(H-)+...+x^{\frac{1}{2}}\psi_1$ against $C_1+x^{\frac{1}{2}}\{\eta u_0(H-)+C_3\}$ beneath implies that $C_3=\psi_1(H-)$, since $\eta=(y-H)x^{\frac{-1}{2}}$.

In region I then, $u=u_0+x^{\frac{1}{2}}u_1+..$ and $\psi=\psi_0+x^{\frac{1}{2}}\psi_1+....$ Therefore the non-dimensionalised momentum equation may be written as

$$\frac{1}{2}u_0x^{\frac{-1}{2}}\psi_1'-\frac{1}{2}x^{\frac{-1}{2}}\psi_1u_0'=u_0''+...$$

So $u_0\psi_1'-\psi_1u_0'=0$ to leading order. Hence $\frac{\psi_1}{u_0}$ must be constant. The solution in region I therefore has the form $\psi_1=A_1u_0$, where A_1 is the constant of integration. Then symmetry about $y=0$ requires $A_1=0$, meaning that the motion induced in region I is comparatively slow.

In conclusion, then, using small-distance analysis to leading order we can

construct the starting behaviour for the flow and obtain reasonably accurate results for smooth continuous initial profiles. However, if the initial profile is subject to abrupt changes (e.g. the initial profile is of the 'top-hat' type, or is very nearly so) then small-distance analysis to leading order is insufficient and the three-region structure above is required to model the starting behaviour for the flow more completely. It should be noted, however, that in [22] Wilson demonstrates that top-hat profiles are not particularly realistic in the Sortex set-up, a result which is corroborated by Smith in [19] and [20]. The numerical approximation, on the other hand, has no problem dealing with near-discontinuous profiles and can provide very good approximate solutions for this case, should the need arise.

2.4 Pressure calculation

The main overarching tasks of this research are to study pressure characteristics and interference associated with the multi-jet set-up. Whereas the investigation of interference in the two-dimensional case will prove to be quite enlightening, there is little to be gained from a complete exploration of two-dimensional pressure properties. Therefore, we present here just a brief overview of a method that can be employed to obtain pressure data from the numerical solution.

The non-dimensionalised normal momentum equation

$$u\frac{\partial v}{\partial x} + v\frac{\partial v}{\partial y} = -\frac{\partial p_1}{\partial y} + \frac{\partial^2 v}{\partial y^2} \tag{2.35}$$

can be rearranged to give

$$p_1 = -\int_0^y u\frac{\partial v}{\partial x}dy - \int_0^y v\frac{\partial v}{\partial y}dy + \frac{\partial v}{\partial y} + G(x). \tag{2.36}$$

Now, (2.36) can then be replaced with

$$p_1 = -\int_0^y \left(u\frac{\partial v}{\partial x} + v\frac{\partial u}{\partial x}\right)dy + \int_0^y v\frac{\partial u}{\partial x}dy - \int_0^y v\frac{\partial v}{\partial y}dy + \frac{\partial v}{\partial y} + G(x), \tag{2.37}$$

which implies

$$p_1 = -\frac{\partial}{\partial x}\int_0^y uvdy + \int_0^y v\left(\frac{\partial u}{\partial x} - \frac{\partial v}{\partial y}\right)dy + \frac{\partial v}{\partial y} + G(x). \tag{2.38}$$

However, since $\frac{\partial u}{\partial x} = -\frac{\partial v}{\partial y}$ by (2.1), we obtain

$$p_1 = -\frac{\partial}{\partial x}\left[\int_0^y uvdy\right] - 2\int_0^y v\frac{\partial v}{\partial y}dy + \frac{\partial v}{\partial y} + G(x). \tag{2.39}$$

Finally, then,

$$p_1 = -\frac{\partial}{\partial x}\left[\int_0^y uvdy\right] - v^2 + \frac{\partial v}{\partial y} + G(x). \tag{2.40}$$

Therefore, if we neglect any induced pressure from outside of the jet, so that $p_1 = 0$ at $y = \infty$, then

$$0 = -\frac{\partial}{\partial x}\left[\int_0^\infty uvdy\right] - v_\infty^2 - 0 + G(x).$$

Implying

$$p_1 = -\frac{\partial}{\partial x}\left[\int_{\infty}^{y} uvdy\right] - v_\infty^2 + \frac{\partial v}{\partial y}. \tag{2.41}$$

Therefore,

$$p_1|_{centreline} = \frac{\partial}{\partial x}\left[\int_{0}^{\infty} uvdy\right] - \frac{\partial u}{\partial x}|_{centreline}, \tag{2.42}$$

since $v_{centreline} = 0$ and $\frac{\partial v}{\partial y} = -\frac{\partial u}{\partial x}$.

Here $\frac{\partial u}{\partial x}|_{centreline}$ is known, and $\int_0^\infty uvdy$ may be calculated numerically during the program run. The approach in this section can be used in the next chapter in the investigation of jet interference.

2.5 Small-time analysis of the unsteady jet

As an aside, we develop small-t theory that will provide a useful check in later sections devoted to three-dimensional unsteady jets.

Considering the time-dependent form of (2.1) at small times, $u << 1$ since $u_0 \propto t << 1$, so that $u_0 \sim O(t)$. Then, from the balances $\frac{u}{t} \sim \frac{uu}{x}$ and $u \sim t$, it follows that $x \sim t^2$. This implies that the governing equations are inviscid and fully non-linear to leading order, with zero pressure gradient. Therefore u is conserved for each particle as it moves along.

Suppose now that u_0 is independent of y, so $u = u(x,t)$ for $-a < y < a$, say. Then we might expect that u is independent of y also, and by (2.1), v

is linear in y, leaving

$$\frac{\partial u}{\partial t} + u\frac{\partial u}{\partial x} = 0. \tag{2.43}$$

The characteristics of (2.43) are $\frac{dx}{dt} = u$, on which u is conserved. Therefore, $x = ut + c_1$, and since $u_0 \propto t$ implies $u_0 = bt$, say, it follows that

$$x = bt^2 + c_1 \tag{2.44}$$

confirming the x-scaling above. Hence let $x = \frac{b}{2}t^2$, say, (where $\frac{b}{2}$ is constant and chosen for convenience) then an appropriate similarity variable is $\frac{x}{t^2}$ and we can attempt a similarity solution of (2.43) in the form

$$u = t.U(X), \text{ where } X = \frac{x}{t^2}.$$

Then

$$\frac{\partial u}{\partial t} = U(X) - 2\frac{x}{t^2}U'(X) = U(X) - 2XU'(X), \tag{2.45}$$

(where $'$ denotes differentiation with respect to X), so that (2.43) becomes

$$U(X) - 2XU'(X) + U(X)U'(X) = 0. \tag{2.46}$$

The solution of (2.46) may have to be in two parts joined together with a discontinuity in U or U' at the join. The downstream part has $U \equiv 0$, which satisfies (2.45). The other, upstream, part ($0 < X < X_1$, say) has $U(0) = b$. Therefore, from (2.46), $U' = \frac{U}{2X-U}$, and letting $U = Xw$, say, gives

$$U' = Xw' + w = \frac{U}{2X - U} = \frac{Xw}{2X - Xw} = \frac{w}{2 - w}.$$

So that $Xw' = \frac{w}{2-w}\{w-1\}$. Hence $\int \frac{dX}{X} = \int \frac{2-w}{w(w-1)}dw$ or equivalently $\int \frac{dX}{X} = \int \frac{dw}{w-1} - 2\int \frac{dw}{w}$.

Performing the integration and rearranging gives

$$C_2 - \ln|X| = 2\ln|w| - \ln|w-1|,$$

implying that

$$\frac{w^2}{w-1} = \frac{c_2}{X}. \tag{2.47}$$

However $U = Xw$, so substituting $w = \frac{U}{X}$ into (2.47) gives $\frac{\frac{U^2}{X^2}}{\frac{U}{X}-1} = \frac{c_2}{X}$. From which we obtain

$$X = U(1 - D_2U) \tag{2.48}$$

where $D_2 = \frac{1}{c_2}$.

This leads to three possible solution branches for X, as depicted in figures 2.14, 2.15 and 2.16.

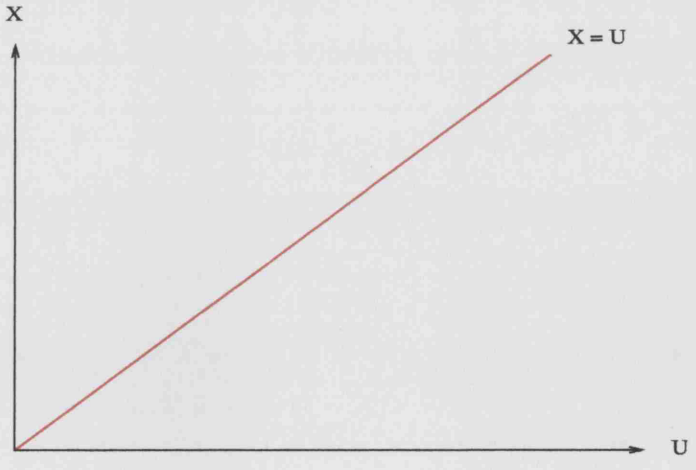

Figure 2.14: X against U, $D_2 = 0$.

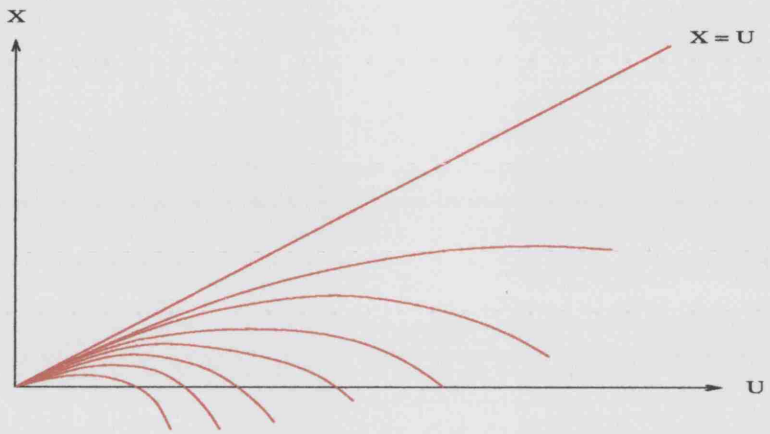

Figure 2.15: X against U, $D_2 > 0$.

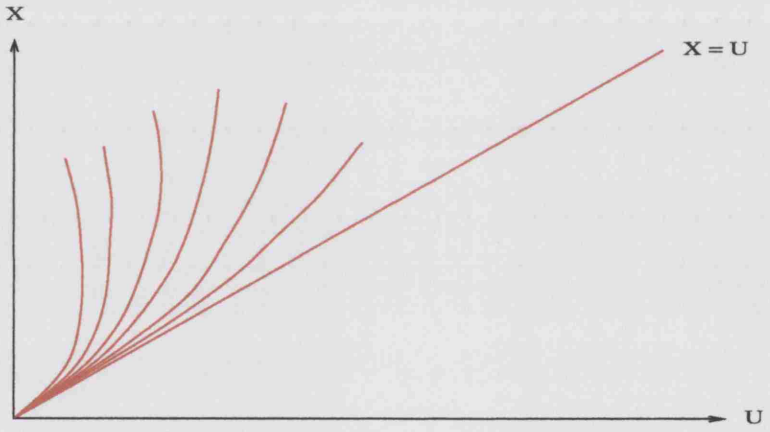

Figure 2.16: X against U, $D_2 < 0$.

Since $U = b$ at $X = 0$, we require the branch for which $D_2 > 0$. This implies that $0 = b(1 - D_2 b)$ and, hence, $D_2 = \frac{1}{b}$. Therefore,

$$X = U\left(1 - \frac{U}{b}\right) \tag{2.49}$$

and the solution looks something like figure 2.17, overleaf.

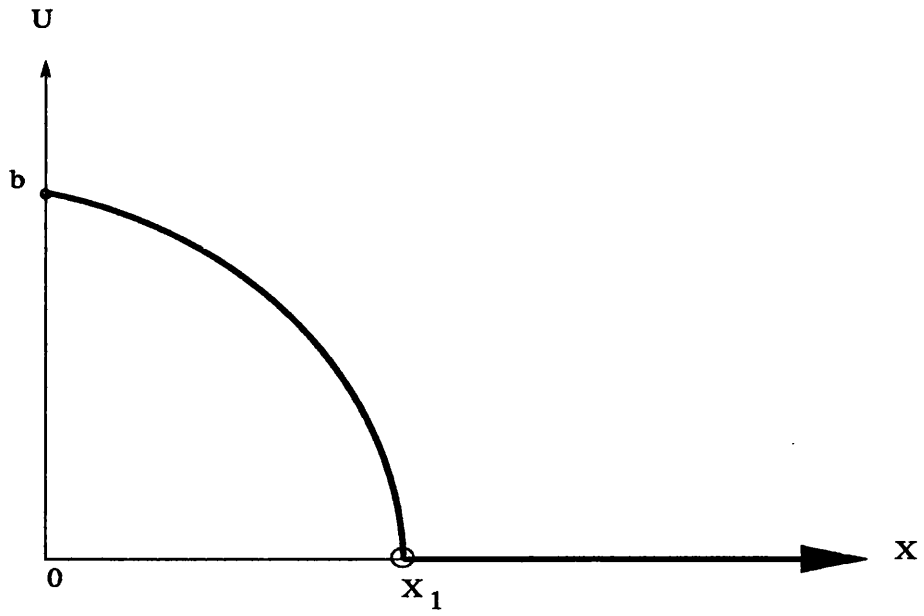

Figure 2.17: U against X. Upstream $(0 < X < X_1)$: $U(0) = b$. Downstream $(X > X_1)$: $U \equiv 0$.

2.5.1 Jet velocity

Differentiating (2.48) with respect to U gives

$$X' = 1 - 2D_2U, \tag{2.50}$$

which is zero when X reaches its maximum. Rearranging (2.50) for U, we find that U has a minimum value of $\frac{1}{2D_2}$. Hence,

$$X_{max} = \frac{1}{2D_2} - D_2\left(\frac{1}{2D_2}\right)^2 = \frac{1}{4D_2}, \tag{2.51}$$

Therefore

$$U_{min} = \frac{1}{2D_2} = 2X_{max}, \tag{2.52}$$

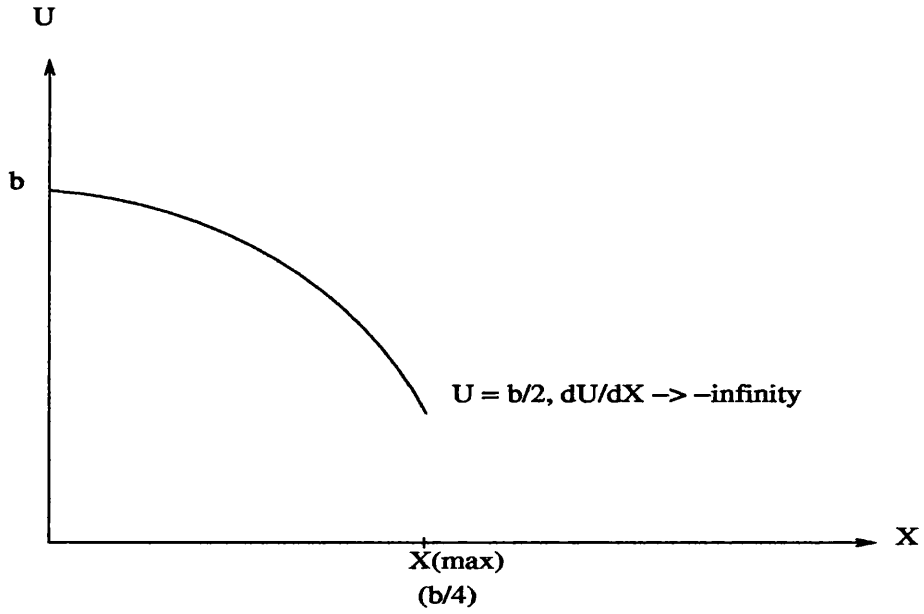

Figure 2.18: The jet's velocity decreases to a minimum value of $2X_{max}$.

which agrees with $\frac{dU}{dX} = \frac{U}{2X-U} \to -\infty$, from (2.46).

Finally then, substituting $D_2 = \frac{1}{b}$, we see that $X_{max} = \frac{b}{4}$ (i.e. $x = \frac{b}{4}t^2$) at which point $U_{min} = \frac{b}{2}$, so the jet flow decelerates as in figure (2.18).

2.5.2 Jet shape

Given that $U = U(x,t)$ only, (1.2) implies $\frac{V}{Y} = -\frac{\partial u}{\partial x}$. Therefore

$$V = -Y\frac{\partial u}{\partial x}. \tag{2.53}$$

Also, from the kinematic condition $\frac{DG}{Dt} = 0$,

$$V = \frac{DY}{Dt} = \frac{\partial F}{\partial t} + u\frac{\partial F}{\partial x} \tag{2.54}$$

on $Y = F(x,t)$.

At the unknown interface $G = Y - F(x,t) = 0$; therefore

$$\frac{\partial F}{\partial t} + u\frac{\partial F}{\partial x} - V = 0$$

so

$$\frac{\partial F}{\partial t} + u\frac{\partial F}{\partial x} + Y\frac{\partial u}{\partial x} = 0.$$

Therefore,

$$\frac{\partial F}{\partial t} + \frac{\partial (uF)}{\partial x} = 0 \tag{2.55}$$

on $Y = F(x,t)$.

For small t we must scale $F \sim F(X)$, where $X \equiv \frac{x}{t^2}$ from earlier. Then

$$\frac{\partial F}{\partial X}(2X - U) = F\frac{\partial U}{\partial X},$$

implying

$$\frac{1}{F}\frac{\partial F}{\partial X} = \frac{1}{(2X-U)}\frac{\partial U}{\partial X}. \tag{2.56}$$

However, $(2X - U)\frac{\partial U}{\partial X} = U$ from (2.46) and $X = U - D_2U^2$ from (2.48). Therefore (2.56) becomes

$$\frac{dF}{F} = \frac{dU}{(2U - 2D_2U^2 - U)} = dU\left[\frac{1}{U} + \frac{2D_2}{(1 - 2D_2U)}\right] \tag{2.57}$$

and after integrating and rearranging we find

$$F = \frac{AU}{(2D_2U - 1)} = \frac{AUb}{2U - b} \tag{2.58}$$

Considering the jet depicted in figure 2.19 then, in which $F = a$ and $U = b$

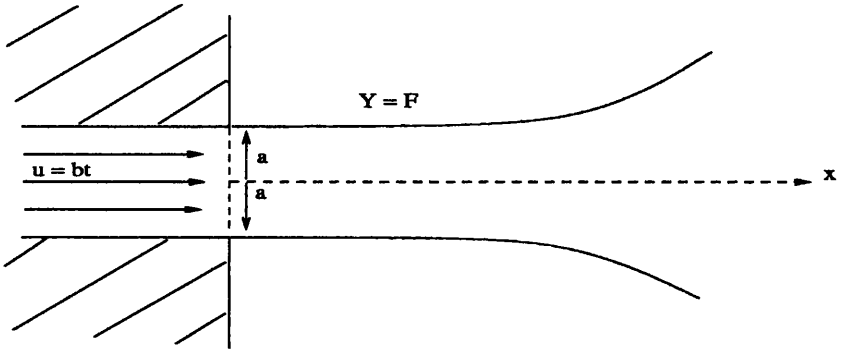

Figure 2.19: slender jet (symmetric about x-axis).

at $x = 0$, (2.58) gives $A = \frac{a}{b} > 0$. However, as $x \to \frac{b}{4}t^2-$, so $X \to \frac{b}{4}-$ and $U \to \frac{b}{2}+$, $F \to \infty$, as in figure 2.20 below.

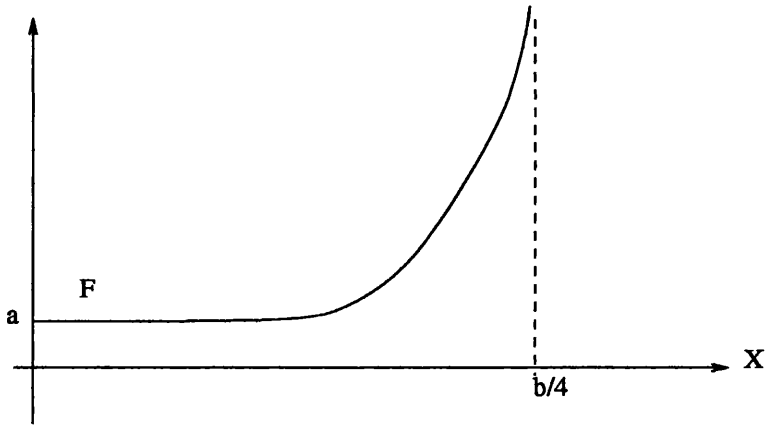

Figure 2.20: inviscid jet 'blow-up'.

Notice also that $V \sim -Y\frac{U'}{t} = -\frac{Y}{t}\left(\frac{U}{2X-U}\right) > 0$. Implying

$$V \to \infty \, as \, X \to \frac{b}{4}- \tag{2.59}$$

In a purely inviscid setting we might expect the trend highlighted by (2.58) and (2.59) to lead on into an *Euler* (square) region (figure 2.21) next, sur-

rounding $x = \frac{b}{4}t^2$. However, in the viscous case the viscous effects must stop the 'blow-up' described above. These effects are investigated next.

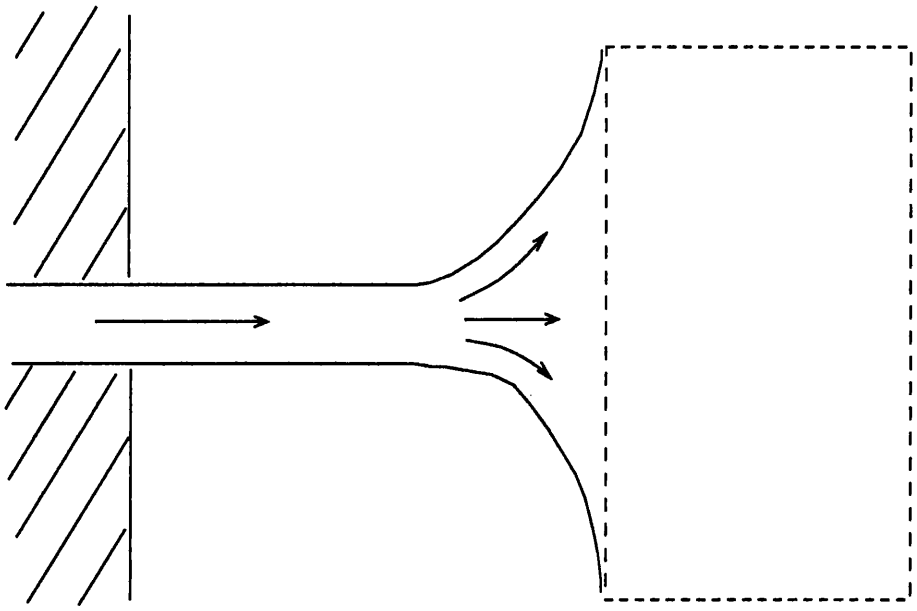

Figure 2.21: inviscid jet and Euler region.

2.5.3 Viscous effects

Viscous effects for small times occur near the edge of the jet, where the momentum balance $\frac{\partial u}{\partial t} \sim \frac{\partial^2 u}{\partial y^2}$ implies $y - F \sim t^{\frac{1}{2}}$. Therefore, putting $y = F + t^{1/2}\hat{y}$, $u = t\hat{U}$ and $v = F_t + uF_x + t^{-1/2}\hat{V}$, along with the Prandtl transposition such that $(x, y, t) \to (\xi, \eta, \hat{t})$ say, where $\xi = \frac{x}{t^2}$; $\eta = \frac{y - F(\frac{x}{t^2})}{t^{1/2}}$ and $\hat{t} = t$, gives

$$v = \frac{-2}{t}\xi\frac{\partial F}{\partial \xi} + \frac{\hat{U}}{t}\frac{\partial F}{\partial \xi} + \frac{1}{t^{1/2}}\hat{V}. \tag{2.60}$$

Also,

$$\frac{\partial}{\partial t} = \frac{\partial}{\partial \xi}\frac{\partial \xi}{\partial t} + \frac{\partial}{\partial \eta}\frac{\partial \eta}{\partial t} + \frac{\partial}{\partial \hat{t}}\frac{\partial \hat{t}}{\partial t} = \frac{-2x}{t^3}\frac{\partial}{\partial \xi} + (\frac{2\xi}{t^{3/2}}\frac{\partial F}{\partial \xi} - \frac{\eta}{2t})\frac{\partial}{\partial \eta} + \frac{\partial}{\partial \hat{t}}$$

So, after substituting $u = t\hat{U}$,

$$\frac{\partial u}{\partial t} = -2\xi\frac{\partial \hat{U}}{\partial \xi} + (\frac{2\xi}{t^{1/2}}\frac{\partial F}{\partial \xi} - \frac{\eta}{2})\frac{\partial \hat{U}}{\partial \eta} + t\frac{\partial \hat{U}}{\partial t} + \hat{U}. \tag{2.61}$$

$$\frac{\partial}{\partial x} = \frac{\partial}{\partial \xi}\frac{\partial \xi}{\partial x} + \frac{\partial}{\partial \eta}\frac{\partial \eta}{\partial x} + \frac{\partial}{\partial \hat{t}}\frac{\partial \hat{t}}{\partial x} = \frac{1}{t^2}\frac{\partial}{\partial \xi} - \frac{1}{t^{5/2}}\frac{\partial F}{\partial \xi}\frac{\partial}{\partial \eta}.$$

So

$$\frac{\partial u}{\partial x} = \frac{1}{t}\frac{\partial \hat{U}}{\partial \xi} - \frac{1}{t^{3/2}}\frac{\partial F}{\partial \xi}\frac{\partial \hat{U}}{\partial \eta}. \tag{2.62}$$

$$\frac{\partial}{\partial y} = \frac{\partial}{\partial \xi}\frac{\partial \xi}{\partial y} + \frac{\partial}{\partial \eta}\frac{\partial \eta}{\partial y} + \frac{\partial}{\partial \hat{t}}\frac{\partial \hat{t}}{\partial y} = \frac{1}{t^{1/2}}\frac{\partial}{\partial \eta},$$

implying

$$\frac{\partial u}{\partial y} = t^{\frac{1}{2}}\frac{\partial \hat{U}}{\partial \eta}. \tag{2.63}$$

$$\frac{\partial^2}{\partial y^2} = \overbrace{\left(\frac{\partial^2}{\partial \xi^2}\frac{\partial \xi}{\partial y} + \frac{\partial^2}{\partial \xi \partial \eta}\frac{\partial \eta}{\partial y} + \frac{\partial^2}{\partial \xi \partial \hat{t}}\frac{\partial \hat{t}}{\partial y}\right)\frac{\partial \xi}{\partial y}}^{=0} + \overbrace{\frac{\partial}{\partial \xi}\frac{\partial^2 \xi}{\partial y^2}}^{=0} +$$

$$\left(\overbrace{\frac{\partial^2}{\partial \eta \partial \xi}\frac{\partial \xi}{\partial y}}^{=0} + \frac{\partial^2}{\partial \eta^2}\frac{\partial \eta}{\partial y} + \overbrace{\frac{\partial^2}{\partial \eta \partial \hat{t}}\frac{\partial \hat{t}}{\partial y}}^{=0}\right)\frac{\partial \eta}{\partial y} + \overbrace{\frac{\partial}{\partial \eta}\frac{\partial^2 \eta}{\partial y^2}}^{=0} + \overbrace{\frac{\partial}{\partial \hat{t}}\frac{\partial^2 \xi}{\partial y^2}}^{=0}$$

$$+ \overbrace{\left(\frac{\partial^2}{\partial \hat{t} \partial \xi}\frac{\partial \xi}{\partial y} + \frac{\partial^2}{\partial \hat{t} \eta}\frac{\partial \eta}{\partial y} + \frac{\partial^2}{\partial \hat{t}^2}\frac{\partial \hat{t}}{\partial y}\right)\frac{\partial \hat{t}}{\partial y}}^{=0}$$

which condenses to leave

$$\frac{\partial^2}{\partial y^2} = \frac{\partial^2}{\partial \eta^2}\left(\frac{\partial \eta}{\partial y}\right)^2 = \frac{1}{t}\frac{\partial^2}{\partial \eta^2}.$$

So that

$$\frac{\partial^2 u}{\partial y^2} = \frac{\partial^2 \hat{U}}{\partial \eta^2} \tag{2.64}$$

Also,

$$\frac{\partial v}{\partial y} = \frac{1}{t^{\frac{1}{2}}}\frac{\partial v}{\partial \eta} = \frac{1}{t^{\frac{3}{2}}}\frac{\partial F}{\partial \xi}\frac{\partial \hat{U}}{\partial \eta} + \frac{1}{t}\frac{\partial \hat{V}}{\partial \eta}. \tag{2.65}$$

Therefore, after making the relevant substitutions, the continuity equation becomes

$$\frac{\partial \hat{U}}{\partial \xi} + \frac{\partial \hat{V}}{\partial \eta} = 0 \tag{2.66}$$

and the momentum equation becomes

$$t\frac{\partial \hat{U}}{\partial \hat{t}} - \frac{\eta}{2}\frac{\partial \hat{U}}{\partial \eta} + \hat{U} - 2\xi\frac{\partial \hat{U}}{\partial \xi} + \hat{U}\frac{\partial \hat{U}}{\partial \xi} + \hat{V}\frac{\partial \hat{U}}{\partial \eta} = \frac{\partial^2 \hat{U}}{\partial \eta^2}. \tag{2.67}$$

Then letting $\hat{t} = t$, $\eta = \hat{y}$ and $\xi = X$ gives the following small-t similarity form.

$$\frac{\partial \hat{U}}{\partial X} + \frac{\partial \hat{V}}{\partial \hat{y}} = 0 \tag{2.68}$$

and

$$t\frac{\partial \hat{U}}{\partial t} - \frac{\hat{y}}{2}\frac{\partial \hat{U}}{\partial \hat{y}} + \hat{U} - 2X\frac{\partial \hat{U}}{\partial X} + \hat{U}\frac{\partial \hat{U}}{\partial X} + \hat{V}\frac{\partial \hat{U}}{\partial \hat{y}} = \frac{\partial^2 \hat{U}}{\partial \hat{y}^2}, \tag{2.69}$$

subject to $\hat{U} \to 0$ as $\hat{y} \to \infty$ and $\hat{U} \to U(X)$ as $\hat{y} \to -\infty$,

where U satisfies $U'(2X - U) = U$.

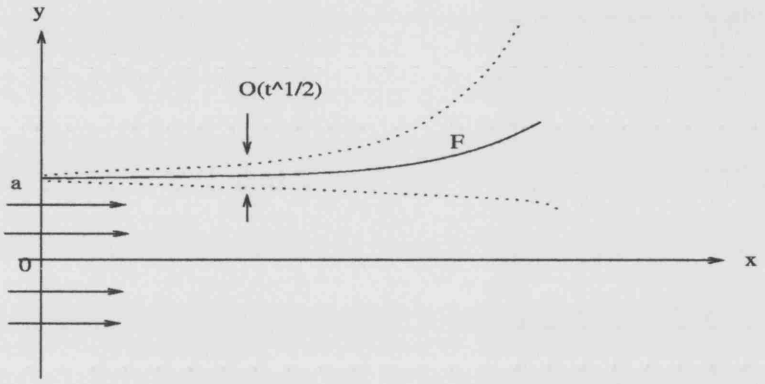

Figure 2.22: Viscous layer.

In conclusion then, it has been shown that as X increases U falls. Implying that the viscous layer is decelerated. Viscous layers thicken as a consequence of deceleration. The deceleration term $\frac{\partial u}{\partial x} \sim \frac{1}{t}\frac{\partial U}{\partial X}$. Thus $\frac{\partial U}{\partial X} \to -\infty$ as $X \to \frac{b}{4}-$. This unbounded deceleration may cause the viscous-layer thickness to tend to ∞ (relative to its original $t^{\frac{1}{2}}$ scaling) and then allow viscous effects to influence, and possibly contain, the spread highlighted in figure 2.20.

2.6 Summary

In summary of the main points, Chapter 2 has presented the governing equations of the two-dimensional jet and described their numerical solution for a number of appropriate cases. Analytical properties have also been explored, notably for small or large distances. The small-distance analysis has been found to be not only particularly relevant in the industrial setting but also

to agree reasonably well with the numerical results, depending on the starting conditions. Pressure evaluation and small-time analysis for unsteady jets have also been introduced

The in-depth study of two-dimensional jets has helped prepare the way for our exploration of three-dimensional jets, which is contained in chapters 4, 5 and 6. The finite difference methods used in Chapter 2 will be extended to solve the three-dimensional steady and unsteady cases. Pressure equations analogous to that presented in the two-dimensional case will be developed and used in the three-dimensional cases and small-distance analysis (subject to the limitations highlighted) will be employed to complement the numerical solutions.

Chapter 3

Interference aspects of multiple in-line two-dimensional jets

3.1 Introduction

This chapter addresses the major issue of interference between jets.

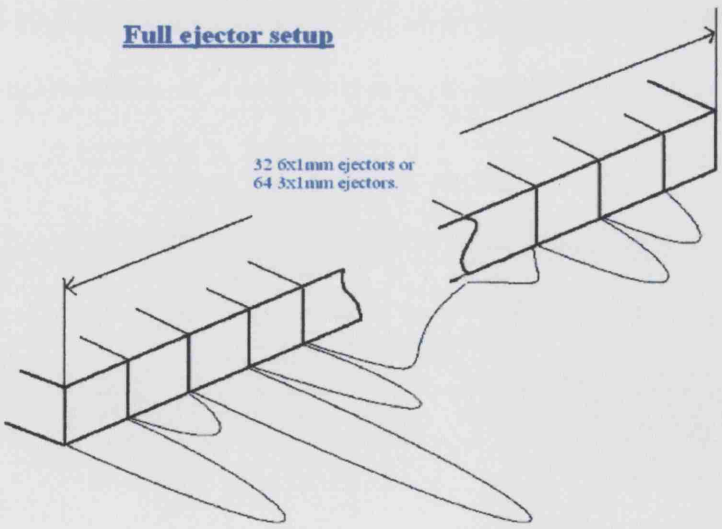

Figure 3.1: Schematic of full $3D$ ejector set-up.

Figure 3.1 illustrates how ejector nozzles in a food sorting machine may be arranged. Typically, in Sortex machines, there exists a single row of several narrow ducts of 3×1mm, 4×1mm or 6×1mm cross-section. Each of these is separated from its immediate neighbour by a 0.5mm gap, which is governed by the thickness of the ejector walls. The ejectors all fire independently of each other in response to defect items in their target areas. Each ejector may fire between 100 and 300 times every second and, hence, it is anticipated that there may be considerable effects from interference between the jets. The modelling of these interference characteristics forms a major part of the entire study here.

In this chapter, then, the numerical marching scheme demonstrated in Chapter 2 will be employed to investigate the development of several or many jets from an imposed laterally symmetric steady initial profile. [The case of interference between several or many wakes has been studied by Smith in [9]].The results obtained will be discussed and then interpreted analytically, once again using techniques outlined in Chapter 2.

3.2 Numerical investigation

The governing equations, then, are (1.2) and (2.1), and these are subject to the conditions given by (2.13) and (2.14). Now, however, for the purposes of addressing interference we consider the initial profile

$$u_0 = \left[1 + \left(6 \sin\left(\frac{y}{2}\right)\right)^2\right]^{-1} \tag{3.1}$$

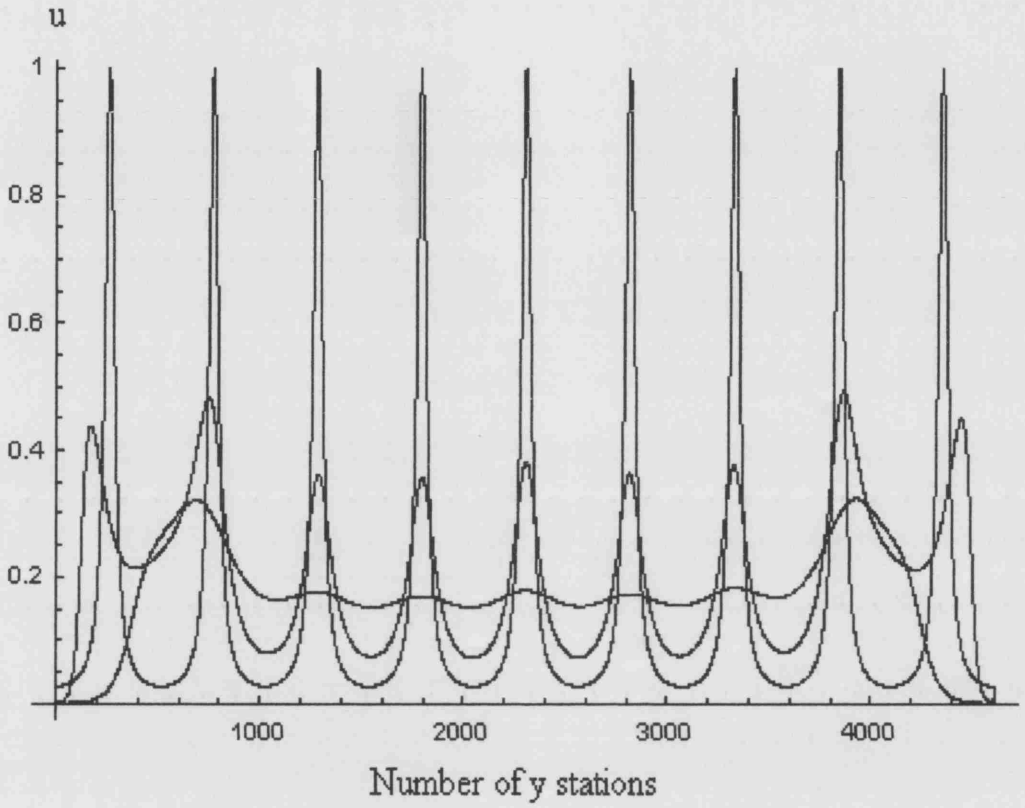

Figure 3.2: $u_0 = \left[1 + \left(6 \sin\left(\frac{y}{2}\right)\right)^2\right]^{-1}$, $-9\pi \leq y \leq 9\pi$, $x = 0,\ 0.1,\ 0.5$.

(which is 2π periodic in y and symmetric about $y = 0$) for $-N\pi \leq y \leq N\pi$, for some odd natural number N. Results for $N = 9$ at $x = 0,\ 0.1$, and 0.5 are presented in figure 3.2.

The plots at first appear to show a maintained lateral periodicity equal to that of u_0 within the central region of the total flow up to at least x = 0.5. However, close inspection of the numerical results for $N = 19$ suggests that in reality there is no such periodicity. For instance, at $x = 0.1$ in the case of $N = 19$, the widths of the jets either side of the central jet decrease

from 2π to approximately 1.96π, whereas the widths of those further out increase in response to the presence of the jets at the outer edges. The peaks and troughs of the middle region eventually merge and smooth, as seen in figure 3.3, and the profile progresses towards the 'Bickley-jet' form. The influence from the edges is gradually absorbed; however, this occurs a long way downstream. The characteristic streamwise length, L, of this viscous system is approximately 1370mm and the characteristic width δ is $1mm$ (this being the semi-width of the jets). Therefore the coalescence shown in figure 3.3 happens well beyond the 150mm range of interest to Sortex. However, the edge effects are a dominant feature within the Sortex range, and these play a major part in the interference.

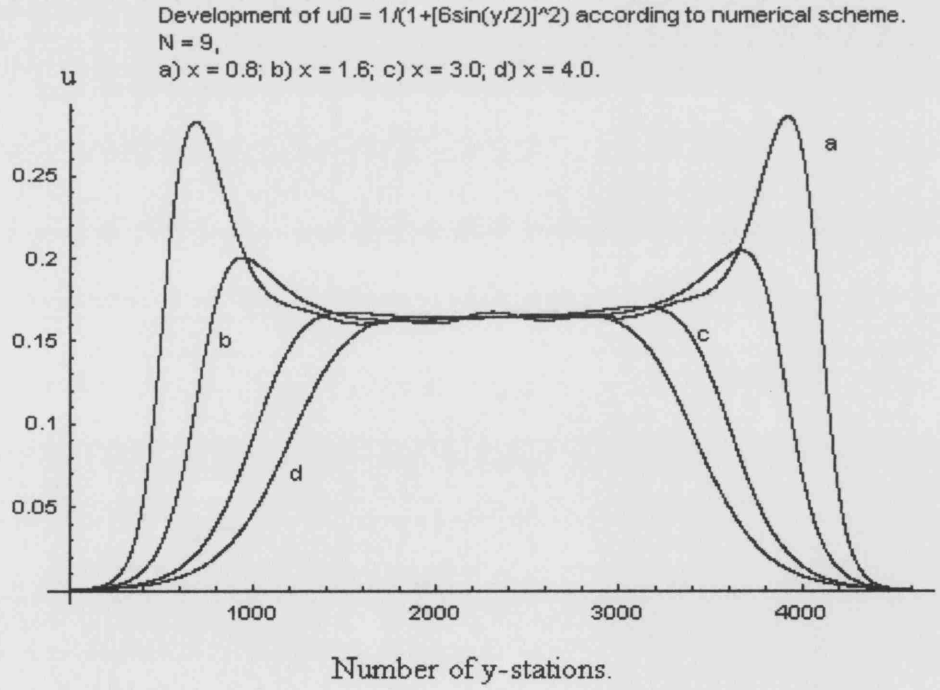

Figure 3.3: $u_0 = \left[1 + \left(6 \sin\left(\frac{y}{2}\right)\right)^2\right]^{-1}$, $-9\pi \leq y \leq 9\pi$, $x = 0.8, 1.6, 3.0, 4.0$.

3.3 Analysing the numerical results

Consider the initial profile $u_0 = \left[1 + \left(6 \sin\left(\frac{y}{2}\right)\right)^2\right]^{-1}$ again, which is periodic in y, with period 2π, and suppose that the profile remains periodic. Then integration of the momentum equation with respect to y across the 2π period would give the integral of u^2 being conserved for all x (see (2.5)) and equal to $\frac{38\pi}{37\sqrt{37}}$, which is approximately 0.5304. A uniform state is anticipated downstream (as predicted by the numerical results, and illustrated in figure 3.3) in which $u \to c$; here, to conserve the u^2 integral in y between $-\pi$ and π, $c = \sqrt{\frac{19}{37\sqrt{37}}}$, a value which is approximately 0.2906.

In contrast the numerical results have been shown NOT to be periodic in y; moreover the uniform state downstream is found to have $u < 0.2$, which is clearly distinct from the value of c just above. The reason or resolution for the contrast is that the flow does not generally maintain y-periodicity: this is a result of the significant interference present.

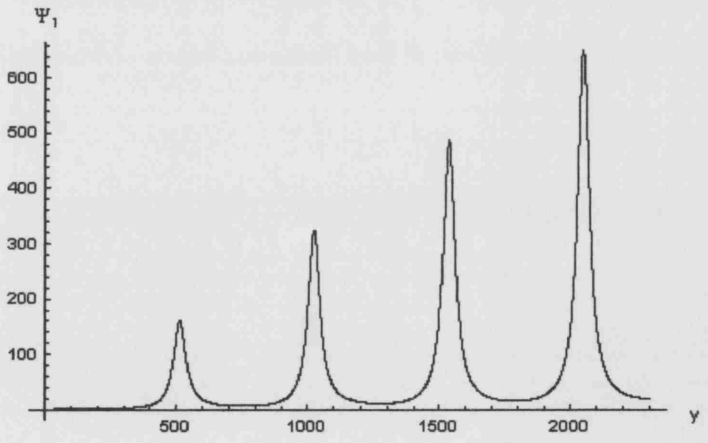

Figure 3.4: ψ_1 vs y for $u_0 = \frac{1}{(1+(6\sin(\frac{y}{2}))^2)}, 0 \leq y \leq N$, $N = 9\pi$.

3.4 Small-x analysis

Small-distance analysis of the form introduced in Chapter 2 further supports the above findings. The flow solutions expand as (2.26), where ψ is the stream function; so u_1 is given by (2.28). Plots of ψ_1 against y and u_1 against y are presented in figures 3.4 and 3.5. Close examination of these confirms the lack of periodicity in y, and an apparent linear growth in u_1 with y.

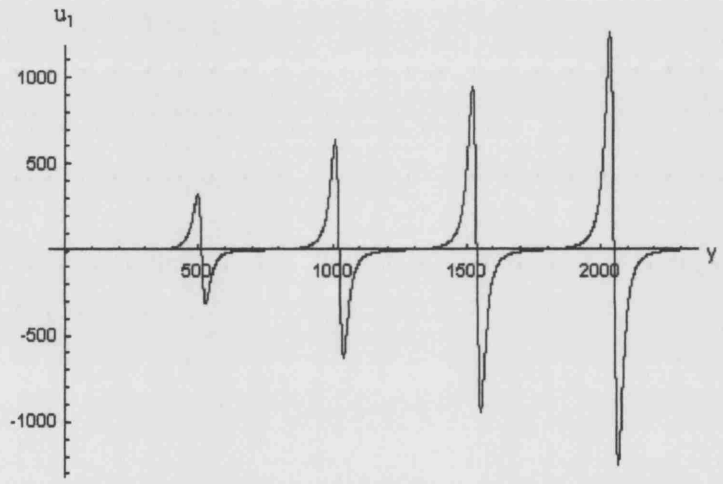

Figure 3.5: u_1 vs y for $u_0 = \frac{1}{(1+6\sin^2(\frac{y}{2}))}, 0 \leq y \leq N,\ N = 9\pi.$

3.5 Summary

In conclusion then, it has been shown that even when considering jets operating over relatively short distances, as in the Sortex case, neighbouring jets will interfere with each other. This interference appears to be influenced greatly by edge effects, as clearly shown in the above plots. Furthermore, it

has been shown that even if the initial u_0 profile is periodic the initial lateral velocity component, $v_0 = -\psi_1$, will be non-zero and non-periodic. This last point goes some way to explaining deficiencies in the pressure solution at very small x, a matter which is discussed in the next chapter, along with a method investigated for overcoming the deficiencies.

Chapter 4

Three-Dimensional Steady Jets

4.1 Introduction

In this chapter the finite difference schemes employed to solve the two-dimensional case will be extended to enable us to investigate the development of steady three-dimensional jets. We begin by obtaining the governing equations for the three-dimensional steady jet and describing their numerical treatment; this is by means of what is in effect a vorticity-velocity formulation. The extra use of small-distance analysis and a cross-planar stream-function formulation are explored in an attempt to overcome deficiencies in the early development of the numerical pressure solution.

The main aim in this chapter, and the next, will be to obtain pressure data that can be compared directly with empirical data supplied by Sortex. However, it should be noted that the empirical data could only be captured over a very short range of approximately 15mm from the nozzle exit; beyond this

range the sensory equipment was unable to accurately measure the air blast. Furthermore, it should be noted that even over the range where data was regarded as acceptable there are fluctuations in the readings. It must also be stressed that the empirical data, unlike the numerical solution discussed in this chapter, is time dependent and any comparisons should really be confined to the unsteady solution that will be developed in Chapter 5.

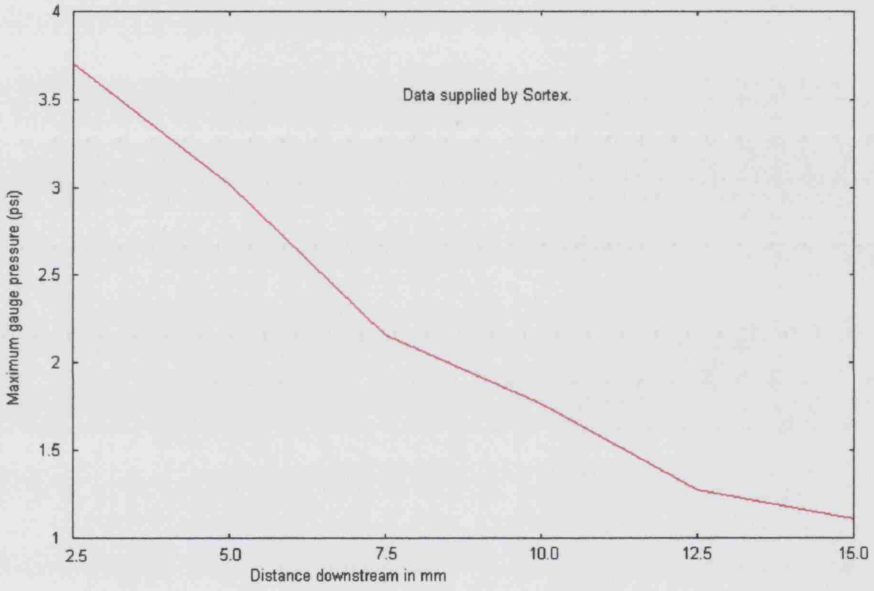

Figure 4.1: Maximum gauge pressures between 2.5mm and 15mm from the nozzle exit supplied by Sortex.

4.2 Governing equations

We take as our starting point the three-dimensional continuity equation and the Cartesian three-dimensional Navier-Stokes momentum equations: 1.5,

1.6, 1.7, from which we discount time dependence so that we are left with:

$$u\frac{\partial u}{\partial x}+v\frac{\partial u}{\partial y}+w\frac{\partial u}{\partial z} = \frac{-1}{\rho}\frac{\partial p}{\partial x}+\frac{\mu}{\rho}\{\frac{\partial^2 u}{\partial x^2}+\frac{\partial^2 u}{\partial y^2}+\frac{\partial^2 u}{\partial z^2}\}, \tag{4.1}$$

$$u\frac{\partial v}{\partial x}+v\frac{\partial v}{\partial y}+w\frac{\partial v}{\partial z} = \frac{-1}{\rho}\frac{\partial p}{\partial y}+\frac{\mu}{\rho}\{\frac{\partial^2 v}{\partial x^2}+\frac{\partial^2 v}{\partial y^2}+\frac{\partial^2 v}{\partial z^2}\}, \tag{4.2}$$

$$u\frac{\partial w}{\partial x}+v\frac{\partial w}{\partial y}+w\frac{\partial w}{\partial z} = \frac{-1}{\rho}\frac{\partial p}{\partial z}+\frac{\mu}{\rho}\{\frac{\partial^2 w}{\partial x^2}+\frac{\partial^2 w}{\partial y^2}+\frac{\partial^2 w}{\partial z^2}\}. \tag{4.3}$$

Dimensional analysis of this system of equations suggests that, as in the two-dimensional case earlier, the second-order derivative with respect to x in each equation is small enough to be ignored. Hence, the governing boundary-layer equations for the three-dimensional steady jet are, as in the two-dimensional case, parabolic in x provided the velocity component u remains positive. This indicates that the numerical scheme required for their solution should be of the downstream marching type. Therefore we consider the following non-dimensionalised system of equations:

$$u\frac{\partial u}{\partial x}+v\frac{\partial u}{\partial y}+w\frac{\partial u}{\partial z} = \frac{-1}{\rho}\frac{\partial p}{\partial x}+\{\frac{\partial^2 u}{\partial y^2}+\frac{\partial^2 u}{\partial z^2}\}, \tag{4.4}$$

$$u\frac{\partial v}{\partial x}+v\frac{\partial v}{\partial y}+w\frac{\partial v}{\partial z} = \frac{-1}{\rho}\frac{\partial p}{\partial y}+\{\frac{\partial^2 v}{\partial y^2}+\frac{\partial^2 v}{\partial z^2}\}, \tag{4.5}$$

$$u\frac{\partial w}{\partial x}+v\frac{\partial w}{\partial y}+w\frac{\partial w}{\partial z}=\frac{-1}{\rho}\frac{\partial p}{\partial z}+\{\frac{\partial^2 w}{\partial y^2}+\frac{\partial^2 w}{\partial z^2}\}, \tag{4.6}$$

$$\frac{\partial u}{\partial x}+\frac{\partial v}{\partial y}+\frac{\partial w}{\partial z}=0, \tag{4.7}$$

subject to the following boundary conditions:

$u \to 0$ as $|y| \to \infty$, $u \to 0$ as $|z| \to \infty$, $\frac{\partial u}{\partial y}=0$ at $y=0$ and $\frac{\partial u}{\partial z}=0$ at $z=0$,

and a starting condition at $x=0$ say. The pressure p is now of the form $p=p_0(x,y,z)+\frac{1}{Re}p_1(x,y,z)+...$ and it follows immediately from equations 4.5 and 4.6 that $\frac{\partial p_0}{\partial y}$ and $\frac{\partial p_0}{\partial z}$ are zero, indicating that the system to be solved requires $p_1(x,y,z)$ to be considered. Also from the boundary conditions at large $|y|$ we find that p_0 is constant, implying the result that $\frac{\partial p_0}{\partial x}=0$.

In preparation for solving the above system for u, v, w, with p_1, (see [27], [28]), first 4.7 can be rearranged to give $\frac{\partial v}{\partial y}=-(\frac{\partial u}{\partial x}+\frac{\partial w}{\partial z})$ and $\frac{\partial w}{\partial z}=-(\frac{\partial u}{\partial x}+\frac{\partial v}{\partial y})$. Therefore, substituting these into 4.5 and 4.6, respectively, gives:

$$u\frac{\partial v}{\partial x}+v\frac{\partial v}{\partial y}+w\frac{\partial v}{\partial z}=-\frac{1}{\rho}\frac{\partial p_1}{\partial y}+\frac{\partial}{\partial z}\{\frac{\partial v}{\partial z}-\frac{\partial w}{\partial y}\}-\frac{\partial^2 u}{\partial x \partial y} \tag{4.8}$$

and

$$u\frac{\partial w}{\partial x}+v\frac{\partial w}{\partial y}+w\frac{\partial w}{\partial z}=-\frac{1}{\rho}\frac{\partial p_1}{\partial z}+\frac{\partial}{\partial y}\{\frac{\partial w}{\partial y}-\frac{\partial v}{\partial z}\}-\frac{\partial^2 u}{\partial x \partial z}. \tag{4.9}$$

Defining the cross-planar vorticity $\zeta = \frac{\partial v}{\partial z} - \frac{\partial w}{\partial y}$ we can then rewrite 4.8 and 4.9 as

$$u\frac{\partial v}{\partial x} + v\frac{\partial v}{\partial y} + w\frac{\partial v}{\partial z} = -\frac{1}{\rho}\frac{\partial p_1}{\partial y} + \frac{\partial \zeta}{\partial z} - \frac{\partial^2 u}{\partial x \partial y} \tag{4.10}$$

and

$$u\frac{\partial w}{\partial x} + v\frac{\partial w}{\partial y} + w\frac{\partial w}{\partial z} = -\frac{1}{\rho}\frac{\partial p_1}{\partial z} - \frac{\partial \zeta}{\partial y} - \frac{\partial^2 u}{\partial x \partial z}. \tag{4.11}$$

We may then eliminate the pressure terms by differentiating 4.10 with respect to z, differentiating 4.11 with respect to y, and then subtracting one of the resulting equations from the other, to obtain

$$u\tfrac{\partial}{\partial x}\{\tfrac{\partial v}{\partial z} - \tfrac{\partial w}{\partial y}\} + v\tfrac{\partial}{\partial y}\{\tfrac{\partial v}{\partial z} - \tfrac{\partial w}{\partial y}\} + w\tfrac{\partial}{\partial z}\{\tfrac{\partial v}{\partial z} - \tfrac{\partial w}{\partial y}\} + \tfrac{\partial v}{\partial y}\{\tfrac{\partial v}{\partial z} - \tfrac{\partial w}{\partial y}\}$$
$$+\tfrac{\partial w}{\partial z}\{\tfrac{\partial v}{\partial z} - \tfrac{\partial w}{\partial y}\} + \tfrac{\partial u}{\partial z}\tfrac{\partial v}{\partial x} - \tfrac{\partial u}{\partial y}\tfrac{\partial w}{\partial x} = \nabla^2\{\tfrac{\partial v}{\partial z} - \tfrac{\partial w}{\partial y}\},$$

where $\nabla^2 = (\frac{\partial^2}{\partial y^2} + \frac{\partial^2}{\partial z^2})$.

This then gives in effect an equation for the vorticity evolution,

$$\nabla^2 \zeta = u\frac{\partial \zeta}{\partial x} + v\frac{\partial \zeta}{\partial y} + w\frac{\partial \zeta}{\partial z} + \zeta\frac{\partial v}{\partial y} + \zeta\frac{\partial w}{\partial z} + \frac{\partial u}{\partial z}\frac{\partial v}{\partial x} - \frac{\partial u}{\partial y}\frac{\partial w}{\partial x}. \tag{4.12}$$

Also, $\frac{\partial^2 v}{\partial y^2} \equiv -\frac{\partial}{\partial y}(\frac{\partial u}{\partial x} + \frac{\partial w}{\partial z})$. Therefore, in terms of the vorticity,

$$\nabla^2 v = \frac{\partial \zeta}{\partial z} - \frac{\partial^2 u}{\partial x \partial y} \tag{4.13}$$

can be regarded (see below) as an equation controlling v, while

$$\nabla^2 w = -\frac{\partial \zeta}{\partial y} - \frac{\partial^2 u}{\partial x \partial z}. \tag{4.14}$$

acts as if to control w. Hence, employing 4.12, 4.13 and 4.14 along with

$$\nabla^2 u = u\frac{\partial u}{\partial x} + v\frac{\partial u}{\partial y} + w\frac{\partial u}{\partial z}, \tag{4.15}$$

the three-dimensional steady incompressible jet problem is now in a form suitable to be solved numerically, as we see in the next section.

4.3 Numerical solution

We first consider 4.15, which after a discretization as described below can essentially be solved using Gauss-Jordan elimination. To account for the boundary conditions the matrix is extended to $(n+2)$ x $(n+2)$ and the value of u is set to zero at all boundary nodes.

As in the two-dimensional case, the undifferentiated terms are taken to be known values from the previous station or initial conditions; this acts as a local or quasi-linearization. A *backward* difference in x is used to model $\frac{\partial u}{\partial x}$ at the current station and *centred* differences are used to model the derivatives with respect to y and z. Hence the difference scheme for 4.15 is

$$\overline{U}_{m,n}\left(\frac{U_{m,n}-\overline{U}_{m,n}}{\Delta x}\right) + \overline{V}_{m,n}\left(\frac{U_{m+1,n}-U_{m-1,n}}{2\Delta y}\right) + \overline{W}_{m,n}\left(\frac{U_{m,n+1}-U_{m,n-1}}{2\Delta z}\right)$$
$$= \left(\frac{U_{m+1,n}-2U_{m,n}+U_{m-1,n}}{(\Delta y)^2}\right) + \left(\frac{U_{m,n+1}-2U_{m,n}+U_{m,n-1}}{(\Delta z)^2}\right),$$

which we rearrange to form

$$(\frac{\overline{V}_{m,n}}{2\Delta y}-\frac{1}{(\Delta y)^2})U_{m+1,n}+2(\frac{1}{(\Delta y)^2}+\frac{1}{(\Delta z)^2}+\frac{\overline{U}_{m,n}}{2\Delta x})U_{m,n}-(\frac{1}{(\Delta y)^2}+\frac{\overline{V}_{m,n}}{2\Delta y})U_{m-1,n}$$

$$+(\frac{\overline{W}_{m,n}}{2\Delta z}-\frac{1}{(\Delta z)^2})U_{m,n+1}-(\frac{1}{(\Delta z)^2}+\frac{\overline{W}_{m,n}}{2\Delta z})U_{m,n-1}=\frac{\overline{U}^2_{m,n}}{\Delta x}, \qquad (4.16)$$

where U, V, W represent the velocity components u, v and w, respectively.

Once the u values have been calculated at the current x-station the associated v, w and ζ values may be approximated using an iterative scheme.

4.3.1 Gauss-Jacobi iterative scheme

Here iterative solution methods generate a sequence of approximations to the exact solution, and it is found that in the present context they can indeed be made to converge to an acceptable level of accuracy. Although the exact solution is not produced these methods have the advantage of requiring less computer storage and are relatively easy to program.

Here we employ the Gauss-Jacobi scheme (see, for instance, [26], [37]) to solve the above system of equations. This is a point-iterative scheme since each quantity is updated one grid point at a time. This particular method was chosen because it works independently of the order in which the nodes are scanned, making programming simpler, and also because it seemed to work in practice fairly efficiently.

4.3.2 Solution of the three-dimensional jet

The individual terms of equations 4.12, 4.13 and 4.14 are replaced by their corresponding difference terms to yield the following finite-difference equations:

$$\left(\frac{newV_{m+1,n} - 2newV_{m,n} + newV_{m-1,n}}{(\Delta y)^2}\right)$$

$$+\left(\frac{newV_{m,n+1} - 2newV_{m,n} + newV_{m,n-1}}{(\Delta z)^2}\right)$$

$$= \left(\frac{new\zeta_{m,n+1} - new\zeta_{m,n-1}}{2\Delta z}\right) - \left(\frac{U_{m+1,n} - U_{m-1,n} - \overline{U}_{m+1,n} + \overline{U}_{m-1,n}}{2\Delta x \Delta y}\right);$$

$$\left(\frac{newW_{m+1,n} - 2newW_{m,n} + newW_{m-1,n}}{(\Delta y)^2}\right)$$

$$+\left(\frac{newW_{m,n+1} - 2newW_{m,n} + newW_{m,n-1}}{(\Delta z)^2}\right)$$

$$= \left(\frac{new\zeta_{m+1,n} - new\zeta_{m-1,n}}{2\Delta y}\right) - \left(\frac{U_{m,n+1} - U_{m,n-1} - \overline{U}_{m,n+1} + \overline{U}_{m,n-1}}{2\Delta x \Delta z}\right)$$

and

$$U_{m,n}\left(\frac{new\zeta_{m,n} - \overline{\zeta}_{m,n}}{\Delta x}\right) + newV_{m,n}\left(\frac{old\zeta_{m+1,n} - old\zeta_{m-1,n}}{2\Delta y}\right) +$$

$$newW_{m,n}\left(\frac{old\zeta_{m,n+1} - old\zeta_{m,n-1}}{2\Delta z}\right) + old\zeta_{m,n}\left(\frac{newV_{m+1,n} - newV_{m-1,n}}{2\Delta y}\right) +$$

$$old\zeta_{m,n}\left(\frac{newW_{m,n+1} - newW_{m,n-1}}{2\Delta z}\right) + \left(\frac{U_{m,n+1} - U_{m,n-1}}{2\Delta z}\right)\left(\frac{newV_{m,n} - \overline{V}_{m,n}}{\Delta x}\right) -$$

$$\left(\frac{U_{m+1,n} - U_{m-1,n}}{2\Delta y}\right)\left(\frac{newW_{m,n} - \overline{W}_{m,n}}{\Delta x}\right)$$

$$= \left(\frac{old\zeta_{m+1,n} - 2old\zeta_{m,n} + old\zeta_{m-1,n}}{(\Delta y)^2}\right) + \left(\frac{old\zeta_{m,n+1} - 2old\zeta_{m,n} + old\zeta_{m,n-1}}{(\Delta z)^2}\right),$$

where '*old*' values are previously known or initially guessed at the present x-station, '$\overline{barred}$' values are values known from the previous x-station and the '*new*' values are to be found.

Therefore,

$$newV_{m,n} =$$

$$\frac{(\Delta y \Delta z)^2}{2(\Delta y^2 + \Delta z^2)}\{(\frac{newV_{m+1,n} + newV_{m-1,n}}{\Delta y^2}) + (\frac{newV_{m,n+1} + newV_{m,n-1}}{\Delta z^2})$$

$$-(\frac{new\zeta_{m,n+1} - new\zeta_{m,n-1}}{2\Delta z}) + (\frac{U_{m+1,n} - U_{m-1,n} - \overline{U}_{m+1,n} + \overline{U}_{m-1,n}}{2\Delta x \Delta y})\} \tag{4.17}$$

$$newW_{m,n} =$$

$$\frac{(\Delta y \Delta z)^2}{2(\Delta y^2 + \Delta z^2)}\{(\frac{newW_{m+1,n} + newW_{m-1,n}}{\Delta y^2}) + (\frac{newW_{m,n+1} + newW_{m,n-1}}{\Delta z^2})$$

$$+(\frac{new\zeta_{m+1,n} - new\zeta_{m-1,n}}{2\Delta y}) + (\frac{U_{m,n+1} - U_{m,n-1} - \overline{U}_{m,n+1} + \overline{U}_{m,n-1}}{2\Delta x \Delta z})\} \tag{4.18}$$

$$new\zeta_{m,n} =$$

$$(\frac{\Delta x}{U_{m,n}})\{(\frac{old\zeta_{m+1,n} - 2old\zeta_{m,n} + old\zeta_{m-1,n}}{(\Delta y)^2}) + (\frac{old\zeta_{m,n+1} - 2old\zeta_{m,n} + old\zeta_{m,n-1}}{(\Delta z)^2})$$

$$+(\frac{U_{m+1,n} - U_{m-1,n}}{2\Delta y})(\frac{newW_{m,n} - \overline{W}_{m,n}}{\Delta x}) - (\frac{U_{m,n+1} - U_{m,n-1}}{2\Delta z})(\frac{newV_{m,n} - \overline{V}_{m,n}}{\Delta x})$$

$$-old\zeta_{m,n}\left(\frac{newW_{m,n+1}-newW_{m,n-1}}{2\Delta z}\right)-old\zeta_{m,n}\left(\frac{newV_{m+1,n}-newV_{m-1,n}}{2\Delta y}\right)$$

$$-newW_{m,n}\left(\frac{old\zeta_{m,n+1}-old\zeta_{m,n-1}}{2\Delta z}\right)-newV_{m,n}\left(\frac{old\zeta_{m+1,n}-old\zeta_{m-1,n}}{2\Delta y}\right)\}+\overline{\zeta}_{m,n} \tag{4.19}$$

Values obtained from 4.16, along with known $\overline{U}$ values and initial or latest values for *'old'* terms are fed successively into 4.17, 4.18 and 4.19, at each stage iterating to an acceptable (pre-defined) level of convergence. Once the solution of 4.19 meets the convergence criterion the *'new'* values are re-fed into 4.17 and the iterative process is repeated until there is overall convergence via equations 4.17, 4.18 and 4.19. The process then steps forward to the next x-station and the process is repeated, and so on.

4.4 Validation of the numerical scheme

As with the two-dimensional scheme, it is possible to validate the numerical solution by employing tests which fix the boundary of the solution domain but which vary either the size and hence number of Δy and Δz steps (i.e. number of grid-nodes) or the size and number of Δx steps.

With the solution domain fixed and with Δx held constant at a prescribed x-station the solution produced the parabolic curve, illustrated in figure 4.2, of $U|_{y=0}$ as Δy and Δz were increased. This agreed with expectations, since both the Δy and the Δz are discretizations of second order accuracy, due to their centring.

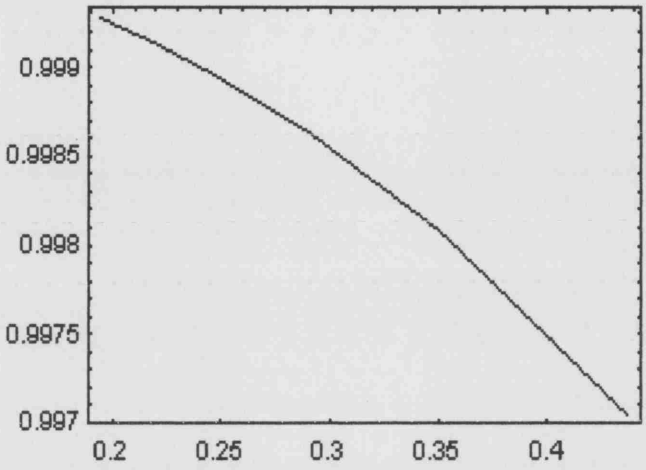

Figure 4.2: Fixed solution domain, increasing Δy and Δz at prescribed x-station. Horizontal axis gives Δy and Δz values; vertical axis gives centreline velocity.

Similarly, holding Δy and Δz constant at a prescribed x-station within a fixed solution domain produced the straight line graph $U|_{y=0}$ against Δx in figure 4.3, in keeping with the first order accuracy of the Δx discretization. (Higher order accuracy in x is discussed in the papers above).

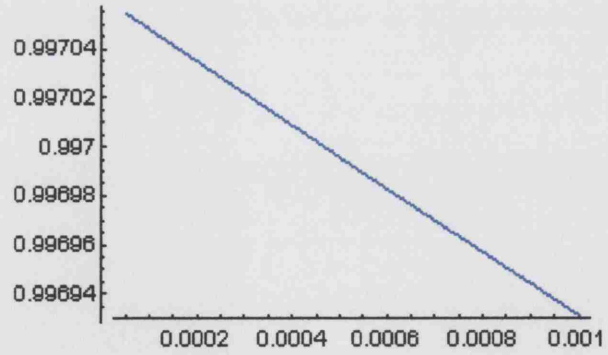

Figure 4.3: Fixed solution domain, increasing Δx at prescribed x-station.

Figure 4.4 illustrates the centreline velocities produced by grids of increasing

refinement but with fixed solution domains. The RED curve was obtained from a grid in which $\Delta y = \Delta z = 7/12$; the GREEN curve was obtained from a grid in which $\Delta y = \Delta z = 7/16$; the BLUE curve was obtained from a grid in which $\Delta y = \Delta z = 7/20$ and the MAGENTA curve was obtained from a grid in which $\Delta y = \Delta z = 7/24$. The vertical axis represents the centreline velocity and the horizontal axis indicates the value of x.

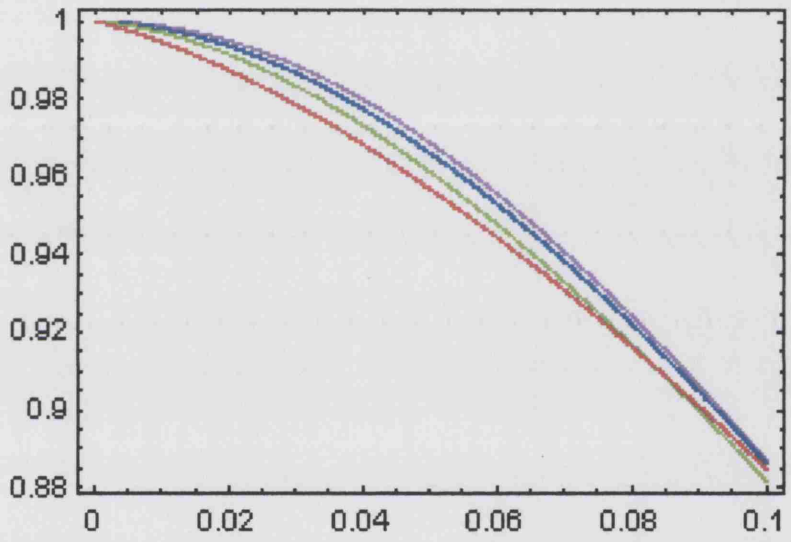

Figure 4.4: centreline velocities produced by refining Δy and Δz.

The overall trend is clearly towards the MAGENTA curve. However the BLUE curve was produced by a grid containing a total of 81 interior nodes and shows only marginal disagreement with the MAGENTA curve, generated by a more computationally expensive grid containing 121 interior nodes. Therefore, in any further work involving this numerical scheme, a grid containing 81 interior nodes will be used.

4.5 Leading order small-x analysis of a smooth initial profile

In this case

$$u = u_0(y,z) + xu_1(y,z) + ...$$

$$v = 0 + xv_1(y,z) + ...$$

$$w = 0 + xw_1(y,z) + ...$$

$$\zeta = 0 + x\zeta_1(y,z) + ...$$

Therefore 4.15 may be written as

$$u_0u_1 + \underbrace{xv_1\frac{\partial u_0}{\partial y} + xw_1\frac{\partial u_0}{\partial z}}_{=0 \text{ since } v,w << 1} = \frac{\partial^2 u_0}{\partial y^2} + \frac{\partial^2 u_0}{\partial z^2} \quad \text{to leading order.}$$

Hence $u_1 = \frac{\nabla^2 u_0}{u_0}$, where $\nabla^2 = (\frac{\partial^2}{\partial y^2} + \frac{\partial^2}{\partial z^2})$.

Considering a relatively smooth initial profile such as $u_0 = \frac{1}{(1+y^2+z^2)}$,

$\frac{\partial^2 u_0}{\partial y^2} = \frac{2}{(1+y^2+z^2)^3}\{3y^2 - z^2 - 1\}$.

Likewise, $\frac{\partial^2 u_0}{\partial z^2} = \frac{2}{(1+y^2+z^2)^3}\{3z^2 - y^2 - 1\}$.

Hence $\nabla^2 u_0 = \frac{4}{(1+y^2+z^2)^3}\{y^2 + z^2 - 1\}$

and $u_1 = \frac{\nabla^2 u_0}{u_0} = \frac{4}{(1+y^2+z^2)^2}\{y^2 + z^2 - 1\}$.

Therefore $u = \frac{1}{(1+y^2+z^2)} + \frac{4x}{(1+y^2+z^2)^2}\{y^2+z^2-1\}$ for small positive x.

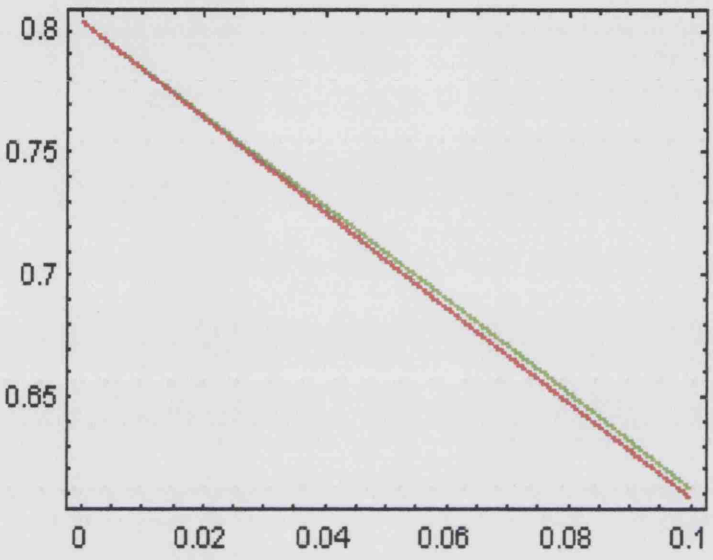

Figure 4.5: comparison of numerical solution with analytical solution at small x for relatively smooth initial profile

Figure 4.5 compares the analytical values of u (RED curve)with the numerical values (GREEN curve) obtained at a node off the centreline. It can be seen that, for relatively smooth initial profiles, the numerical solution shows very good agreement with the solution produced by small-x analysis. However, for less smooth 'unit-pulse' type initial profiles, small-x analysis is subject to the same limitations encountered in the two-dimensional case, highlighted in 2.3, and can provide no really useful comparison.

4.6 Obtaining the pressure equation

To obtain an equation for pressure we return to the governing equations of section 4.2 and differentiate the non-dimensionalised forms of equations 4.5 and 4.6 with respect to y and z, respectively, to obtain

$$u\frac{\partial^2 v}{\partial x \partial y}+\frac{\partial v}{\partial x}\frac{\partial u}{\partial y}+v\frac{\partial^2 v}{\partial y^2}+(\frac{\partial v}{\partial y})^2+w\frac{\partial^2 v}{\partial y \partial z}+\frac{\partial w}{\partial y}\frac{\partial v}{\partial z}=-\frac{\partial^2 p}{\partial y^2}+\{\frac{\partial^3 v}{\partial y^3}+\frac{\partial^3 v}{\partial y \partial z^2}\}$$

and

$$u\frac{\partial^2 w}{\partial x \partial z}+\frac{\partial w}{\partial x}\frac{\partial u}{\partial z}+v\frac{\partial^2 w}{\partial y \partial z}+\frac{\partial w}{\partial y}\frac{\partial v}{\partial z}+w\frac{\partial^2 w}{\partial z^2}+(\frac{\partial w}{\partial z})^2=-\frac{\partial^2 p}{\partial z^2}+\{\frac{\partial^3 v}{\partial y^3}+\frac{\partial^3 v}{\partial y \partial z^2}\}.$$

These can then be added together to produce:

$$u\frac{\partial}{\partial x}\{\frac{\partial v}{\partial y}+\frac{\partial w}{\partial z}\}+v\frac{\partial}{\partial y}\{\frac{\partial v}{\partial y}+\frac{\partial w}{\partial z}\}+w\frac{\partial}{\partial z}\{\frac{\partial v}{\partial y}+\frac{\partial w}{\partial z}\}+(\frac{\partial v}{\partial y})^2+(\frac{\partial w}{\partial z})^2+\frac{\partial v}{\partial x}\frac{\partial u}{\partial y}$$

$$+\frac{\partial w}{\partial x}\frac{\partial u}{\partial z}+2\frac{\partial w}{\partial y}\frac{\partial v}{\partial z}=-\nabla^2 p+\{\frac{\partial^2}{\partial y^2}(\frac{\partial v}{\partial y}+\frac{\partial w}{\partial z})+\frac{\partial^2}{\partial z^2}(\frac{\partial v}{\partial y}+\frac{\partial w}{\partial z})\},$$

which, after considering the continuity equation, implies

$$-u\frac{\partial^2 u}{\partial x^2}-v\frac{\partial^2 u}{\partial x \partial y}-w\frac{\partial^2 u}{\partial x \partial z}+(\frac{\partial u}{\partial x})^2-2\frac{\partial v}{\partial y}\frac{\partial w}{\partial z}+\frac{\partial v}{\partial x}\frac{\partial u}{\partial y}+\frac{\partial w}{\partial x}\frac{\partial u}{\partial z}+2\frac{\partial w}{\partial y}\frac{\partial v}{\partial z}$$

$$=-\nabla^2(p+\frac{\partial u}{\partial x}). \qquad (4.20)$$

Then, considering the u momentum equation 4.4, we have

$$\frac{\partial}{\partial x}\{u\frac{\partial u}{\partial x}+v\frac{\partial u}{\partial y}+w\frac{\partial u}{\partial z}\}=\frac{\partial}{\partial x}\{\nabla^2 u\},$$

which, after expanding the left-hand-side and rearranging, implies that

$$-u\frac{\partial^2 u}{\partial x^2}-v\frac{\partial^2 u}{\partial x\partial y}-w\frac{\partial^2 u}{\partial x\partial z}=-\frac{\partial}{\partial x}\nabla^2 u+(\frac{\partial u}{\partial x})^2+\frac{\partial v}{\partial x}\frac{\partial u}{\partial y}+\frac{\partial w}{\partial x}\frac{\partial u}{\partial z}. \quad (4.21)$$

Hence, substituting this into 4.20 and rearranging gives the following pressure equation:

$$\nabla^2 p=-2\{(\frac{\partial u}{\partial x})^2+\frac{\partial v}{\partial x}\frac{\partial u}{\partial y}+\frac{\partial w}{\partial x}\frac{\partial u}{\partial z}+\frac{\partial w}{\partial y}\frac{\partial v}{\partial z}-\frac{\partial v}{\partial y}\frac{\partial w}{\partial z}\}, \quad (4.22)$$

which can be approximated using finite-differencing and solved using the Gauss-Jacobi iterative technique described earlier.

The iterative scheme is

$$P_{i,j}^{k+1}=\frac{1}{2(\Delta y^2+\Delta z^2)}\{\Delta y^2(P_{i,j+1}^k+P_{i,j-1}^k)+\Delta z^2(P_{i+1,j}^k+P_{i-1,j}^k)+2\Delta y^2\Delta z^2 X\}$$

where $X=(\frac{U_{i,j}-\overline{U}_{i,j}}{\Delta x})^2+(\frac{U_{i+1,j}-U_{i-1,j}}{2\Delta y})(\frac{newV_{i,j}-\overline{V}_{i,j}}{\Delta x})+(\frac{U_{i,j+1}-U_{i,j-1}}{2\Delta z})(\frac{newW_{i,j}-\overline{W}_{i,j}}{\Delta x})$

$+(\frac{newW_{i+1,j}-newW_{i-1,j}}{2\Delta y})(\frac{newV_{i,j+1}-newV_{i,j-1}}{2\Delta z})$

$-(\frac{newV_{i+1,j}-newV_{i-1,j}}{2\Delta y})(\frac{newW_{i,j+1}-newW_{i,j-1}}{2\Delta z})$.

It was hoped that specification of u_0 only would be sufficient for the computational solution to evolve; this was confirmed, subject to a settling-in period, which appeared to span the first 25-30 x-steps.

With the x-step (Δx) set at 0.0001, the program was made to run forward through 200 steps. This equated to approximately 27mm (a fifth of the total range of interest to Sortex). However, it should be noted that of particular interest are the first 15mm or so, since data produced over this range can be compared directly with data obtained from Sortex's physical test rig.

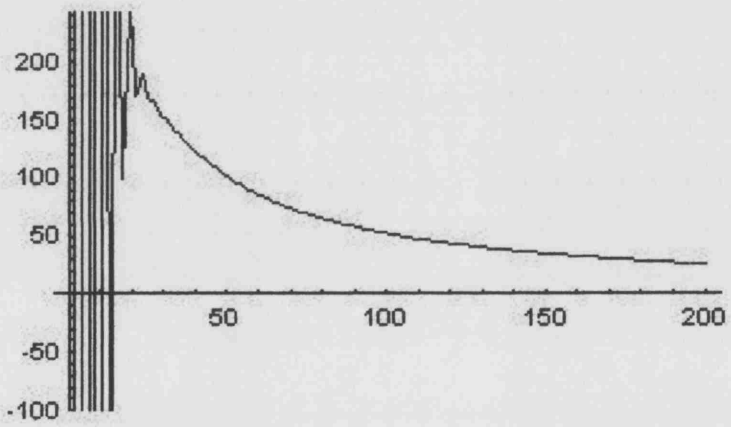

Figure 4.6: Non-dimensional centre-line pressure curve produced by the numerical solution with a smoothed unit-pulse initial profile.

Figure 4.6 clearly shows that the solution does not settle down until after the first thirty or so steps (i.e. beyond 4mm in Sortex terms). Since this accounts for over a quarter of the range in which physical data exists for comparison, consideration was given to the starting conditions on the lateral velocity components v and w and the starting pressure.

4.7 Small-distance analysis

Consider the following power series expansions:

$$u = u_0 + xu_1 + x^2u_2 + ...$$

$$v = v_0 + xv_1 + x^2v_2 + ...$$

$$w = w_0 + xw_1 + x^2w_2 + ...$$

$$\overline{p} = \overline{p}_0 + x\overline{p}_1 + x^2\overline{p}_2 + ...$$

The continuity equation may be rewritten as

$$(u_1 + 2xu_2) + (v_{0y} + xv_{1y}) + (w_{0z} + xw_{1z}) = 0.$$

Therefore, equating coefficients of x, $u_1 = -v_{0y} - w_{0z}$ and $u_2 = \frac{-v_{1y}-w_{1z}}{2}$.

The v-momentum equation gives

$$v_1 = \frac{\nabla^2 v_0 - v_0 v_{0y} - w_0 v_{0z} - \overline{p}_{0y}}{u_0}$$

and the w-momentum equation gives

$$w_1 = \frac{\nabla^2 w_0 - v_0 w_{0y} - w_0 w_{0z} - \overline{p}_{0z}}{u_0}.$$

Also

$$u_{1y} = -v_{0yy} - w_{0yz},$$

$$u_{1z} = -v_{0yz} - w_{0zz},$$

$$v_{1y} = \frac{1}{u_0}(\nabla^2 v_{0y} - v_0 v_{0yy} - v_{0y}^2 - w_0 v_{0yz} - w_{0y} v_{0z} - \overline{p}_{0yy})$$

$$-\frac{u_{0y}}{u_0^2}(\nabla^2 v_0 - v_0 v_{0y} - w_0 v_{0z} - \overline{p}_{0y}),$$

and

$$w_{1z} = \frac{1}{u_0}(\nabla^2 w_{0z} - v_0 w_{0yz} - v_{0z} w_{0y} - w_0 w_{0zz} - w_{0z}^2 - \overline{p}_{0zz})$$

$$-\frac{u_{0z}}{u_0^2}(\nabla^2 w_0 - v_0 w_{0y} - w_0 w_{0z} - \overline{p}_{0z}).$$

Furthermore the u-momentum equation can be written

$$(u_0 + xu_1)(u_1 + xu_2) + (v_0 + xv_1)(u_{0y} + xu_{1y}) + (w_0 + xw_1)(u_{0z} + xu_{1z})$$

$$= \nabla^2(u_0 + xu_1). \tag{4.23}$$

Equating coefficients of x in 4.23 we obtain

$$v_0 u_{0y} - u_0 v_{0y} - u_0 w_{0z} + w_0 u_{0z} = \nabla^2 u_0, \tag{4.24}$$

which can be rewritten as

$$(\frac{v_0}{u_0})_y + (\frac{w_0}{u_0})_z = -\frac{\nabla^2 u_0}{u_0^2}, \tag{4.25}$$

and

$$2u_0u_2 + u_1^2 + v_0u_{1y} + v_1u_{0y} + w_0u_{1z} + w_1u_{0z} = \nabla^2 u_1, \tag{4.26}$$

which, after making the relevant substitutions and cancelling, gives:

$$\nabla^2\overline{p}_0 = \frac{2u_{0y}}{u_0}(\overline{p}_{0y} + w_0v_{0z} + v_0v_{0y} - \nabla^2 v_0) +$$

$$\frac{2u_{0z}}{u_0}(\overline{p}_{0z} + w_0w_{0z} + v_0w_{0y} - \nabla^2 w_0) - 2(v_{0y} + w_{0z})^2 - 2v_{0z}w_{0y}. \tag{4.27}$$

Returning to equation 4.25, obtained from the leading order expansion of the u-momentum equation, we seek now to obtain expressions for v_0 and w_0, and thence ζ_0.

Suppose that v_{0cf} and w_{0cf} are complementary functions and V_0 and W_0 are particular integrals, which together give general solutions v_0 and w_0. Then, by considering the homogeneous problem $(\frac{v_0}{u_0})_y + (\frac{w_0}{u_0})_z = 0$, which is satisfied by the function $\lambda(y,z)$ such that $\lambda_z = \frac{v_0}{u_0}$ and $-\lambda_y = \frac{w_0}{u_0}$, we can specify an arbitrary function of y and z, such as $\lambda(y,z) = y^2 + z^2$, say, for which the corresponding complementary functions would be $v_{0cf} = 2zu_0$ and $w_{0cf} = -2yu_0$. Then, to obtain a particular integral, V_0, consider 4.25 such that $w_0 = 0$. So that $-(\frac{v_0}{u_0})_y = \frac{\nabla^2 u_0}{u_0^2}$, giving

$$V_0 = -u_0 \int^y \frac{\nabla^2 u_0}{u_0^2} dy. \tag{4.28}$$

This integral can be evaluated numerically, using Simpson's method, and the result used to obtain values for v_0 and w_0, which we will obtain by considering the cross-planar stream function. First, however, consideration must be given to the boundary conditions.

4.7.1 Boundary conditions

Our main interest here is in the far-field behaviour. Considering $(\frac{v_0}{u_0})_y = -\frac{\nabla^2 u_0}{u_0^2}$, from above, and the relatively smooth initial profile $u_0 = 1/(1+y^6+z^6)$, we see that at large y values $(\frac{v_0}{u_0})_y \approx \frac{y^{-8}}{y^{-12}} \sim y^4$. This implies $v_0 \approx u_0.y^5 \sim y^{-1}$. Therefore, in terms of the stream function, $\psi_y \approx \frac{w_0}{u_0} \sim y^5$, implying $\psi \sim y^6$ (or z^6 at large z). Hence we expect that $u_0\psi_y$ and $u_0\psi_z \to 0$ as $|y|$ and $|z| \to \infty$.

Also, by considering below the axisymmetric case it is possible to gain further insight into the nature of the far-field boundary conditions from the radial velocity components.

In cylindrical polar coordinates the continuity equation is

$$r\frac{\partial u}{\partial x} + \frac{\partial (rv)}{\partial r} = 0,$$

and the x-momentum boundary-layer equation is

$$u\frac{\partial u}{\partial x} + v\frac{\partial u}{\partial r} = \frac{\partial^2 u}{\partial r^2} + \frac{1}{r}\frac{\partial u}{\partial r}.$$

Therefore, expanding $u = u_0 + xu_1 + ...$ and $v = v_0 + ...$, the continuity equation becomes:

$$u_1 r + v_0 + r\frac{\partial v_0}{\partial r} = 0,$$

implying

$$u_1 = \frac{-v_0 - r\frac{\partial v_0}{\partial r}}{r}.$$

The momentum equation becomes

$$u_0 u_1 + v_0 \frac{\partial u_0}{\partial r} = \frac{\partial^2 u_0}{\partial r^2} + \frac{1}{r}\frac{\partial u_0}{\partial r},$$

which, upon substituting for u_1, gives

$$\frac{-u_0 v_0}{r} - u_0 \frac{\partial v_0}{\partial r} + v_0 \frac{\partial u_0}{\partial r} = \frac{\partial^2 u_0}{\partial r^2} + \frac{1}{r}\frac{\partial u_0}{\partial r}.$$

Hence the equation controlling v_0 is

$$r u_0'' + u_0' = -u_0 v_0 - r u_0 v_0' + r v_0 u_0', \tag{4.29}$$

where $'$, representing differentiation with respect to r, is used for ease of notation.

Dividing both sides of 4.29 by u_0^2 it follows that

$$-\frac{\partial}{\partial r}(\frac{rv_0}{u_0}) = \frac{(ru_0'' + u_0')}{u_0^2}.$$

Hence the solution is

$$v_0 = -\frac{u_0}{r}\int_0^r \frac{(ru_0'' + u_0')}{u_0^2}dr.$$

Therefore, for an initial profile that depends on r, such as $u_0 = \frac{a}{(1+r^n)}$, where $a = constant$ and $n > 0$, $v_0 \sim \frac{-n}{r}$ as $r \to \infty$, implying $v_0 \to 0$ slowly *as* $r \to \infty$. This is in agreement with what was expected at the start of the sub-section.

4.8 Cross-planar stream function formulation for three-dimensional jets

By definition, the vorticity $\zeta_0 = v_{0z} - w_{0y}$. Therefore letting $v_0 = V_0 + \overline{v}_0$ and $w_0 = W_0 + \overline{w}_0$ say, and considering zero vorticity with $W_0 = 0$ gives $V_{0z} + \overline{v}_{0z} = \overline{w}_{0y}$ and, hence,

$$\overline{v}_{0z} - \overline{w}_{0y} = -V_{0z}. \tag{4.30}$$

Then introducing the cross-plane stream function $\psi(y,z)$ such that $\psi_z = \frac{\overline{v}_0}{u_0}$

and $\psi_y = -\frac{w_0}{u_0}$ 4.30 can be written as

$$(u_0\psi_y)_y + (u_0\psi_z)_z = -V_{0z}. \tag{4.31}$$

This is an elliptic partial differential equation for ψ; we shall see later that it can be used to model interference properties of many jets in rectangular or other arrays. With u_0 known and V_0 supplied by 4.28, 4.31 can be solved numerically using a five point finite-difference scheme, as used throughout Chapter 2. The finite-difference scheme adopted here is thus given by

$$\psi_{i,j} = \frac{(\Delta y \Delta z)^2}{2u_{0i,j}(\Delta y^2 + \Delta z^2)}\{\frac{u_{0i,j}}{\Delta y^2}(\psi_{i+1,j}+\psi_{i-1,j})+\frac{(u_{0i+1,j} - u_{0i-1,j})}{4\Delta y^2}(\psi_{i+1,j}-\psi_{i-1,j})+$$

$$\frac{u_{0ij}}{\Delta z^2}(\psi_{i,j+1}+\psi_{i,j-1})+\frac{(u_{0i,j+1} - u_{i,j-1})}{4\Delta z^2}(\psi_{i,j+1}-\psi_{i,j-1})+\frac{1}{2\Delta z}(V_{0i,j+1}-V_{0ij-1})\}. \tag{4.32}$$

Also, since $v_0 = u_0\psi_z + V_0$ and $w_0 = -u_0\psi_y + 0$ (because in the present context $W_0 = 0$ from above), and using $\psi_y = \frac{(\psi_{i+1,j}-\psi_{i-1,j})}{2\Delta y}$ and $\psi_z = \frac{(\psi_{i,j+1}-\psi_{i,j-1})}{2\Delta z}$ as the representations of derivatives, values for the initial lateral velocity component contributions v_0 and w_0 can then be obtained.

Results for the $u_0 = 1/(1+y^6+z^6)$ initial profile discussed above are contained in the following tables and figures.

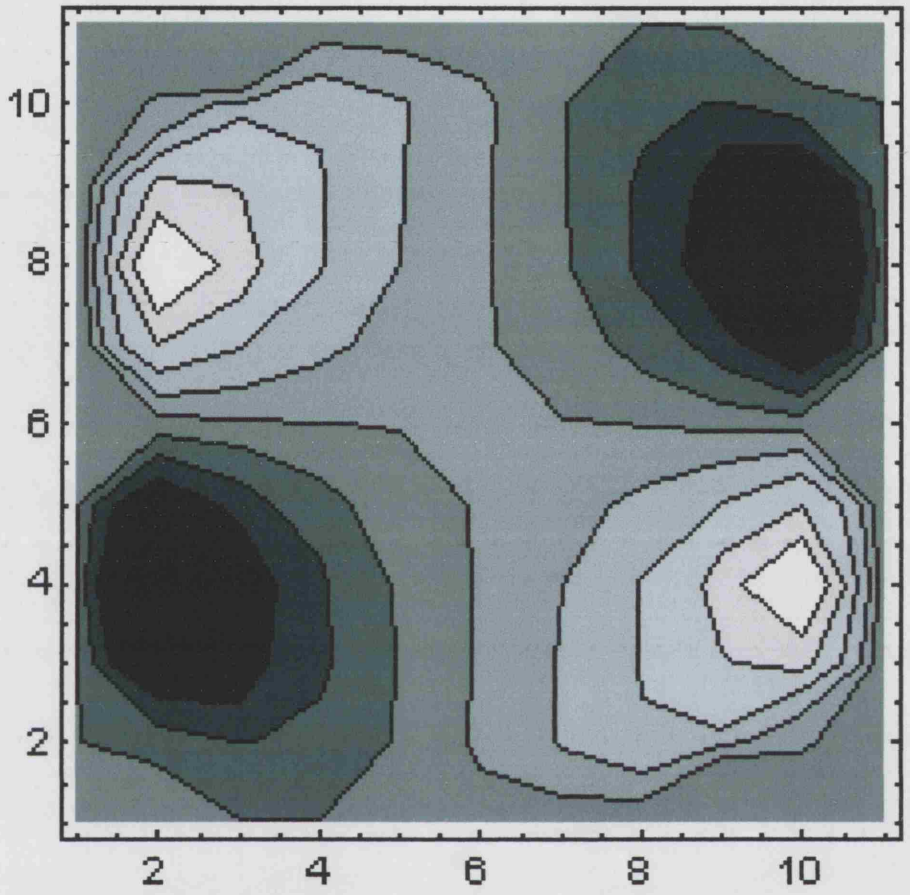

Figure 4.7: Contour plot of ψ in the y, z plane.

Output (ψ) for $u_0 = 1/(1+y^6+z^6)$, 81 interior point.

0	0	0	0	0	0	0	0	0	0	0
0	−2.1526	−4.1018	−2.8387	0.6863	4.6630	8.2211	10.4114	9.3597	4.8217	0
0	−13.3744	−9.6745	−4.7325	0.1936	4.3904	8.2390	12.1420	15.4231	16.8328	0
0	−19.0798	−11.5162	−4.7902	0.4222	4.3670	7.9697	12.2151	17.4989	23.0154	0
0	−11.6913	−6.1093	−1.5321	1.8812	4.3598	6.5003	8.9756	12.1873	15.8314	0
0	2.0956	3.0507	3.7250	4.1900	4.3582	4.1900	3.7250	3.0507	2.0956	0
0	15.8314	12.1873	8.9756	6.5003	4.3598	1.8812	−1.5321	−6.1093	−11.6913	0
0	23.0154	17.4989	12.2151	7.9697	4.3670	0.4222	−4.7902	−11.5162	−19.0798	0
0	16.8328	15.4231	12.1420	8.2390	4.3904	0.1936	−4.7325	−9.6745	−13.3744	0
0	4.8217	9.3597	10.4114	8.2211	4.6630	0.6863	−2.8387	−4.1018	−2.1526	0
0	0	0	0	0	0	0	0	0	0	0

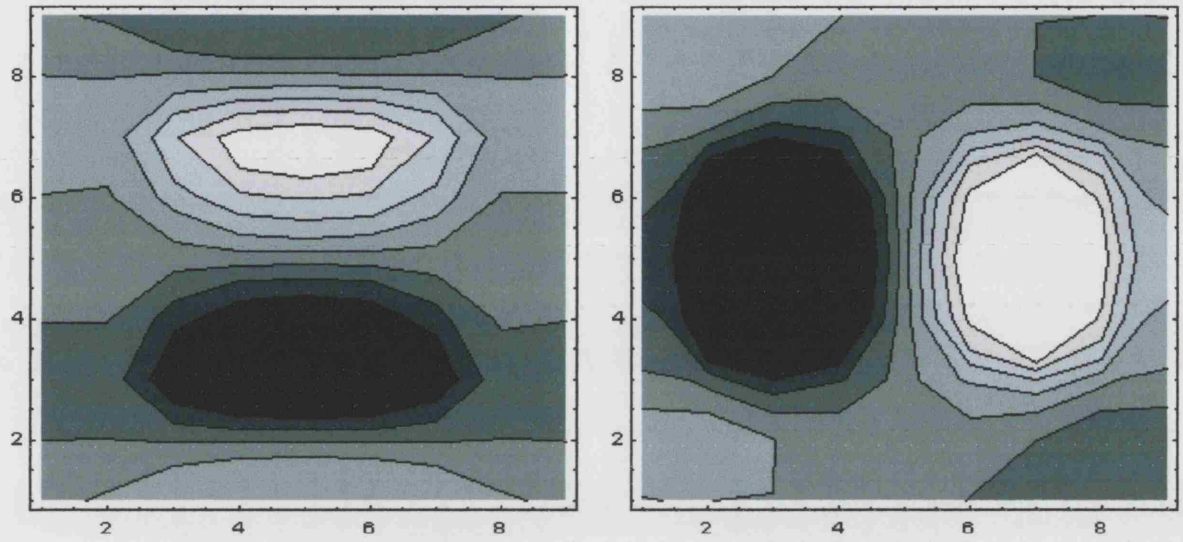

Figure 4.8: Contour plot of v_0 (on the left) and Contour plot of w_0 (on the right).

Output (v_0) for $u_0 = 1/(1+y^6+z^6)$, 81 interior point.

0	0	0	0	0	0	0	0	0	0	0
0	1.0535	1.9690	2.6348	2.8779	2.9211	2.8529	2.5768	1.9231	1.0566	0
0	−1.4253	−1.3348	−1.7257	−1.8619	−1.9768	−1.8709	−1.7273	−1.3246	−1.4457	0
0	−2.2240	−2.8053	−9.5551	−13.696	−14.629	−13.668	−9.3501	−2.6686	−2.2614	0
0	−1.2982	−1.2499	−5.6407	−9.0214	9.7977	−8.9457	−5.2902	−1.0528	−1.3419	0
0	0.0225	−0.1048	−0.1875	−0.0440	$1.09E-15$	0.0440	0.1875	0.1048	−0.0225	0
0	1.3419	1.0528	5.2902	8.9457	9.7977	9.0214	5.6407	1.2499	1.2982	0
0	2.2614	2.6686	9.3501	13.668	14.629	13.696	9.5551	2.8053	2.2240	0
0	1.4457	1.3246	1.7273	1.8709	1.9768	1.8619	1.7257	1.3348	1.4253	0
0	−1.0566	−1.9231	−2.5768	−2.8529	−2.9211	−2.8779	−2.6348	−1.9690	−1.0535	0
0	0	0	0	0	0	0	0	0	0	0

Output (w_0) for $u_0 = 1/(1+y^6+z^6)$, 81 interior point.

0	0	0	0	0	0	0	0	0	0	0
0	0.4149	0.5006	0.2821	−0.0117	−0.2656	−0.4984	−0.7239	−0.7982	−0.5221	0
0	0.8760	1.1567	0.5056	0.0729	0.0818	0.0695	−0.4673	−1.2698	−0.9415	0
0	−0.1003	−0.9237	−2.4448	−1.5810	0.0287	1.6288	2.4188	0.8384	0.0597	0
0	−1.2810	−4.0265	−7.9771	−4.5622	0.0106	4.5766	7.9535	3.9937	1.2655	0
0	−1.6653	−5.0628	−9.8791	−5.6191	0	5.6191	9.8791	5.0628	1.6653	0
0	−1.2655	−3.9937	−7.9535	−4.5766	−0.0106	4.5622	7.9771	4.0265	1.2810	0
0	−0.0597	−0.8384	−2.4188	−1.6288	−0.0287	1.5810	2.4448	0.9237	0.1003	0
0	0.9415	1.2698	0.4673	−0.0695	−0.0818	−0.0729	−0.5056	−1.1567	−0.8760	0
0	0.5221	0.7982	0.7239	0.4984	0.2656	0.0117	−0.282	−0.5006	−0.4149	0
0	0	0	0	0	0	0	0	0	0	0

By adding just a few lines of code to the computer program developed to solve the pressure equation in section 4.6 the values obtained above for v_0 and w_0 were introduced as starting conditions for the lateral velocity components. However, running the program with the modified starting conditions produced the same pressure solution, subject to the same settling-in period.

It seems clear then that this solution method can produce reasonable results throughout most of the flow-field, but will always be subject to the settling-in problem highlighted above during the very early development stage. However, running the program with smaller x-step sizes confirms that the settling-in phase can be confined to a region closer and closer to the nozzle exit. Therefore, by making the streamwise step smaller and smaller, detail can be captured closer and closer to the issuing nozzle. Hence, employing a suitably small x step and accounting for the Re^{-1} factor associated with p_1, plotting the dimensionalized centreline pressure data between 0.3mm and 15mm from the nozzle exit produces the following graph.

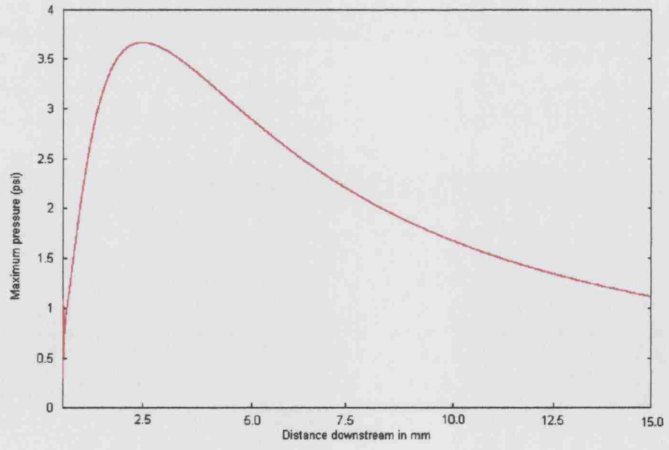

Figure 4.9: Dimensionalized centreline pressure up to 15mm from exit.

Furthermore, extracting centreline pressure values at $2.5mm$ intervals between $x = 2.5mm$ and $15mm$ enabled a comparison between maximum physical pressure data supplied by Sortex and the numerical solution to be made. Though subject to a scaling factor, figure 4.10 illustrates very good agreement between the physical and theoretical data.

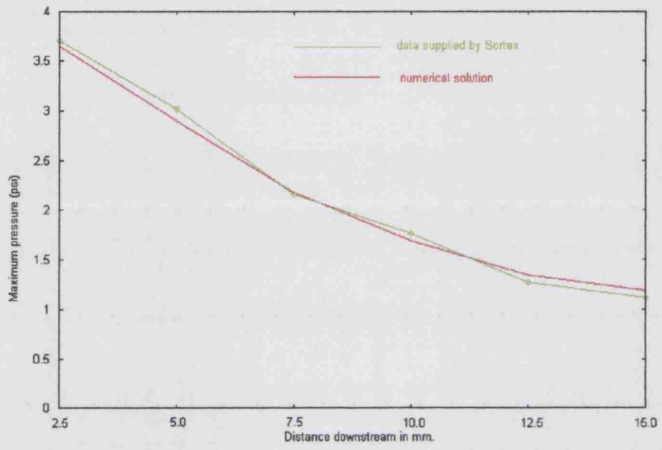

Figure 4.10: Dimensionalized pressure comparison at discrete points up to 15mm from exit.

4.9 Swirl

In [27] it is shown that the evolution of input swirl in ducts, such as those used to feed the jets in this study, is significantly affected by bending and twisting in the ducting coupled with other considerations, such as valves and internal surface roughness due to machining etc. See also [29]. Swirl is an important characteristic and therefore its effect on the issuing jets should be considered. We note that in a real setting, rather than in the case of the idealized unit-pulse type initial profiles considered here, that swirl will

contribute to a non-symmetric and rather complex or skewed u_0 initial jet profile. For the present study, however, we will demonstrate only the effects that an induced swirl has on the development of such idealized jets in terms of velocity and pressure characteristics.

Figures 4.11 and 4.12 are crude contour plots produced using 'Mathematica'. They illustrate, roughly, the v components of velocity a short way downstream with no induced swirl and with an induced swirl, respectively.

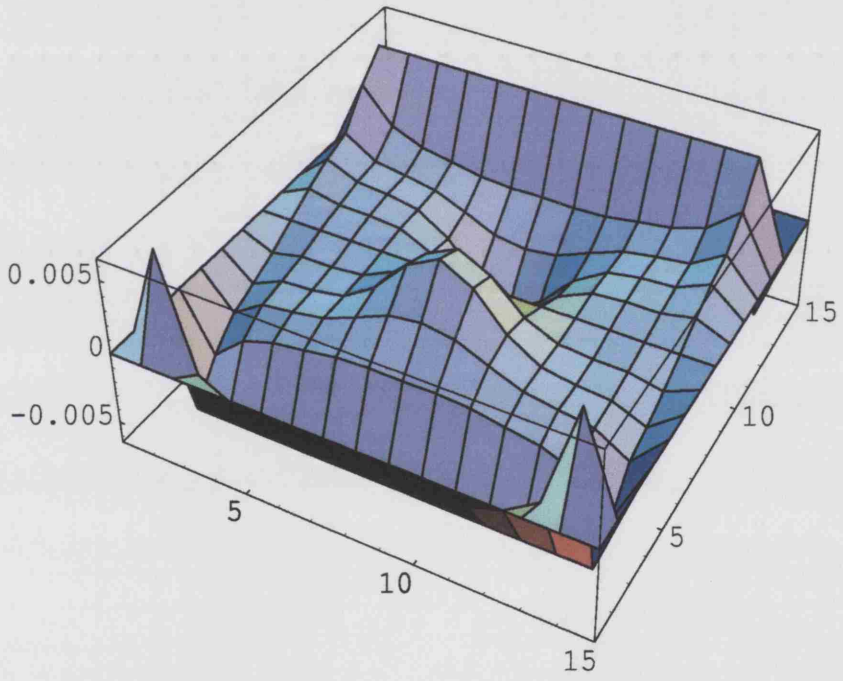

Figure 4.11: v velocity components ten steps downstream. (No induced swirl).

It is reasonable to assume that in the case of a unit-pulse initial profile the swirling effect will be concentrated around the core region and that it will rapidly diminish with distance away from the jet's central axis. Therefore, for

a jet issuing from a square nozzle, we contend that the initial lateral velocity components v_0 and w_0 could be given by expressions such as $v_0 = \frac{z}{r^n}$ and $w_0 = \frac{-y}{r^n}$, respectively, where r is the radial distance and n is a positive integer controlling the rate of decay, for an induced swirl in a clockwise direction.

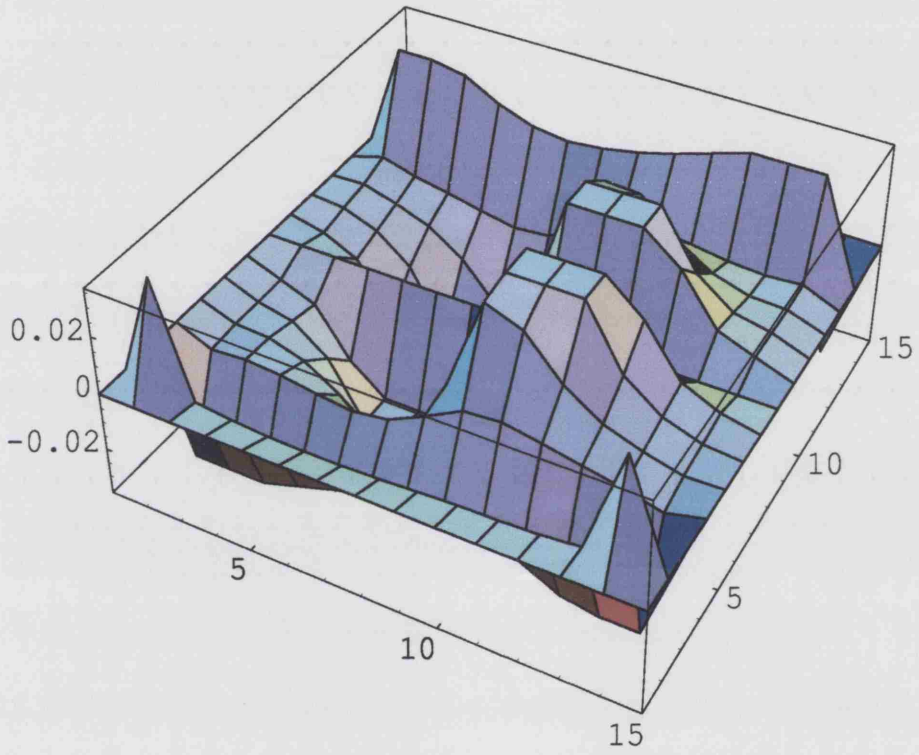

Figure 4.12: v velocity components ten steps downstream.(Swirl given by $v_0 = \frac{z}{r^5}$, $w_0 = \frac{-y}{r^5}$).

The numerical solution predicts no appreciable change in centreline streamwise velocity or pressure over the $150mm$ range of interest to Sortex when a range of swirl values is imposed. These results are illustrated in figures 4.13 and 4.14.

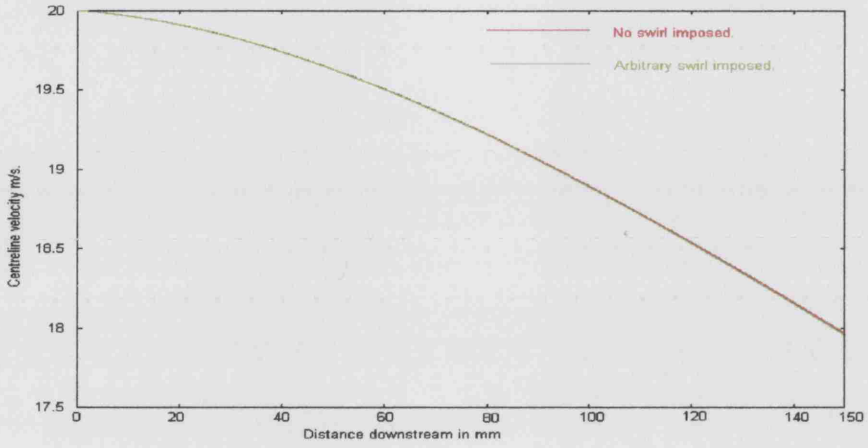

Figure 4.13: Comparison of centreline velocity with and without swirl.

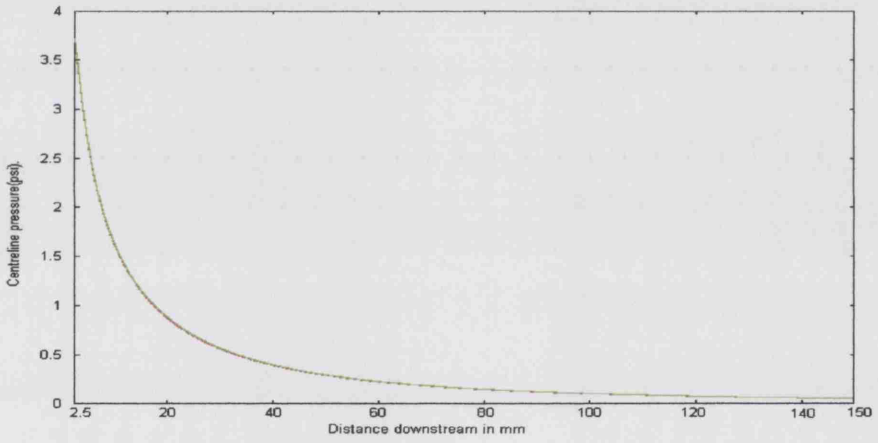

Figure 4.14: Comparison of centreline pressure with and without swirl.

However, it can be seen by comparing figures 4.15 and 4.16 that in the case of a unit-pulse initial profile imposed swirl works to contain and concentrate the pressure profile.

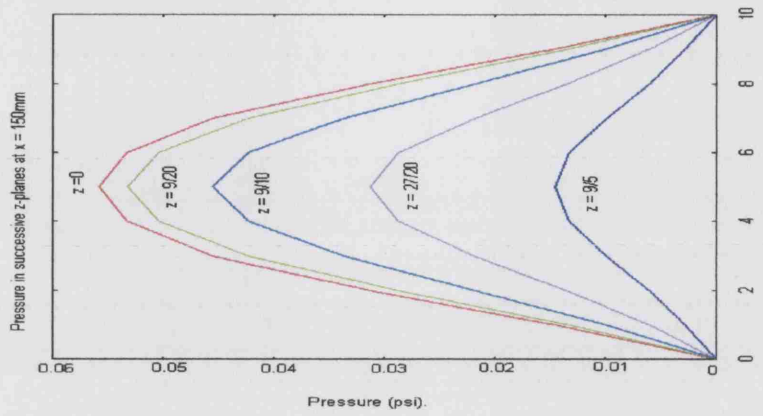

Figure 4.15: Pressure solutions for a square unit-pulse initial profile at $x = 150mm$.

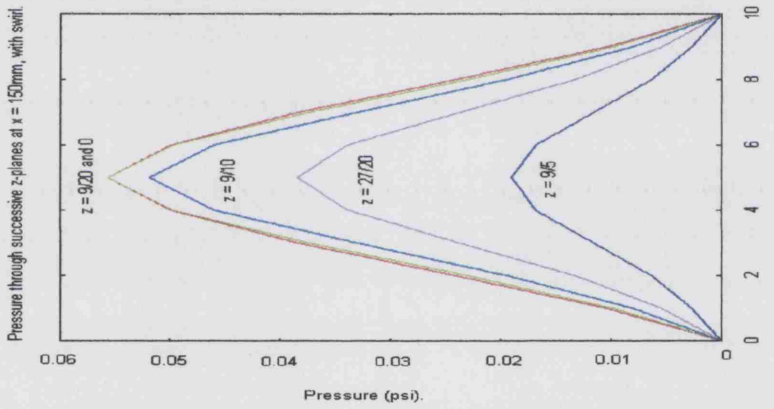

Figure 4.16: Pressure solutions for a square unit-pulse initial profile at $x = 150mm$, arbitrary swirl imposed.

4.10 Non-square rectangular jets

In order to deal with these cases the initial profile was modified so that $u_0 = 1/(1+(\frac{y}{a})^n+(\frac{z}{b})^n)$, where n is an even positive integer used to vary the initial profiles between relatively smooth at small n and near-discontinuous at large n, and a and b are integers greater than 1 used to control the width and depth of the jet's issuing nozzle. Consequently, to accommodate wider

nozzles required modifications to the size of the finite-difference grid and this in turn affected the y and z step sizes and the position of the far-field boundaries. Overall results from the modified scheme were good; however it was not possible to capture pressure data as close to the nozzle exit as in the case of square nozzles. Swirl was introduced in a similar manner to that outlined in the previous section but with $r = ((\frac{y}{a})^2 + (\frac{z}{b})^2)^{\frac{1}{2}}$. Figures 4.17 and 4.18 illustrate velocity and pressure results with and without swirl.

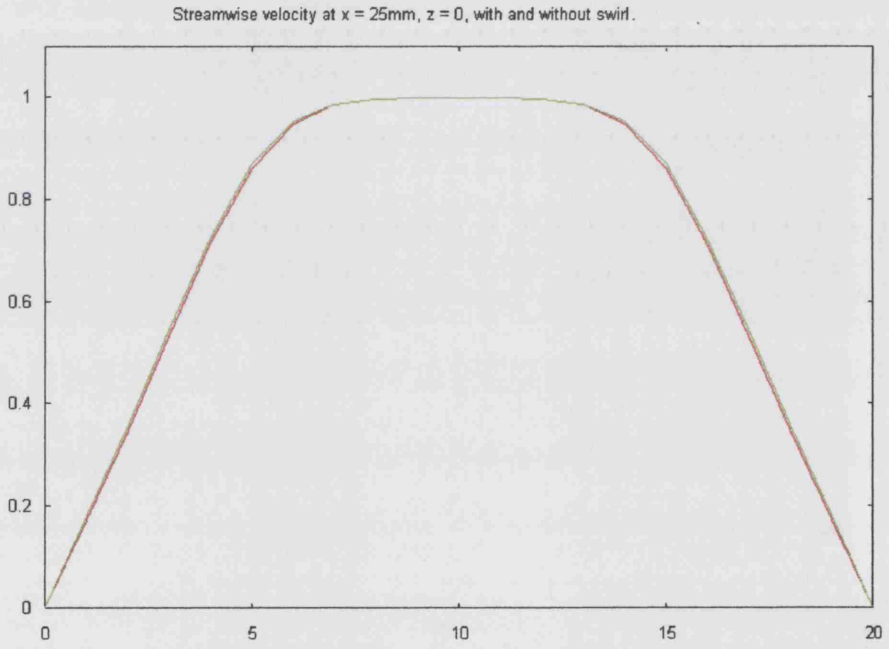

Figure 4.17: Streamwise velocity profiles with and without swirl at x = 25mm.

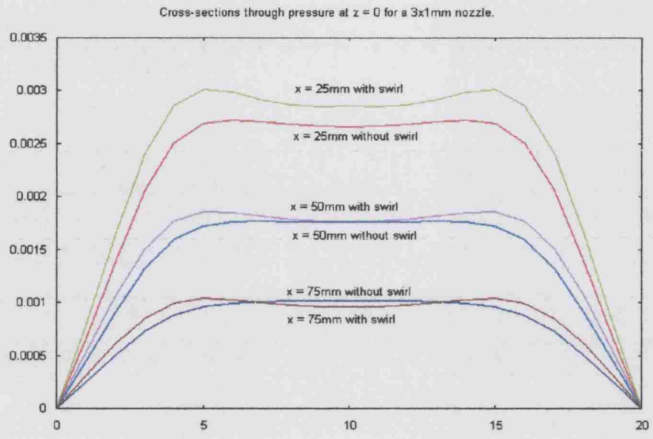

Figure 4.18: Pressure profiles with and without swirl.

4.11 Summary

In summary of Chapter 4, the governing equations of the steady three-dimensional jet have been derived in terms of a vorticity-velocity formulation and their numerical solution has been demonstrated using an iterative scheme. The results from the numerical solution and small-distance analysis of a smooth case were shown to agree closely. The pressure equation was obtained and solved numerically, but a weakness at the upstream end was highlighted. An attempt was made to overcome this weakness using small-distance analysis and a cross-planar stream function formulation to obtain starting values for the lateral velocity components and, although insightful, it proved not to be successful in terms of obtaining pressure results at very small x. It was demonstrated, however, that pressure data could be obtained relatively close to the nozzle exit simply by employing smaller streamwise steps in the numerical solution. Comparisons with physical pressure data supplied by Sortex showed good agreement, subject to a scaling factor required

possibly because the numerical solution was obtained from a square, rather than rectangular, initial profile. Finally, swirl was introduced to the starting conditions and its effect on the jet's development was recorded. There was no apparent loss of pressure or velocity over the entire range but the jet's pressure profile was concentrated along its axis.

Chapter 5

Three-Dimensional Unsteady Jets

5.1 Introduction

In this chapter we consider time-dependent solutions and then make direct comparisons with physical pressure data supplied by Sortex.

5.2 Governing equations

As in the last chapter, our starting point is the (unsteady) three-dimensional incompressible continuity equation:

$$\frac{\partial u}{\partial x} + \frac{\partial v}{\partial y} + \frac{\partial w}{\partial z} = 0 \tag{5.1}$$

and the Cartesian three-dimensional Navier-Stokes momentum equations 1.5, 1.6, 1.7, which after normalizing give:

$$\frac{\partial u}{\partial t} + u\frac{\partial u}{\partial x} + v\frac{\partial u}{\partial y} + w\frac{\partial u}{\partial z} = -\frac{\partial p}{\partial x} + \nabla^2 u, \tag{5.2}$$

$$\frac{\partial v}{\partial t} + u\frac{\partial v}{\partial x} + v\frac{\partial v}{\partial y} + w\frac{\partial v}{\partial z} = -\frac{\partial p}{\partial y} + \nabla^2 v, \tag{5.3}$$

$$\frac{\partial w}{\partial t} + u\frac{\partial w}{\partial x} + v\frac{\partial w}{\partial y} + w\frac{\partial w}{\partial z} = -\frac{\partial p}{\partial z} + \nabla^2 w, \tag{5.4}$$

where $\nabla^2 = (\frac{\partial^2}{\partial y^2} + \frac{\partial^2}{\partial z^2})$.

Once again, as in Section 4.2, $\frac{\partial v}{\partial y} = -(\frac{\partial u}{\partial x} + \frac{\partial w}{\partial z})$ and $\frac{\partial w}{\partial z} = -(\frac{\partial u}{\partial x} + \frac{\partial v}{\partial y})$ can be substituted into 5.3 and 5.4, respectively, and the vorticity term, $\zeta = \frac{\partial v}{\partial z} - \frac{\partial w}{\partial y}$ introduced so that

$$\frac{\partial v}{\partial t} + u\frac{\partial v}{\partial x} + v\frac{\partial v}{\partial y} + w\frac{\partial v}{\partial z} = -\frac{\partial p}{\partial y} + \frac{\partial \zeta}{\partial z} - \frac{\partial^2 u}{\partial x \partial y} \tag{5.5}$$

and

$$\frac{\partial w}{\partial t} + u\frac{\partial w}{\partial x} + v\frac{\partial w}{\partial y} + w\frac{\partial w}{\partial z} = -\frac{\partial p}{\partial z} - \frac{\partial \zeta}{\partial y} - \frac{\partial^2 u}{\partial x \partial z}. \tag{5.6}$$

Equations 5.5 and 5.6 can then be differentiated and combined to obtain the following vorticity evolution equation

$$\nabla^2 \zeta = \frac{\partial \zeta}{\partial t} + u\frac{\partial \zeta}{\partial x} + v\frac{\partial \zeta}{\partial y} + w\frac{\partial \zeta}{\partial z} + \zeta\frac{\partial v}{\partial y} + \zeta\frac{\partial w}{\partial z} + \frac{\partial v}{\partial x}\frac{\partial u}{\partial z} - \frac{\partial w}{\partial x}\frac{\partial u}{\partial y}. \tag{5.7}$$

Also, as in the steady case,

$$\nabla^2 v = \frac{\partial \zeta}{\partial z} - \frac{\partial^2 u}{\partial x \partial y} \tag{5.8}$$

and

$$\nabla^2 w = -\frac{\partial \zeta}{\partial y} - \frac{\partial^2 u}{\partial x \partial z} \tag{5.9}$$

and since $\frac{\partial p_0}{\partial x} = 0$ (see Section 4.2)

$$\nabla^2 u = \frac{\partial u}{\partial t} + u\frac{\partial u}{\partial x} + v\frac{\partial u}{\partial y} + w\frac{\partial u}{\partial z}. \tag{5.10}$$

Thus the three-dimensional unsteady jet problem is now in a form which can be solved numerically, subject to the following conditions:

$$u(0, y, z, 0) = u_0,$$

$$u(x, y, z, 0) = 0, \; x > 0,$$

$$u \to 0 \; as \; |y| \to \infty \; and \; u \to 0 \; as \; |z| \to \infty,$$

$$\frac{\partial u}{\partial y} = 0 \; at \; y = 0 \; and \; \frac{\partial u}{\partial z} = 0 \; at \; z = 0.$$

Our aim now, in essence, is to solve 5.10 for u, then 5.7 for ζ, followed by 5.8, 5.9 for v, w, along with some iteration, and so on.

5.3 Numerical solution

As in the previous chapter the u momentum equation, 5.10, can be solved using Gauss-Jordan elimination and the v, w and ζ equations solved iteratively. However, the inclusion of time-dependence requires the u momentum equation, and then the v, w and ζ equations, to be solved for every x station before proceeding to the next time value. The finite-difference equations are

$$(\frac{\overline{v}_{i,j}}{2\Delta y}-\frac{1}{(\Delta y)^2})u_{i+1,j}+(\frac{1}{\Delta t}+\frac{\overline{u}_{i,j}}{\Delta x}+\frac{2}{(\Delta y)^2}+\frac{2}{(\Delta z)^2})u_{i,j}-(\frac{\overline{v}_{i,j}}{2\Delta y}+\frac{1}{(\Delta y)^2})u_{i-1,j}+$$

$$(\frac{\overline{w}_{i,j}}{2\Delta z}-\frac{1}{(\Delta z)^2})u_{i,j+1}-(\frac{\overline{w}_{i,j}}{2\Delta z}+\frac{1}{(\Delta z)^2})u_{i,j-1}=\frac{u_{i,j}^{old}}{\Delta t}+\frac{(\overline{u}_{i,j})^2}{\Delta x}, \qquad (5.11)$$

$$v_{i,j}=\frac{(\Delta y\Delta z)^2}{2((\Delta y)^2+(\Delta z)^2)}\{(\frac{v_{i+1,j}+v_{i-1,j}}{(\Delta y)^2})+(\frac{v_{i,j+1}+v_{i,j-1}}{(\Delta z)^2})-$$

$$(\frac{\zeta_{i,j+1}-\zeta_{i,j-1}}{2\Delta z})+(\frac{u_{i+1,j}-u_{i-1,j}-\overline{u}_{i+1,j}+\overline{u}_{i-1,j}}{2\Delta x\Delta y})\}, \qquad (5.12)$$

$$w_{i,j}=\frac{(\Delta y\Delta z)^2}{2((\Delta y)^2+(\Delta z)^2)}\{(\frac{w_{i+1,j}+w_{i-1,j}}{(\Delta y)^2})+(\frac{w_{i,j+1}+w_{i,j-1}}{(\Delta z)^2})+$$

$$(\frac{\zeta_{i+1,j}-\zeta_{i-1,j}}{2\Delta y})+(\frac{u_{i,j+1}-u_{i,j-1}-\overline{u}_{i,j+1}+\overline{u}_{i,j-1}}{2\Delta x\Delta z})\}, \qquad (5.13)$$

$$(\frac{1}{\Delta t}+\frac{\overline{u}_{i,j}}{\Delta x}+\frac{2}{(\Delta y)^2}+\frac{2}{(\Delta z)^2})\zeta_{i,j}=(\frac{1}{(\Delta y)^2}-\frac{\overline{v_{i,j}}}{2\Delta y})\zeta_{i+1,j}+$$

$$(\frac{1}{(\Delta y)^2}+\frac{\overline{v}_{i,j}}{2\Delta y})\zeta_{i-1,j}+(\frac{1}{(\Delta z)^2}-\frac{\overline{w}_{i,j}}{2\Delta z})\zeta_{i,j+1}+(\frac{1}{(\Delta z)^2}+\frac{\overline{w}_{i,j}}{2\Delta z})\zeta_{i,j-1}+$$

$$\frac{\zeta_{i,j}^{old}}{\Delta t}+(\frac{\overline{u}_{i,j}}{\Delta x}-\frac{v_{i+1,j}}{2\Delta y}+\frac{v_{i-1,j}}{2\Delta y}-\frac{w_{i,j+1}}{2\Delta z}+\frac{w_{i,j-1}}{2\Delta z})\overline{\zeta}_{i,j}+$$

$$\frac{(\overline{v}_{i,j}-v_{i,j})(u_{i,j+1}-u_{i,j-1})}{2\Delta x\Delta z}+\frac{(\overline{w}_{i,j}-w_{i,j})(u_{i+1,j}-u_{i-1,j})}{2\Delta x\Delta y}. \qquad (5.14)$$

where u, v, w and ζ are values at the present time and x-station, u^{old} and ζ^{old} are values at the previous time but present x-station, $\overline{u}$, $\overline{v}$, $\overline{w}$ and $\overline{\zeta}$ are values at the previous x-station but present time and the i, j subscripts indicate positions in the y, z plane, respectively.

5.4 The pressure equation

To obtain an equation for pressure we follow the same procedure as in Section 4.6 and differentiate the governing v and w momentum equations 5.3, 5.4 with respect to y and z, respectively. The resulting equations are then added and after consideration of the continuity equation give

$$-\nabla^2(p+\frac{\partial u}{\partial x})=$$

$$-\frac{\partial^2 u}{\partial x\partial t}-u\frac{\partial^2 u}{\partial x^2}-v\frac{\partial^2 u}{\partial x\partial y}-w\frac{\partial^2 u}{\partial x\partial z}+\frac{\partial v}{\partial x}\frac{\partial u}{\partial y}+\frac{\partial w}{\partial x}\frac{\partial u}{\partial z}+2\frac{\partial w}{\partial y}\frac{\partial v}{\partial z}-2\frac{\partial v}{\partial y}\frac{\partial w}{\partial z}+(\frac{\partial u}{\partial x})^2. \qquad (5.15)$$

Differentiating the u momentum equation 5.2 with respect to x gives

$$-\frac{\partial}{\partial x}\nabla^2 u = -\frac{\partial^2 u}{\partial x \partial t} - u\frac{\partial^2 u}{\partial x^2} - v\frac{\partial^2 u}{\partial x \partial y} - w\frac{\partial^2 u}{\partial x \partial z} - \frac{\partial v}{\partial x}\frac{\partial u}{\partial y} - \frac{\partial w}{\partial x}\frac{\partial u}{\partial z} - (\frac{\partial u}{\partial x})^2, \tag{5.16}$$

which is substituted into 5.15 to obtain

$$\nabla^2 p = -2\{(\frac{\partial u}{\partial x})^2 + \frac{\partial v}{\partial x}\frac{\partial u}{\partial y} + \frac{\partial w}{\partial x}\frac{\partial u}{\partial z} + \frac{\partial w}{\partial y}\frac{\partial v}{\partial z} - \frac{\partial v}{\partial y}\frac{\partial w}{\partial z}\}. \tag{5.17}$$

Hence, the pressure equation for the three-dimensional unsteady jet is precisely the same as that obtained for the steady three-dimensional jet. We can therefore use the iterative finite-difference scheme of Section 4.6 for this case also.

5.5 Physical pressure data

In Section 4.1 we noted that the physical pressure data used for comparisons in this study are subject to fluctuations, which should be taken into account. We consider here three of the data-sets used, so that similarities and differences can be noted.

Figure 5.1 illustrates the maximum pressure values recorded at 3 milliseconds, 4 milliseconds, 5 milliseconds and 6 milliseconds after the ejector valve opens at points separated by 2.5mm intervals travelling downstream, in three different trials. The plots at 3 milliseconds show good agreement. However, all the other plots show appreciable differences in the pressure recordings at different distances along the flow. These differences could be the result of the

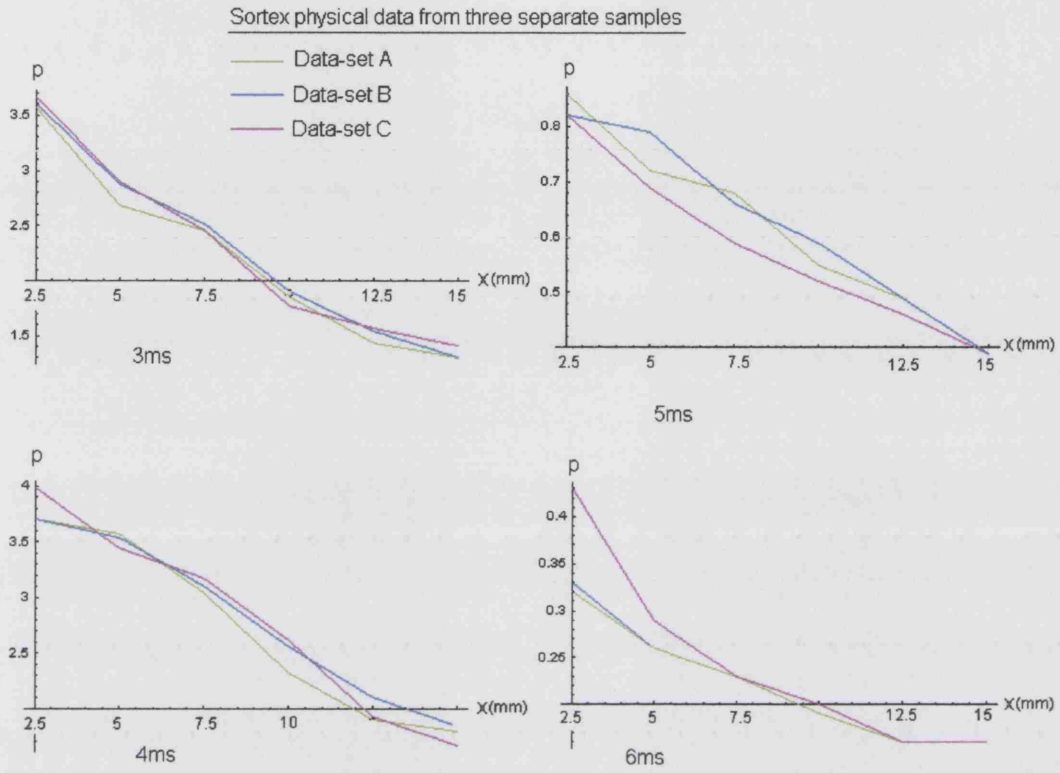

Figure 5.1: Maximum pressure values recorded at 2.5mm intervals along the flow for three distinct samples, at four different times.

complex upstream flow characteristics reported by Smith in [20] and Wilson in [22]. Alternatively, they could possibly be due to the apparatus used to obtain the data or the way this apparatus was set up. For instance, the distance between the points at which measurements were taken in each plane was crudely set at 1mm. Decreasing this gap size might aid consistency. It should be noted also that the maximum pressure values were generally found not to lie on the central streamwise axis but were consistently located in a particular region off-centre, as can be seen in figure 5.2. This observation also supports Smith's results in [20] regarding misalignment of the emerging jets.

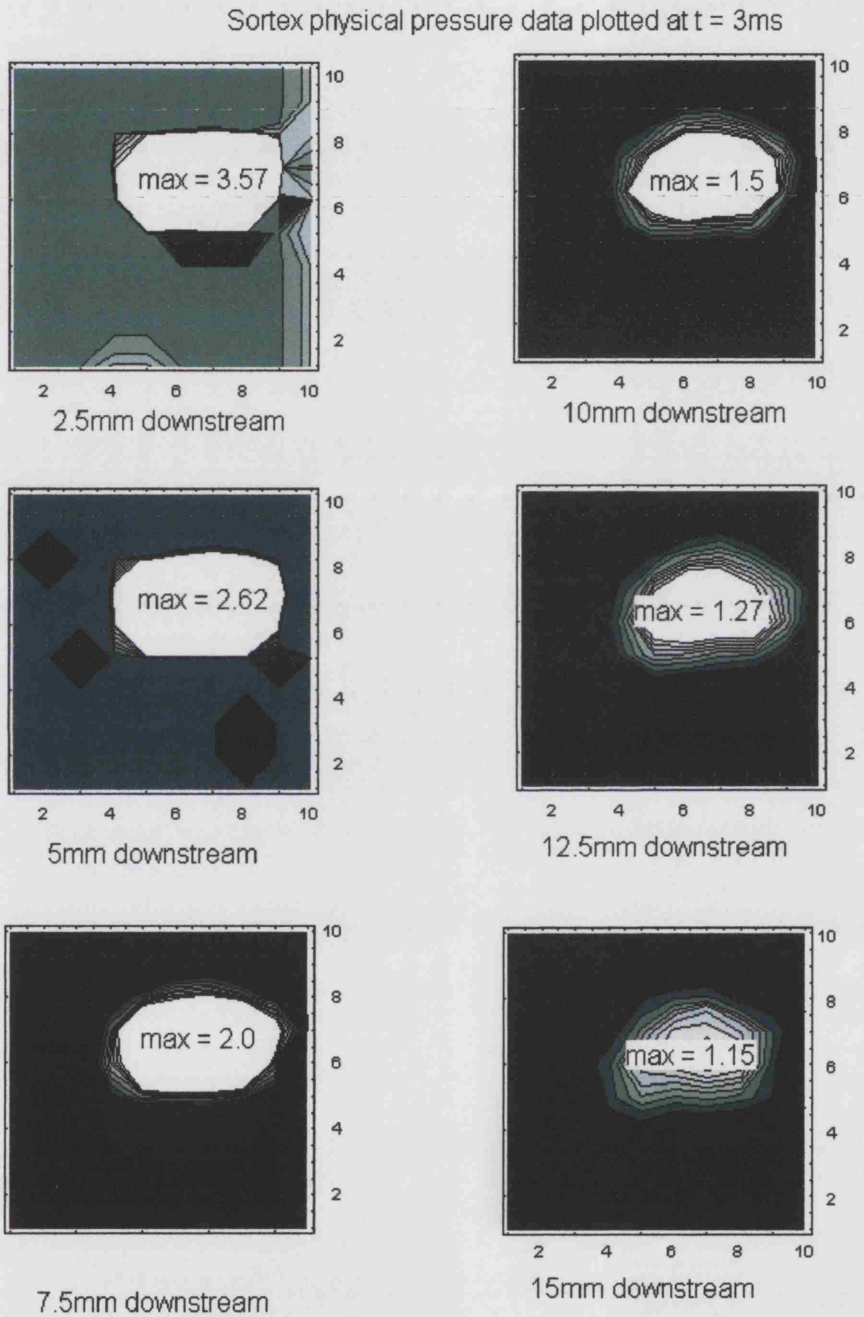

Figure 5.2: Contour plots of pressure data recorded at 3 milliseconds on 10mm x 10mm (y,z) planes. Highest values are white, lowest values are black.

5.6 Comparing numerical solutions with physical test data

The numerical scheme used to solve the unsteady case presently incorporates a symmetric growth and decay of the initial jet profile over time. For true comparisons to be made this should be replaced with data obtained from physical trials. However, for the present study, a simplified initial condition proves sufficient for some basic comparisons to be made. We note also that, due to the numerical solution's sensitivity to parameter changes, which require further investigation, the initial profile used is square rather than rectangular.

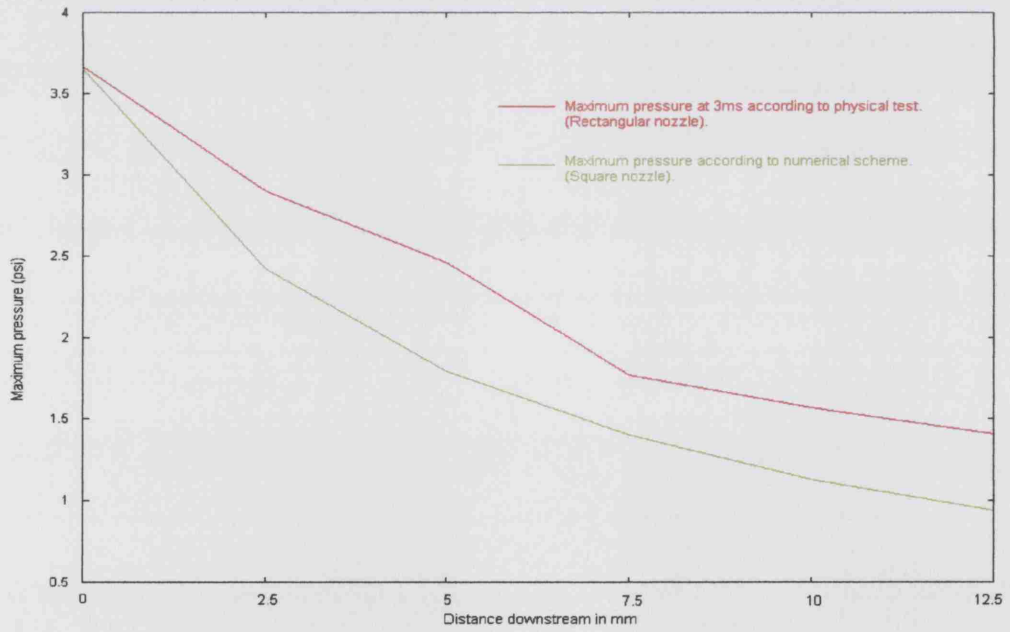

Figure 5.3: Maximum pressure values at t = 3ms, recorded at 2.5mm intervals along the flow .

Figure 5.3 illustrates the maximum pressures recorded during the physical trials of a jet issuing from a 3x1mm rectangular nozzle at t = 3ms (since these results were most consistent) and the results produced by the numerical solution for a jet issuing from a square nozzle. Similarities are apparent in the overall trend although the numerical solution describes a much smoother result.

5.7 Summary

In summary of Chapter 5, the governing equations of the unsteady three-dimensional jet have been derived and solved in a manner analogous to that of the preceding chapter. Pressure solutions have been obtained for a jet issuing from a square nozzle. These have been compared with physical results for a jet issuing from a rectangular nozzle and have been shown to agree relatively closely, subject to a scaling factor. The numerical solution has been found to be sensitive to parameter changes when considering the truly rectangular case however, and further investigation regarding this is required.

Chapter 6

Modelling Interference for Multiple Three-Dimensional Jets (Steady or Unsteady)

6.1 Introduction

In section 4.5 small-distance analysis was used to validate the numerical scheme used to solve the three-dimensional steady case. Here we take the same expansions for u, v, w and ζ and substitute them into equations 4.12, 4.13, 4.14 and 4.15. Then, considering the irrotational case $\zeta \equiv 0$, so that continuity then gives

$$\nabla^2 v = -\frac{\partial^2 u}{\partial x \partial y} \tag{6.1}$$

and

$$\nabla^2 w = -\frac{\partial^2 u}{\partial x \partial z}, \tag{6.2}$$

we can investigate further what happens to the lateral velocity components as the initial u_0 profile becomes less smooth and, hence, gain a greater understanding of the interference associated with jets in close proximity to each other. For this investigation we let $u_0 = 1/(1 + y^n + z^n) + c$, where n is a positive even integer and c is a positive real number. Results for a variety of initial profiles, ranging from very smooth through to near-discontinuous, are plotted in figure 6.1.

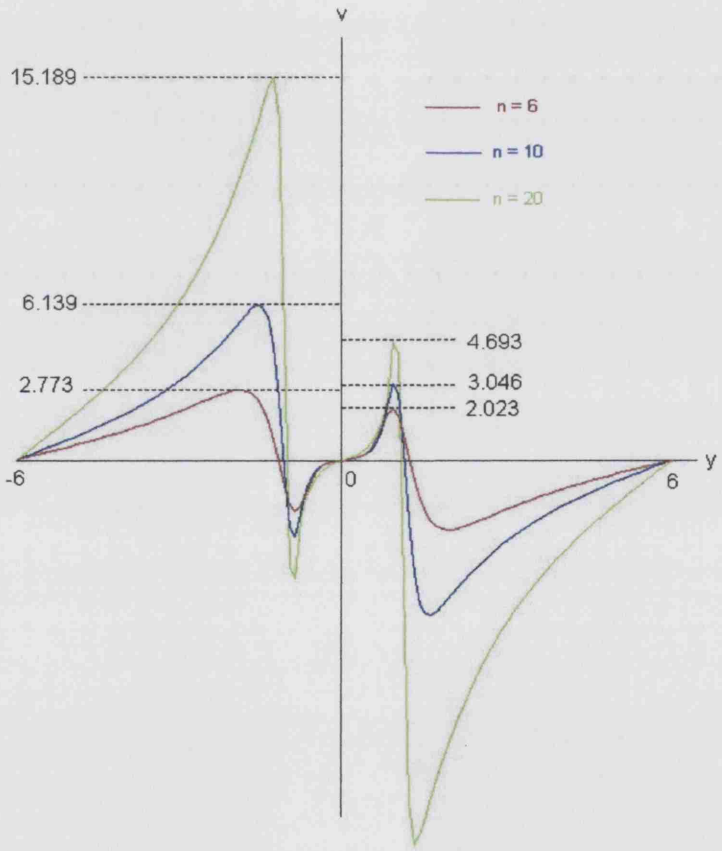

Figure 6.1: Effect on crossflow as u_0 approaches discontinuous case.

It is evident from figure 6.1 that the crossflow becomes ever stronger as the

edge layer thins and the incident flow approaches the discontinuous case. This is entirely consistent with the earlier two-dimensional study at small x, which predicts that a pure 'top-hat' profile generates normal velocities v of order $x^{\frac{-1}{2}}$ that are much larger than the order one normal velocities in the smooth case. Therefore the smooth lateral velocity components, v, have to grow as the non-smooth top-hat case is approached.

6.2 Potential flow solution of the steady rectangular discontinuous case

Following discussions with Professors F. T. Smith, S. N. Timoshin and S. N. Brown it became apparent that the problem with the lateral velocity components could be treated using potential flow theory. This is because as the top-hat situation is approached the streamwise velocity component u is constant mostly, both within the boundary, C say, of the top-hat and outside of it. Therefore from 6.1, 6.2 we have

$$\nabla^2 v = \nabla^2 w = 0$$

there; hence we can employ the potential function ϕ and stream function ψ, satisfying

$$\nabla^2 \phi = \nabla^2 \psi = 0.$$

The problem therefore reduces to solving Laplace's equation subject to a jump condition which must be satisfied on the jet's core-edge (the boundary

C) given by

$$\phi_n^+ - \phi_n^- = u_0 \int_{-\infty}^{\infty} \frac{u_0''}{u_0^2} dn, \tag{6.3}$$

where the primes represent differentiation with respect to n and which is obtained from the earlier small-distance analysis (see in chapter 2), and which drives the whole solution.

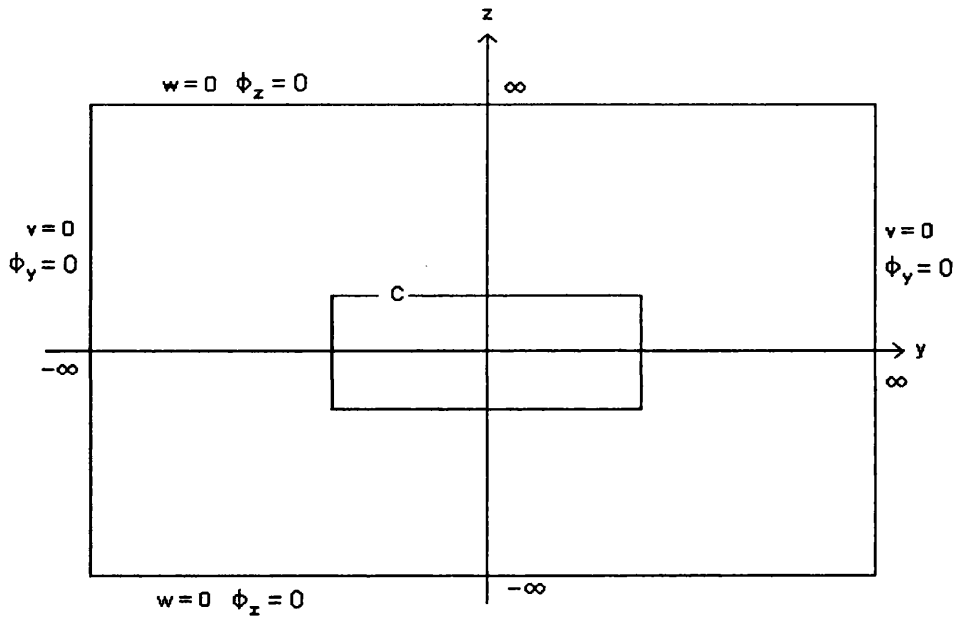

Figure 6.2: Potential flow problem specification, shown for a rectangular nozzle. C is the core-edge, on which the jump condition must be satisfied.

Initially in solving the present system it was assumed that the velocity components v and w should be set as zero at large distances from the origin, implying that $\frac{\partial \phi}{\partial y}$ and $\frac{\partial \phi}{\partial z}$ should be set as zero on the far-field y and z boundaries, respectively. However, solving Laplace's equation numerically subject to the above conditions produced the plots in figure 6.3, suggesting that the

far-field boundary conditions needed further investigation. Therefore the axisymmetric case was analysed since at sufficiently large distances from the centre the rectangular jet tends towards this.

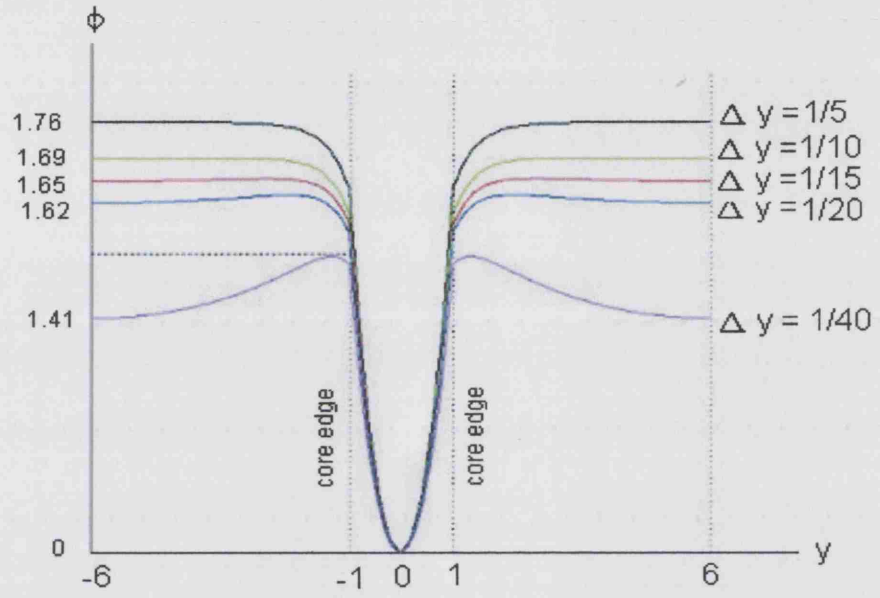

Figure 6.3: ϕ vs y ($z = 0$) at various Δy, ∞ fixed at ± 6.

6.3 The axisymmetric case and far-field conditions

In the axisymmetric case the continuity equation is given by

$$ru_x + (rv)_r = 0 \tag{6.4}$$

and the u-momentum equation is given by

$$uu_x + vu_r = u_{rr} + \frac{1}{r}u_r. \tag{6.5}$$

Hence, expanding $u = u_0(r) + xu_1(r) + ...$ and $v = v_0(r) + xv_1(r) + ...$ gives

$$u_1 + \frac{1}{r}(rv_0)_r = 0 \tag{6.6}$$

and

$$u_0u_1 + v_0u_0' = u_0'' + \frac{1}{r}u_0'. \tag{6.7}$$

From this we obtain

$$v_0 = -\frac{u_0}{r}\int_r^0 \frac{(u_0'' + r^{-1}u_0')}{u_0^2} r dr. \tag{6.8}$$

Considering a specific initial profile u_0 that depends on r, such as

$$u_0 = \frac{a}{1 + r^n},$$

where a is a constant and n is greater than zero, suggests $v_0 \sim -\frac{n}{r}$. Hence ϕ grows logarithmically as $r \to \infty$. A suitably revised boundary condition on ϕ can be implemented by considering the points on the far-field boundaries and their immediate neighbours, and doing so leads to the following expression

$$\phi_1 = \frac{\ln(r_3/r_1)}{\ln(r_3/r_2)}\phi_2 - \frac{\ln(r_2/r_1)}{\ln(r_3/r_2)}\phi_3, \tag{6.9}$$

where ϕ_1 represents the point on the outer boundary and ϕ_2, ϕ_3 are the successive points just inside the boundary.

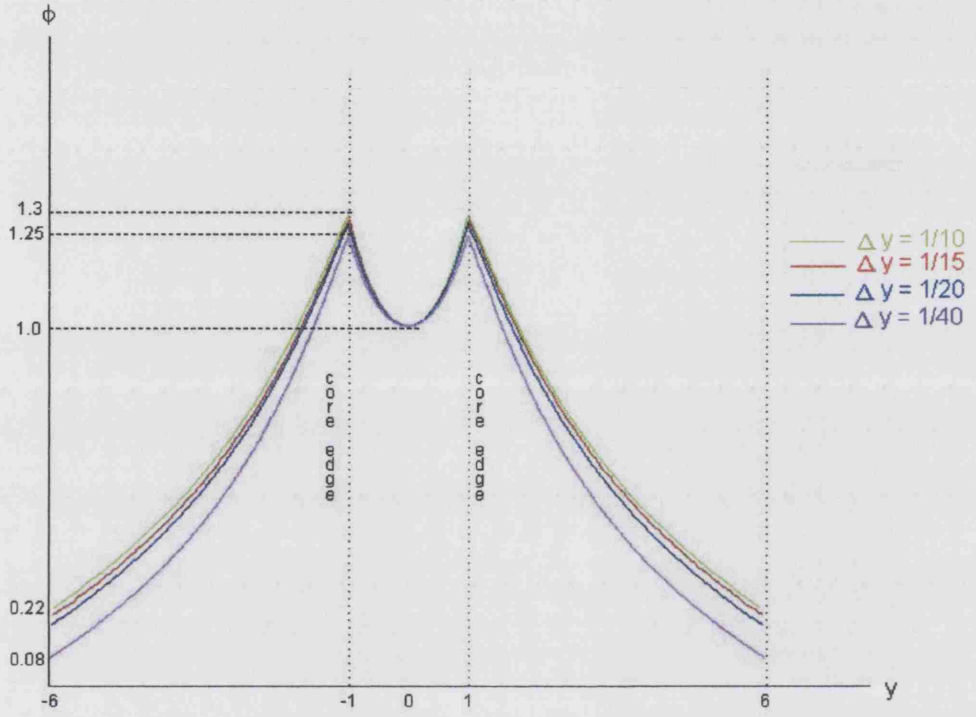

Figure 6.4: $\phi \, vs \, y(z = 0)$ for various Δy, ∞ fixed at ± 6, far-field conditions given by $\phi = -n \ln r + k$.

With the far-field boundary condition replaced by 6.9 the results for ϕ are now as in figure 6.4. It is evident, and significant, that the gradients of the curves plotted in 6.4 vary very little as the finite-difference grid used is refined, a property which is found to yield consistency in the results for the velocity component v.

6.3.1 Comparison of cross-flow prediction with numerical solution of smooth profiles

Returning to equations 6.6 and 6.7 for the axisymmetric case and considering the 'top-hat' scenario ($n >> 1$) implies that $u_0 = K$ say, within the core and it follows that $v_0 = 0$ there. Therefore, on the core-boundary, let $r = 1 + \epsilon\hat{r}$, where $\epsilon << 1$, and $u_0 = \overline{u}(\hat{r})$. From this it follows that

$$-(\frac{v_0}{\overline{u}})'\epsilon^{-1}\overline{u}^2 = \epsilon^{-2}\overline{u}'',$$

which can be rearranged to give

$$v_0 = -\frac{\overline{u}}{\epsilon}\int_{-\infty}^{\hat{r}} \frac{\overline{u}''}{\overline{u}^2}dr. \tag{6.10}$$

The appearance of the ϵ^{-1} factor in 6.10 is clearly a contributory factor to the growth in the crossflow solutions of the smooth case, and this is exaggerated by a factor of n present in the integral 6.10, as illustrated in figure 6.1. Since this analysis is local to the boundary, C, this work is no longer confined to the axisymmetric case and applies equally to any shape of nozzle cross-section, including the rectangular ones of most significance in this study. Therefore, in order to compare results from the smooth case with those produced by the potential flow theory it is appropriate to normalize the smooth-profile results, dividing them by a factor of n. The normalized results for a selection of n values are shown in figure 6.5, in which it can be seen that results seem to clearly converge to a limiting value and can now be compared directly with

the crossflow prediction produced by the potential flow solution as follows.

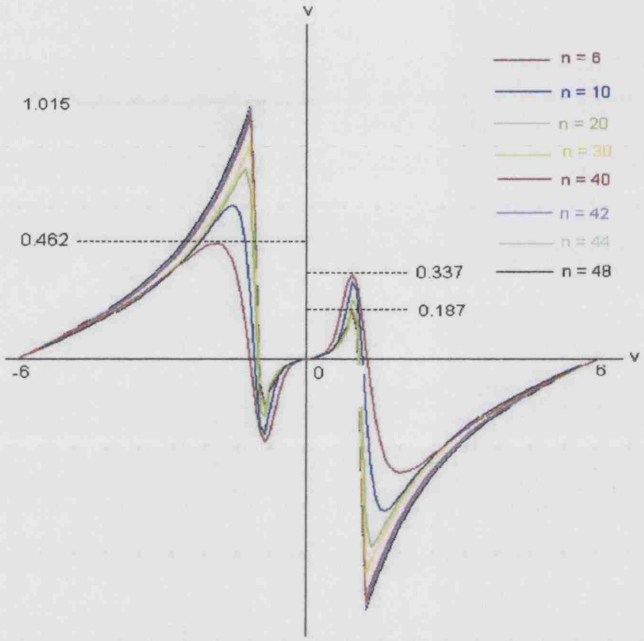

Figure 6.5: Normalised crossflow results for smooth cases.

Figure 6.6 shows fairly conclusively that for large n the smooth result tends towards the discontinuous result obtained by the potential flow theory. We contend, therefore, that the potential flow solution to the jet problem is reliable, but also note that the inherent jump discontinuity makes it especially useful for the study of several or many neighbouring jets in relatively close proximity. This is because, unlike most other potential flow solutions, when considering more than one jet the jump condition on the core-edge makes it possible to add on **linearly** to the solution for a single jet. In the sections that follow we will use this unusual feature to demonstrate steady and unsteady results for multiple rectangular and round jets.

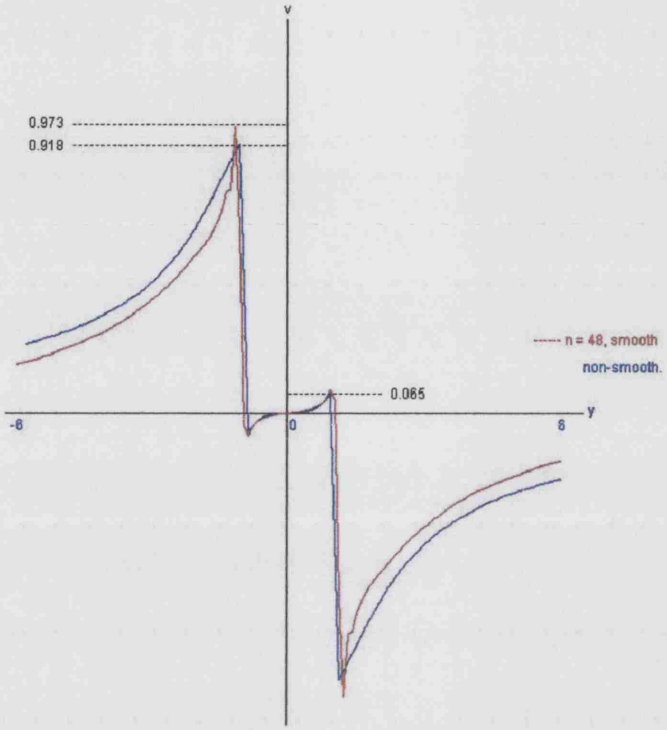

Figure 6.6: Comparison of crossflow prediction from smooth result at large n with potential flow solution.

6.4 Multiple in-line steady rectangular jets

As it stands, the numerical solution developed for the preceding section can only really be used to investigate the cross-flow characteristics of single steady rectangular jets of varying cross-section. This is because the solution domain must be fixed prior to any calculation. However, each individual jet in any array of jets under consideration will have a different solution domain, which must overlap those of all the others in the array. In this section we will discuss modifications to the numerical solution that enable the study of interference between several or many similar neighbouring jets.

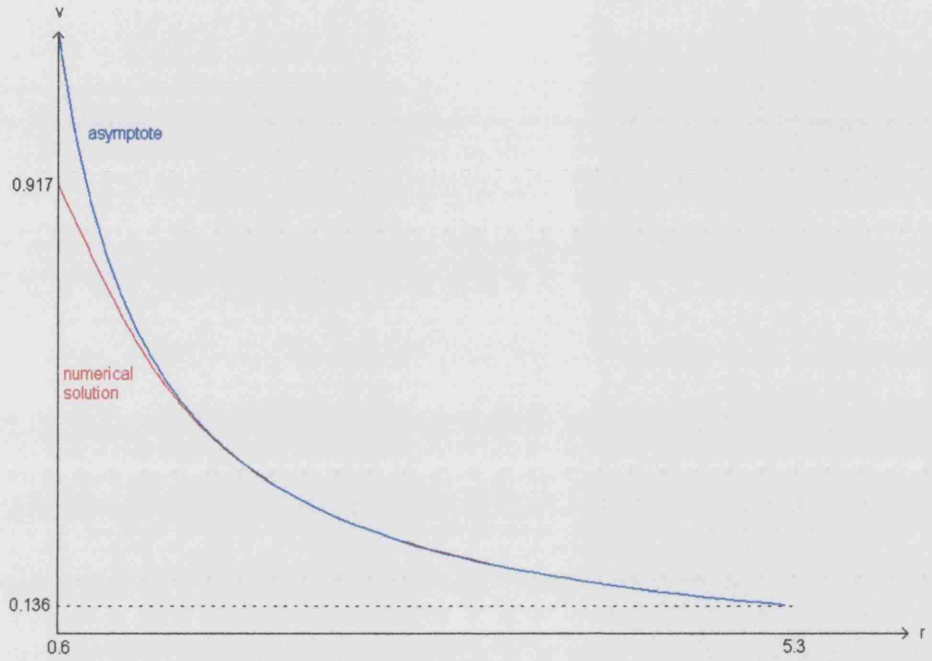

Figure 6.7: Comparison of v against r and asymptote c/r at $\theta = \pi$ (square nozzle).

Once the nozzle cross-section has been specified, data pertaining to a single jet can be obtained and this, along with the nozzle parameters, can be used to extrapolate the velocity data necessary to position this single jet into a specific location within a larger array of similar jets. The data (for a single jet) is extrapolated by assuming, as we have done previously, that at large distances from the jet's centre the velocity profile will tend towards that of the axisymmetric case. Hence, in the far-field, $v \simeq c/r$ for some constant c and radius r, at the point being considered. Figures 6.7 and 6.8 illustrate that the numerical potential-flow solution does indeed converge to the asymptotic

axisymmetric solution when considering the solution along the axial arms (i.e. when $\theta = n\pi/2$, $n \in Z$).

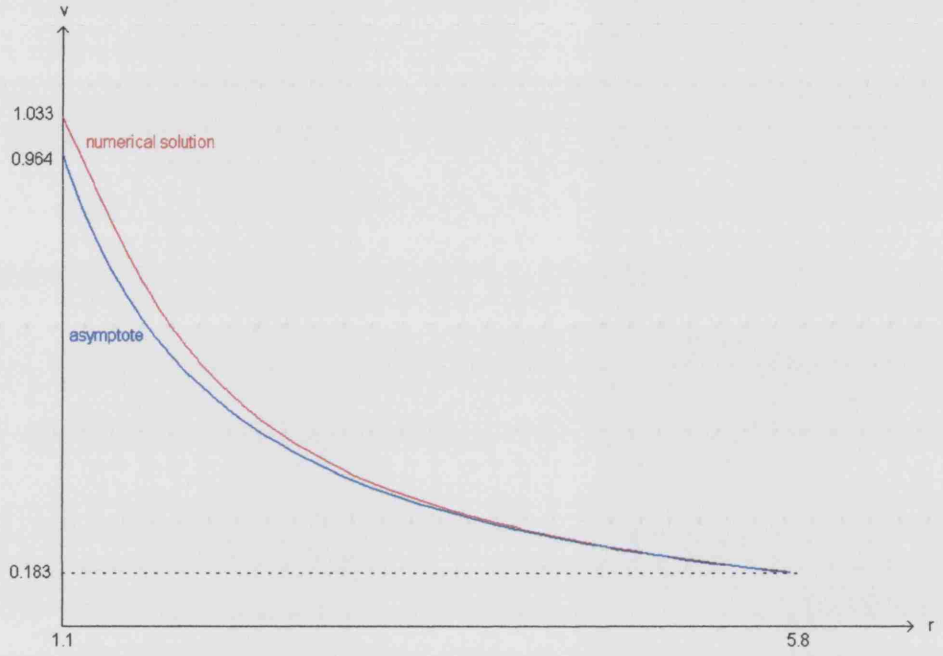

Figure 6.8: Comparison of v against r and asymptote c/r at $\theta = \pi$ (rectangular nozzle).

However, comparing the values of v along radial arms which do not lie on the coordinate axes, such as those at $\theta = (2n+1)\pi/4$ for instance, with the above asymptote, highlights the importance of θ dependence in the asymptote. For instance, figure 6.9 illustrates one such comparison for a 1 x 1 square nozzle. In this case, when $\theta = \pi$ and $r = 5.3$, $v = 0.27$. However, at $\theta = 3\pi/4$ and $r = 5.3$, $v = 0.18$, suggesting that $v(r = 5.3, \theta = 3\pi/4) = \frac{2}{3}v(r = 5.3, \theta = \pi)$.

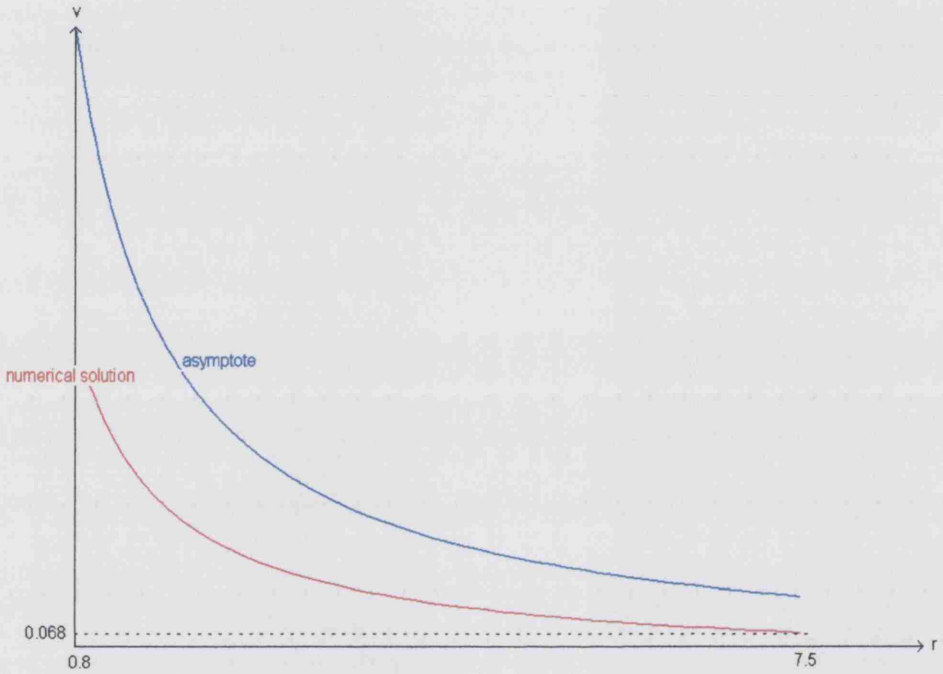

Figure 6.9: Comparison of v against r and asymptote c/r at $\theta = 3\pi/4$ (square nozzle).

Since the v-velocity components are positive in the second and third quadrants but negative in the first and fourth quadrants, the properties of the cosine function can be exploited to introduce a correcting factor. Measuring θ in a clockwise manner as illustrated in figure 6.10 we take $v = \hat{c}/r$, where $\hat{c} = c\cos(\alpha\theta)$ say, so that in the above example $\theta = 0$ implies $\hat{c} = v \cdot r = 1.431$. Hence $\alpha = \frac{4}{\pi}\arccos(\frac{2}{3}) \approx 1.071$.

Generally, α will have to be calculated for each different nozzle cross-section,

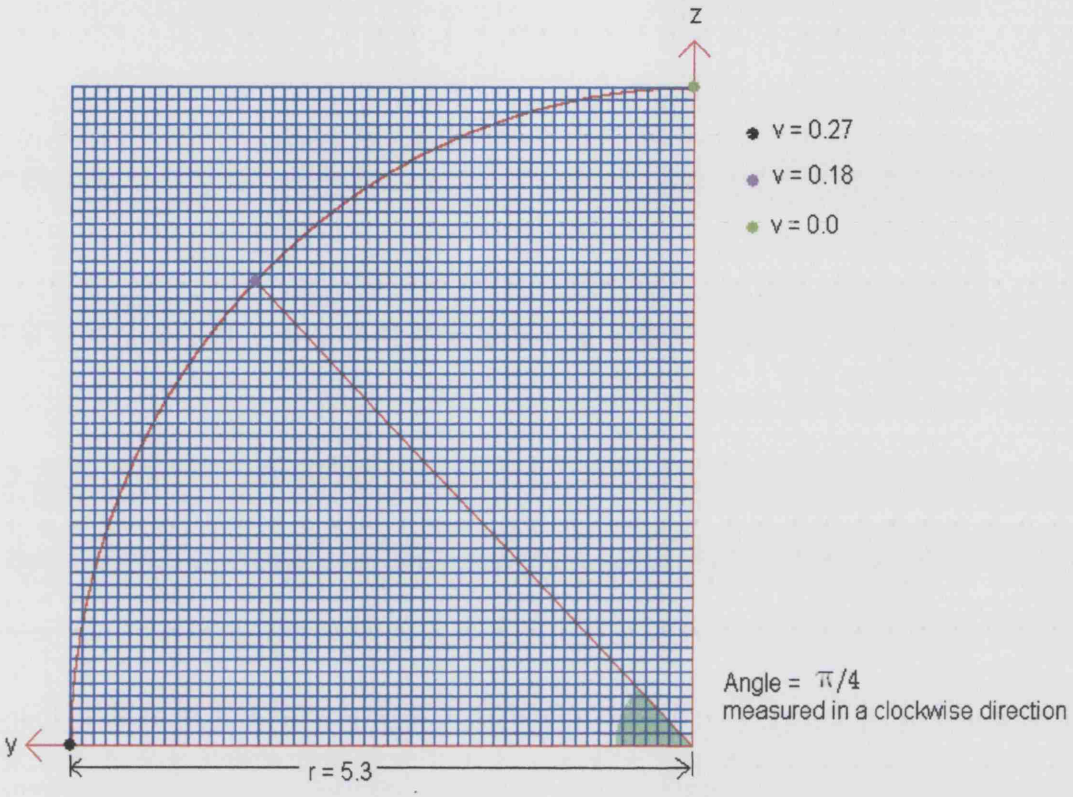

Figure 6.10: v dependence on θ, θ measured clockwise.

but this is quite straightforward. However, the computer program developed has been designed so that $4.9 \leq r_{max} \leq 7.8$ along $\theta = 0$ in order to accommodate many different nozzle cross-sections, ranging from 0.2mm x 0.2mm to 6mm x 6mm. Therefore it is more convenient to consider the value of v at r_{max} along the radial arm at $\theta = \pi/8$; this ensures that the cell to be considered actually lies within the array holding the v values. For example, if a nozzle of cross-section 6mm x 1mm were to be considered, then the array holding the v values would have dimension 157 x 107 and each quadrant would contain 78 x 53 cells. The cells hold values for v at intervals of 0.1mm, thus $r_{max} = 7.8$. However, the cell at $r = 7.8$ along the radial arm at $\theta = \pi/4$

would have to be positioned 55 cells left of, and 55 cells up from, the array's central cell, but this cell is not contained within the array.

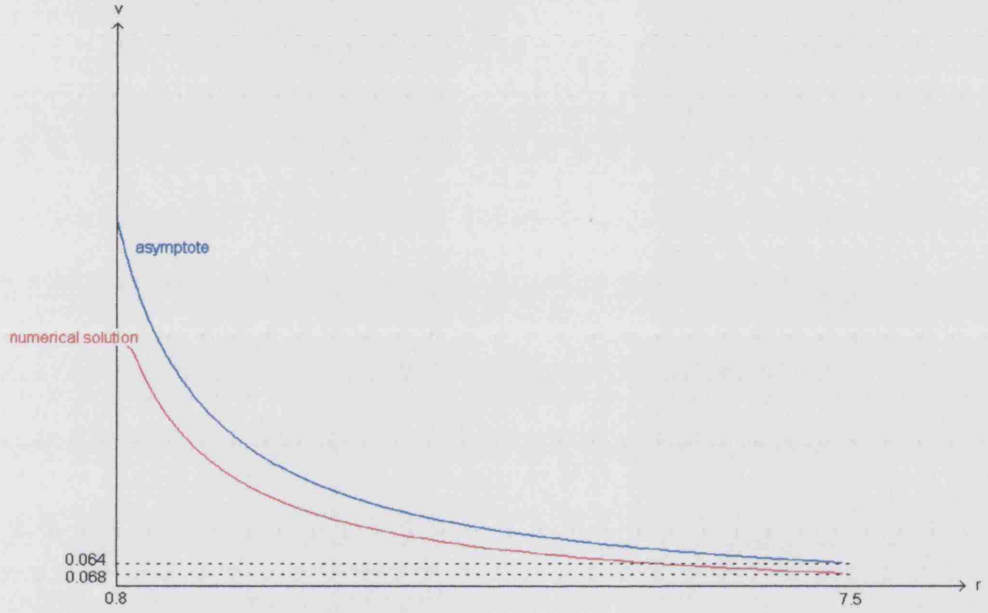

Figure 6.11: Comparison of v against r and asymptote at $\theta = 3\pi/4$ with θ correction.

Using the simple θ correction factor outlined above produced very good results. Figure 6.11 and the contour plots, produced for a variety of nozzle cross-sections, illustrated in figure 6.12 demonstrate clearly how well the extrapolated data fits with the numerical solutions. Note, however, that the extrapolated (multiple) jet solution only produces enough data to demonstrate each jet's interactions with other jets being considered, and to show its position within the array. Hence, since in figure 6.12 only single jets are being depicted, the solution is automatically truncated.

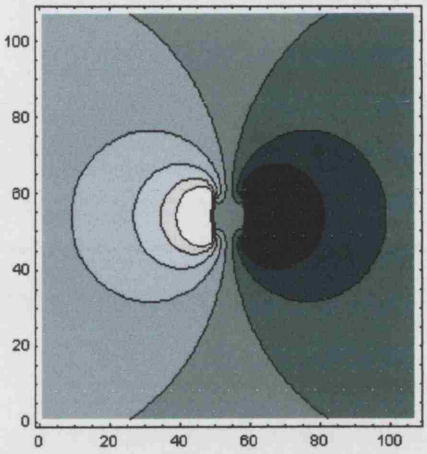

Potential flow solution for a single 1x1mm nozzle (restricted solution domain).

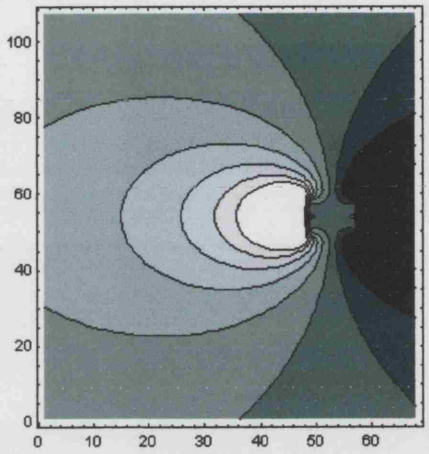

Solution with extrapolated data placed at position 3 of a larger array.

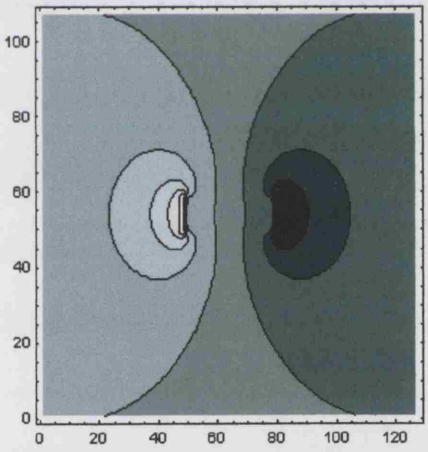

Potential flow solution for a single 3x1mm nozzle (restricted solution domain).

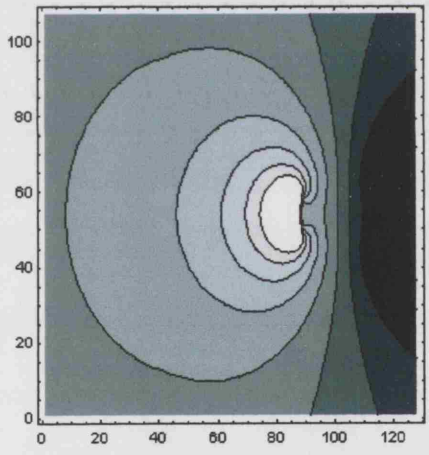

Solution with extrapolated data placed at position 3 of a larger array.

Figure 6.12: Contour plots of (restricted solution domain) potential flow solution for 1x1mm and 3x1mm nozzles and solutions with extrapolated data placed in larger arrays.

As stated above, the multiple in-line steady rectangular jet solution extrapolates the numerical data for a single jet sufficiently to place each jet into its relevant position within the larger array of jets being considered. This positioning also allows for varying the gap between neighbouring jets in increments of 0.1mm. We illustrate next various results produced for 3x1mm nozzles with 1mm gaps between neighbours, within an array of three nozzles. It should be noted that we have chosen this restricted solution domain only for clarity and note that the maximum number of jets that can be considered is restricted only by the maximum array size allowed by the machine and programming language being used. Hence the total number of nozzles that can be considered is in excess of the maximum number required to be considered in the Sortex case.

The graph on the top-right of figure 6.13 illustrates that only enough data is extrapolated to position the jet appropriately. Since no jets beyond position 3 are being considered the data is truncated at an appropriate point just beyond the core region of the jet in position 3, but is extrapolated far enough in front of nozzle 3 to illustrate its overall position in the array. The plot and graph presented in the middle of figure 6.13 illustrate steady jets in positions 1 and 3 of the array being fired. The graph clearly shows how the crossflow from each jet affects the other. Note, particularly, how the flow within each jet's core increases under the influence of the other jet's crossflow. The final graph, in which the nozzles neighbour each other, separated only by a 1mm gap, shows a similar but more pronounced result, and demonstrates that the flow within each jet's core region increases in the direction of its neighbour.

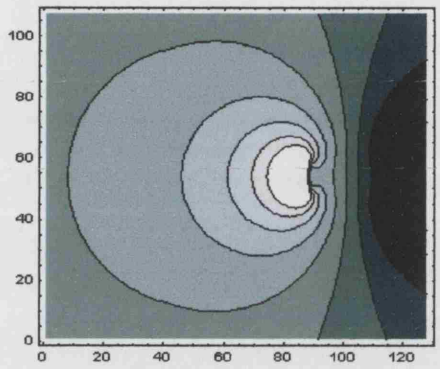

Contour plot of v for 3x1mm jet in position 3 of larger array.

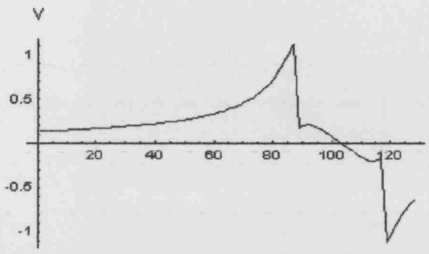

Numerical value of v along axis (z = 0) for single jet in position 3.

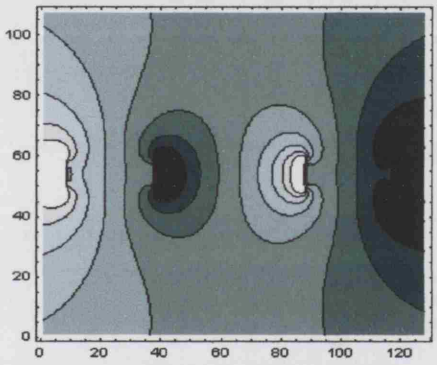

Contour plot of v for 3x1mm jets in positions 1 and 3 (1mm gap between neighbouring nozzles).

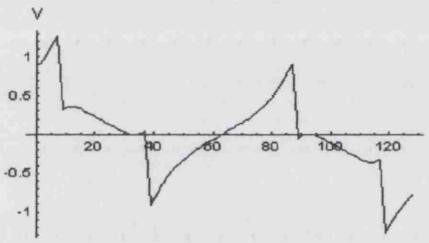

Numerical value of v along axis (z = 0) for jets in positions 1 and 3.

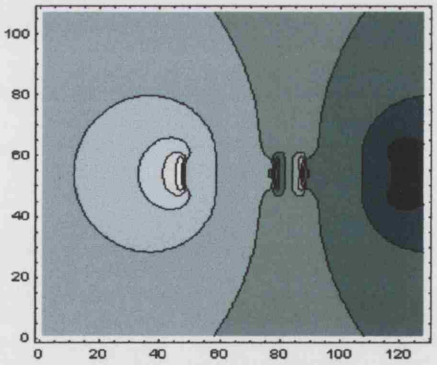

Contour plots of v for 3x1mm jets in positions 2 and 3 (1mm gap between nozzles).

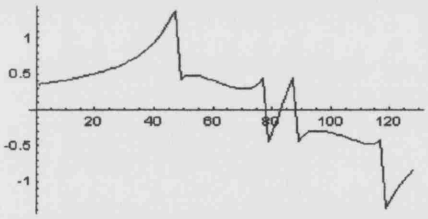

Numerical value of v along axis (z = 0) for jets in positions 2 and 3.

Figure 6.13: Crossflow solutions for steady jets issuing from 3x1mm nozzles.

In the core of a single square jet there is virtually zero crossflow, initially. However, in rectangular jets the initial core crossflow, though small, increases marginally with increased jet width and is directed towards the jet's centre. As the number of jets in the array increases each jet competes to suck fluid from its neighbours, in order to sustain itself. Irrespective of jet cross-section, the crossflow is increasingly directed towards the centremost jet in the array with increased number of jets. However, the crossflow within the core of the centremost jet is now directed away from its centre as it is pulled toward neighbouring jets. The growth in crossflow is most notable at the array extremes.

6.5 In-parallel steady round jets

In accordance with section 6.3.1 we take v_0 within the core-region of the single axisymmetric jet to be zero, and satisfy the jump condition on the core-edge boundary C by letting v_0 be equal to some arbitrary constant there. We note, however, that the value of the arbitrary constant k, say, is necessarily negative at all points on C, since this reflects the fact that the radial velocity v is in the direction towards the jet's centre at this early stage of the jet's development because the jet is entraining fluid from the surrounding medium. We then impose $v \sim k/r$, where r represents the radial distance from the jet's centre, for all values of r outside C. The solution for a single jet with $k = -10$ imposed on C is illustrated in figure 6.14. As in the rectangular case, the solution for multiple in-line jets is produced by adding on linearly the solution for the single jet, subject to the axial displacement. Examples

are illustrated in figure 6.15 with $k = -10$ imposed on C.

6.6 Comparing steady rectangular and round jet solutions

Of particular interest to the industrial application are comparisons of crossflow/interference properties of jets issuing from nozzles of rectangular cross-section with those of jets issuing from nozzles of different rectangular cross-sections and also those issuing from round nozzles. Since we have already briefly discussed similarities and differences between jets issuing from square nozzles and those issuing from rectangular nozzles, we take the time here to illustrate the similarities and differences between the crossflow characteristics of jets issuing from square nozzles and jets issuing from round nozzles.

Figure 6.16 (top) compares the crossflow solution obtained for a single square jet of width 2mm with that of a single round jet of diameter 2mm, both positioned at the far right of their respective arrays. It should be noted that, as in the preceding sections, a Cartesian coordinate system is used to plot the square jet, hence positive v values indicate flow from left to right and negative v values indicate flow from right to left of the graph. The graph of the round jet illustrates the radial velocity component. Therefore negative v values indicate flow towards $r = 0$. In figure 6.16, the direction of the crossflow is indicated by RED arrows for the square jet and GREEN arrows for the round jet. Figure 6.16 (bottom) compares the crossflow solutions obtained for five square jets and five round jets, each with the above dimensions and

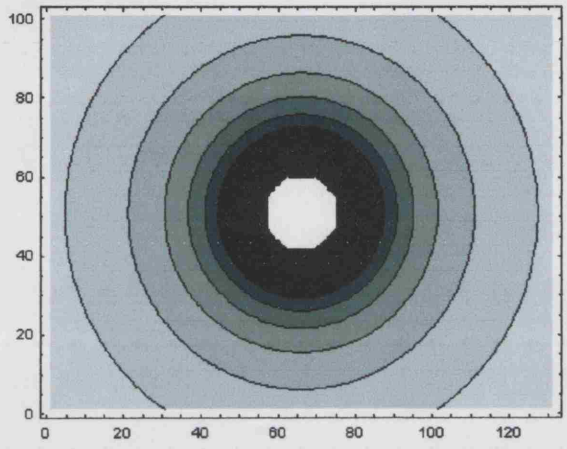

Contour plot of radial velocity for a single round jet.

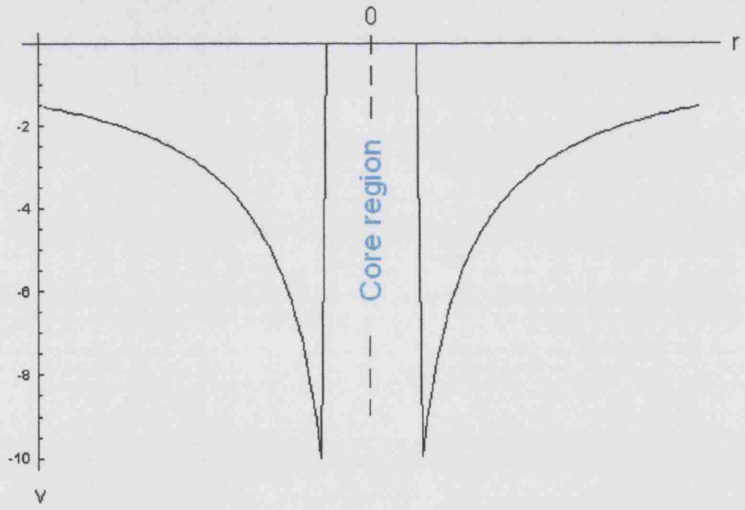

v against r, $\theta = 0$ and $\theta = \pi$.

Figure 6.14: Solution for a single round jet with $k = -10$.

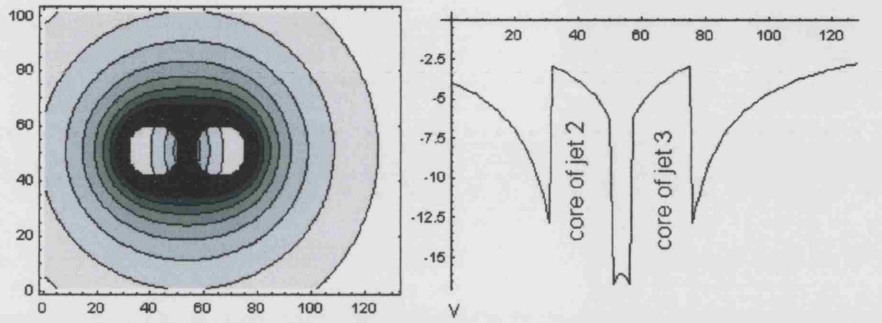

Two round jets in positions 2 and 3 of 5.

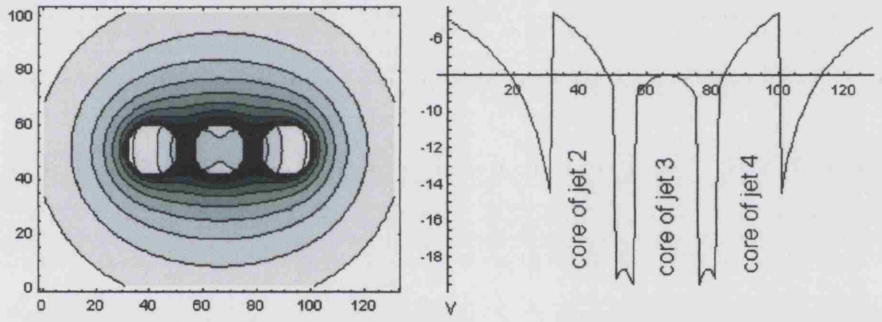

Three jets in positions 2, 3 and 4 of 5.

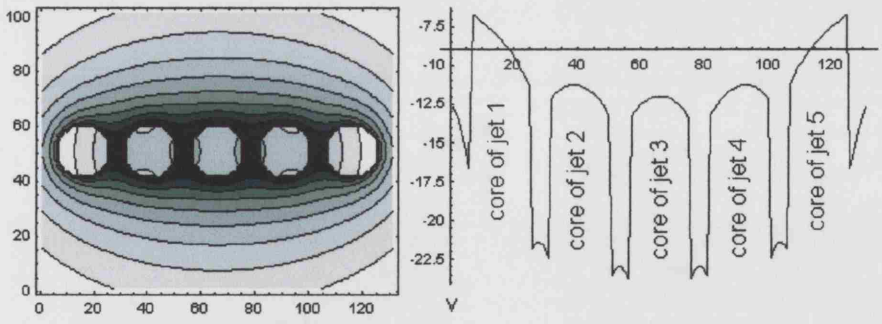

Five neighbouring steady jets.

Figure 6.15: Multiple steady round jet examples. $k = -10$.

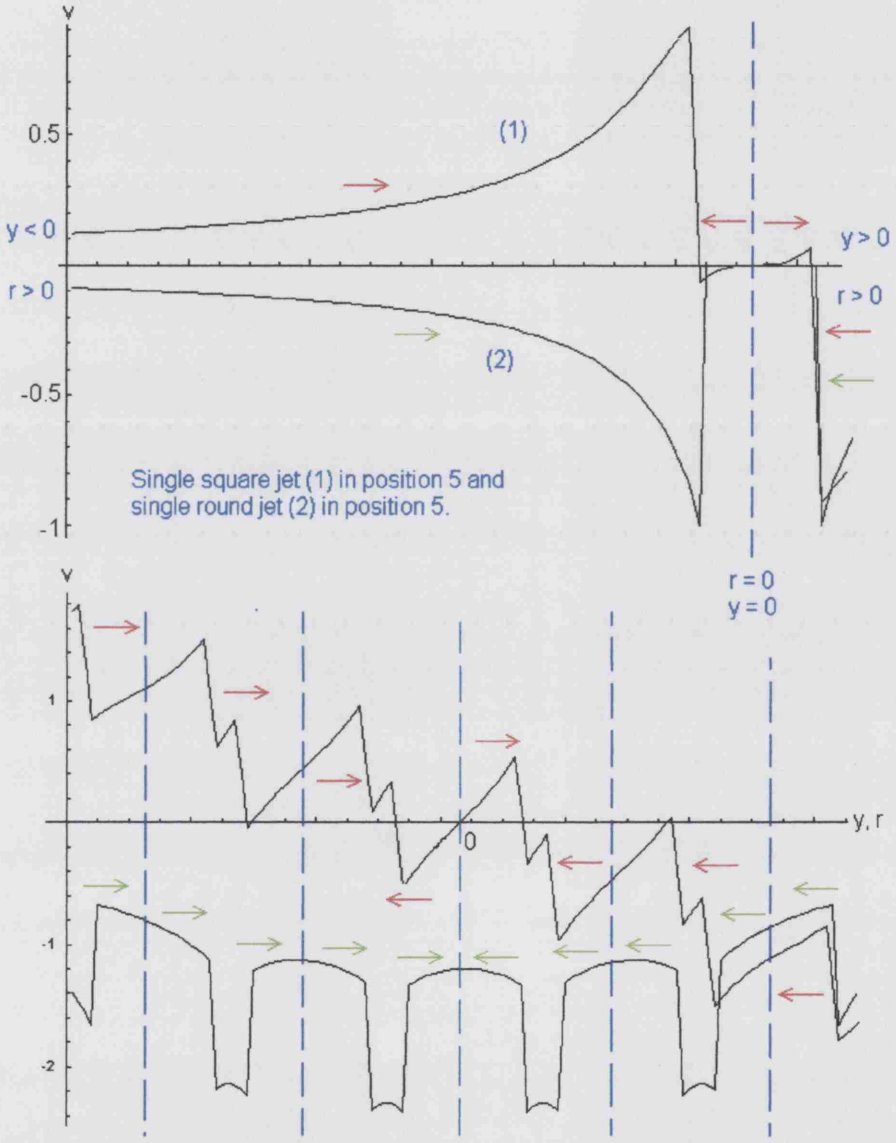

Figure 6.16: (Top) single square jet and single round jet crossflow solutions. (Bottom) Comparison of crossflow solutions for five neighbouring square jets and five neighbouring round jets.

separated by 0.5mm gaps. Reference to figures 6.15 and 6.13 confirms that crossflow increases with increased number of jets. Figure 6.16 shows that, in general, the crossflow is in both cases directed towards the centremost jet, and appears to flow into the centremost round jet but out of the centremost square jet. However, edge-effects are a marginally more dominant feature in the square jet case and, although still influential, appear to be attenuated in the round jet case.

Broadly, and for either type of nozzle cross-section, it is clear that the interference between the jets would tend to draw all the jet flows together. Moreover, the different directions of the central arrows in the figure means that in the square case the interference would tend to concentrate the central jet, whereas in the round case the effect is to diffuse the central jet.

6.7 Unsteady round jets

In this section we extend the multiple round jet potential-flow-like solution of Section 6.5 to include time-dependence. The method of approach, once again, is to consider each jet in turn adding its contribution to the whole solution, subject to its axial displacement. However, unlike in the steady case, several solutions exist for each jet, each pertaining to a single moment in time. The solutions for each individual jet at each time step are obtained by generating the appropriate core-edge values and then solving for the rest of that jet's flow field (driven by those core-edge values). Then, as each time slot is arrived at, the relevant contribution for each jet is added to the total for

all the jets firing. The core-edge values, k_i say, for each jet at each particular time, t, are determined by considering the time-lag of the jet's firing after the first jet to fire, and can be represented simply by an expression such as

$$k_i = (t - L_i)(1 - (t - L_i))H, \tag{6.11}$$

subject to $L_i \leq t \leq 1 + L_i$. We realize that strictly the k_i should be governed via the particular prescribed u_0'' and u_{0t} dependencies through an extension of the integral in 6.10, but here we model the additional unsteady effects by means of 6.11. Here H is a negative constant (since the jet is sucking fluid from its surrounding) and L_i represents the time-lag between the ith jet and the first jet. Note that if $L_i > t$ we let $k_i = 0$, otherwise 6.11 would be meaningless in the sense that it would give a non-zero core-edge value k_i, and this would lead to a non-zero contribution from jet i which is <u>not</u> yet firing.

The crossflow solution for each jet v_i at time t is then given by

$$v_i(t) = \frac{k_i(t)}{r_i}, \tag{6.12}$$

where r_i is the radial distance from that jet's centre. The entire solution at time t is then given by

$$V(t) = \sum_{i=1}^{N} v_i(t), \tag{6.13}$$

where N is the number of jets being considered.

The computer program written for this section has been restricted to produce

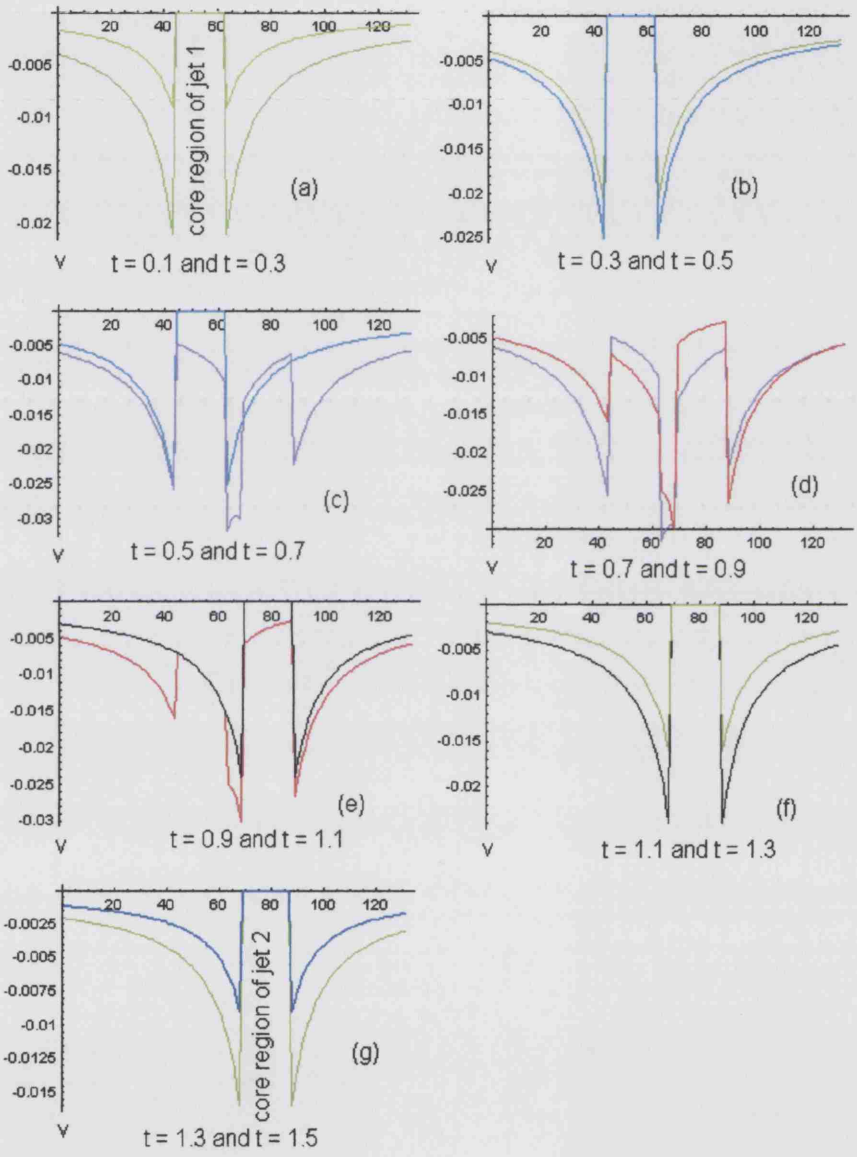

Figure 6.17: Crossflow predictions for two unsteady jets of 2mm diameter, separated by 0.5mm gap and lag = 0.5, at various times over complete solution cycle.

solutions for a maximum of sixty-four in-parallel jets, since this represents the maximum number of nozzles currently used in Sortex sorting machines. Sample output is plotted in figure 6.17 for just two jets firing, however plots for larger numbers of jets with various time-lags are presented in Appendix A. In the example illustrated by figure 6.17, the first jet to fire is active between $t = 0$ and $t = 1.0$, growing and decaying evenly between its maximum at $t = 0.5$. The time-lag between the firing of the jets is 0.5, hence the second jet is active between $t = 0.5$ and $t = 1.5$.

Fig 6.17 (a), (b) show the crossflow increasing as fluid is sucked from the environs towards jet 1 up to its maximum value at $t = 0.5$, at which point jet 2 fires but its profile is not captured until the next time frame, $t = 0.6$ (not shown). Note, however, that at this stage there is no crossflow within the core of jet 1. Figure 6.17 (c) illustrates the crossflow solution just as jet 2 fires and again two time steps into its development. At this point crossflow appears in the cores of both jets as they compete to steal fluid from each other. This also causes the level of crossflow into jet 1 to be maintained and that of jet 2 to be driven up considerably. Two steps further on in time, figure 6.17 (d), we see jet 1 subsiding. The lower crossflow values indicate that it is now struggling to maintain itself, and the increased slope in its core-region indicates that it is now giving-up more of its fluid to jet 2, which is approaching its peak crossflow. By $t = 1.1$, the black graph in figure 6.17 (e), which is one time step after jet 1 has died, jet 2 has passed its maximum crossflow and, although still entraining fluid from the surrounding air, no longer exhibits crossflow in its core.

6.8 Unsteady rectangular jets

In this section we combine the ideas of the previous sections of this chapter to produce results which will enable us to investigate crossflow characteristics of unsteady jets issuing from nozzles of various rectangular cross-sections. In particular we will consider jets issuing from nozzles of 3x1mm cross-section, since these are typical of the dimensions used in food-sorting machines. Results for jets issuing from 4x1mm and 6x1mm rectangular nozzles will be presented in Appendix B. Consideration will also be given to the effects of varying the size of the gaps between nozzles.

The results are obtained by considering the solution for a single steady rectangular jet produced by the program developed for Section 6.2. This is then extrapolated using the method of Section 6.4 so that it can be placed appropriately in the complete solution array. The solution for each active jet is multiplied by the appropriate time-dependent factor given by 6.11 of the previous section and added to the solutions for all other currently active jets.

Figure 6.18 illustrates the development of a single 2x1mm unsteady rectangular jet subject to 6.11 with H given by the solution to the steady jet of like dimensions, up to its maximum crossflow value at $t = 0.5$. According to the present model the crossflow then decays at the same rate. Therefore solutions between $t = 0.5$ and $t = 1.0$ would overlay those in figure 6.18 and they are not presented.

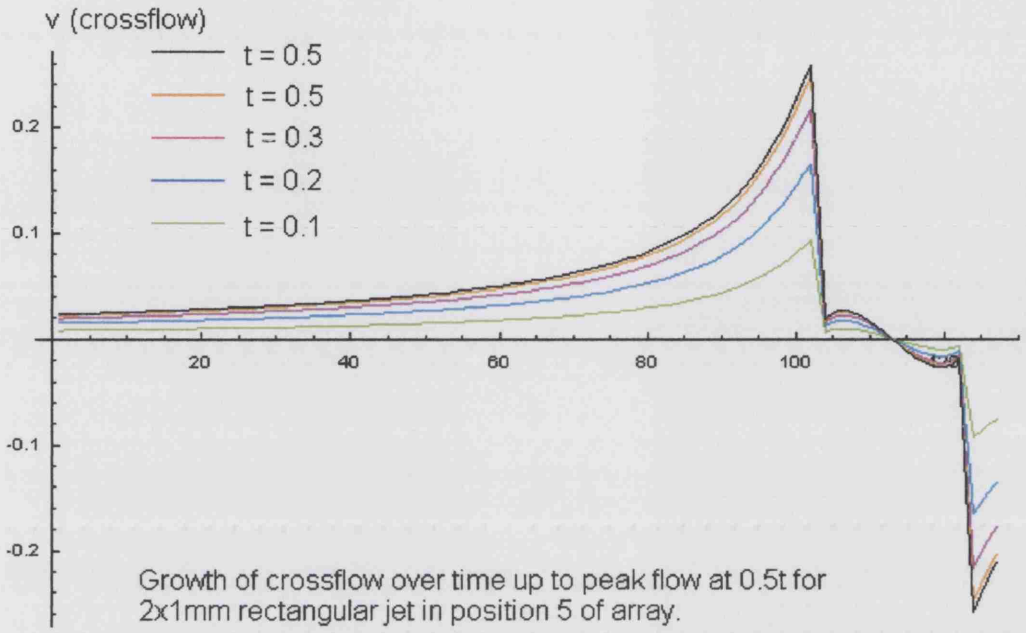

Figure 6.18: Example of a single unsteady rectangular jet developing subject to condition 6.11.

6.8.1 Effects of unsteady firing

In figure 6.19 we present an example of several jets issuing from 3x1mm rectangular nozzles. In this example two neighbouring jets, in positions 2 and 3 of a larger array of currently inactive jets, fire subject to a time-lag of 0.3 and separated by a gap of 0.5mm. Clearly up until $t = 0.3$ jet 2 (the first jet to fire) is not influenced by any other jet and its crossflow response is entirely as expected; fluid is entrained evenly from the ambient fluid. The core crossflow increases slightly and this is directed towards the jet's centre.

Beyond $t = 0.3$ up to $t = 0.5$ the crossflow associated with jet 2 continues to rise until it reaches its maximum value at $t = 0.5$. However, because jet 3 is now active (being 2 steps into its cycle) the crossflow within the core

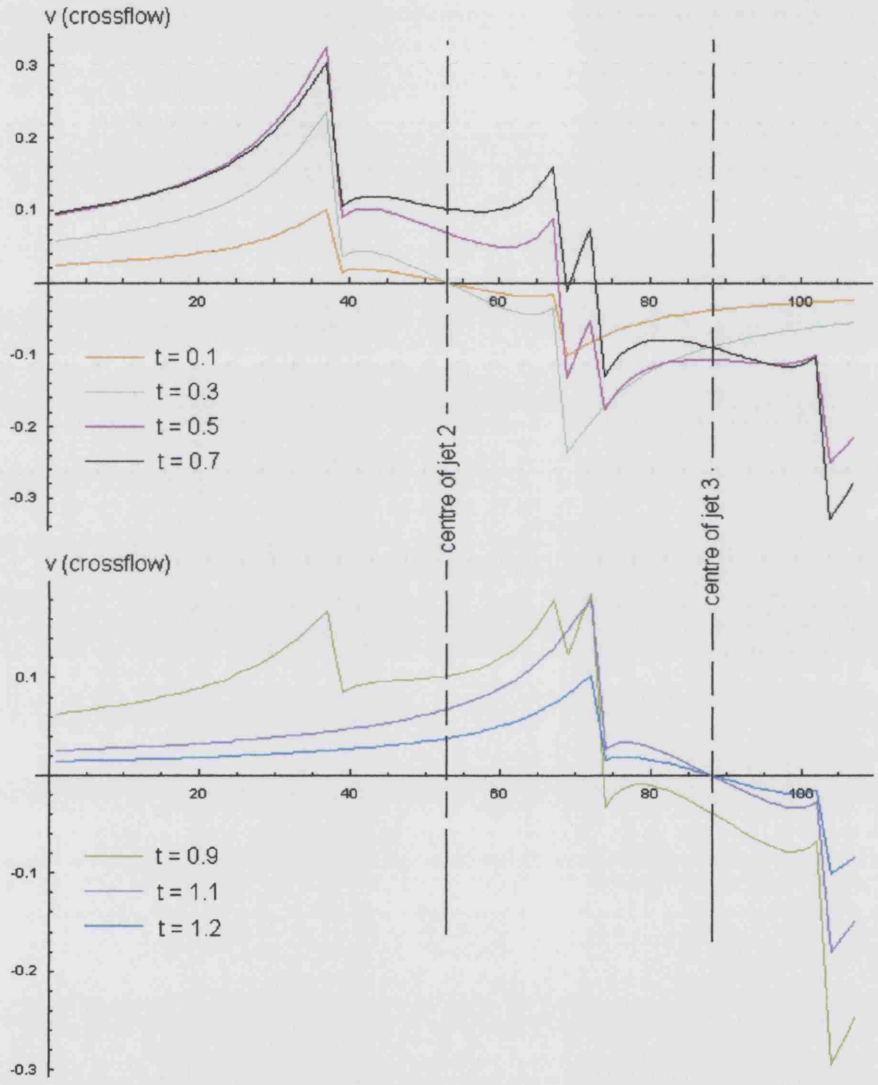

Figure 6.19: Two jets issuing from 3x1mm nozzles subject to a time-lag of 0.3 and separated by 0.5mm gaps .

of jet 2 increases and is sucked towards the other jet. Jet 3, meanwhile, also experiences greater crossflow under the influence of jet 2, with its fluid being sucked towards jet 2. The additional fluid that jet 2 receives from the younger jet 3 enables it to maintain its pull on fluid from the environs. More and more of the fluid is sucked towards jet 3 which, beyond $t = 0.5$, begins to dominate, losing less and less fluid to jet 2. While both jets are active more fluid is drawn into each of them from the external fluid than is given up to the neighbouring jet. Hence there is an overall increase in core flow and a general growth or diffusion of these jets. Eventually jet 3 is effectively firing in isolation, drawing ambient fluid in from the environs. Its core crossflow level subsides but the little that remains is directed towards its centre. We report that a similar response is encountered when the time-lag between the jets firing is increased. We next consider the effects of different gap sizes between nozzle exits.

6.8.2 Inter-nozzle spacing effects

Due to machining constraints, the current minimum gap separating nozzle exits in Sortex sorting machines is 0.5mm. Therefore, at this stage, we consider gaps of increased size but note that the model can produce solutions subject to smaller gaps. Indeed, results for smaller gaps have been demonstrated in earlier sections.

In figure 6.19 (top) at t = 0.5 (pink graph) the first jet to fire (jet 2) has reached its maximum crossflow and the second jet to fire (jet 3) is two steps into its firing cycle. At this point the fluid within the gap between the nozzles

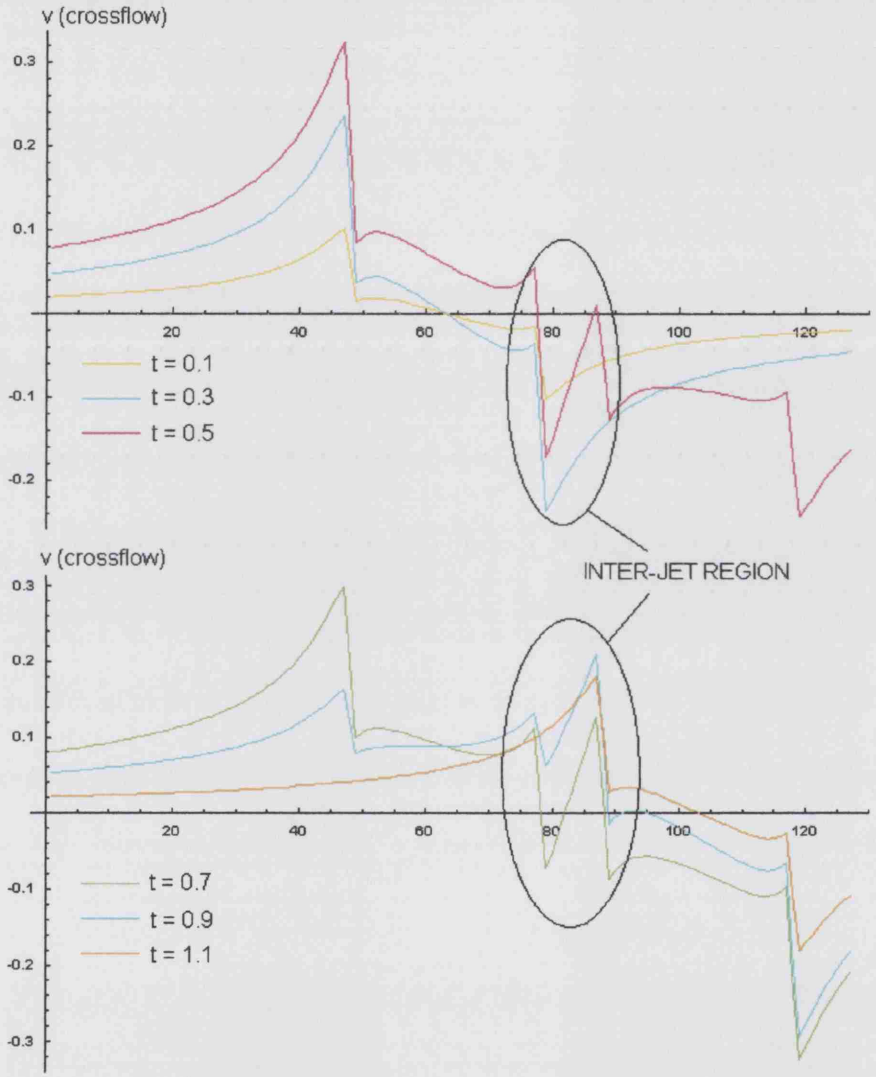

Figure 6.20: Two unsteady 3x1mm jets separated by a 1mm gap and time-lag of 0.3. The ringed areas highlight the 'inter-jet region'..

is flowing towards the more dominant jet (jet 2) with increasing velocity as it approaches. This evacuation of fluid away from jet 3 causes the crossflow within the core of jet 3 to increase and to be pulled towards jet 2. By t = 0.7 (black graph) jet 2 is struggling to maintain its dominance and the flow of fluid in the gap between the nozzles has reversed direction. It is now being drawn back towards jet 3, which at this stage is marginally more dominant. The crossflow in jet 2 is driven up and dragged towards jet 3, causing jet 2 to continue to entrain fluid from the outer regions of its environs.

Figure 6.20 illustrates two neighbouring jets firing subject to a time-lag of 0.3 but with an 'inter-nozzle' gap of 1mm. The jet development pattern associated with the previous example can still be seen and the behaviour of the fluid in the inter-nozzle gap resembles that of the earlier example, too. However, with the increased gap, the graph at t = 0.5 is telling a slightly different story. It seems to suggest that there is virtually zero flow out of jet 3 in the direction of jet 2. This suggests that any fluid drawn into jet 2 from this region must be from fluid already residing in the gap from earlier times. At t = 0.7, unlike the previous case, jet 2, which is now in decline, still draws fluid from the inter-nozzle region in an attempt to preserve itself. However it is soon unable to continue to fight the influence of jet 3 and begins to lose fluid to jet 3 at an increasing rate.

6.9 Summary

In summary of the present Chapter 6, a small-distance analysis of the three-dimensional steady irrotational case gave a clear insight into the nature of interference aspects associated with closely neighbouring jets. The results predicted massive growth in crossflow as the initial u_0 profile was made to approach that described by Smith in [20] and supported earlier small-distance analysis of a similar two-dimensional case. The somewhat unusual initial profiles associated with the jets being studied also meant that potential flow theory could be invoked in a rather novel way. An inherent jump discontinuity associated with each individual jet allowed the solutions for single jets to be added linearly, subject to axial displacement, to obtain the crossflow solution for several or many jets in an in-parallel array. A method for extrapolating the single jet solution to accommodate the axial displacement necessary for placing each jet into a larger array of similar jets was developed and shown to yield very good results. The axisymmetric case was studied and compared with the rectangular case.

A simple time-dependent model for the axisymmetric case was also developed and then extended to the rectangular case so that a program could be written to solve for up to sixty four independent rectangular jets issuing from nozzles of various cross-section and separated by various gaps. We note that, although the current time-dependent model provides a very good insight, empirical data should be used to obtain 6.11.

Other case comparisons and parameter changes might now be made, and

clearly the present approach is able to handle any array configuration in principle. We believe however that the main point is made already concerning the construction of solutions for jet arrays: this can be done simply by the linear addition of individual jet solutions.

Chapter 7

Target Impact Properties

This short chapter is concerned with the properties of the target impact, i.e. the effects of the air jet flow on a representative falling grain of rice, as depicted in figure 7.1. In reality this is a complex three-dimensional unsteady flow problem and it is very difficult to determine the flow accurately. Our interest here is more in modelling the typical overall effects, and in a simple manner.

A typical rice grain of mass M is assumed to be free-falling with constant downward terminal velocity u, so that

$$Mg = a_1 u^2. \tag{7.1}$$

This balances the gravity (g) and air-resistance forces (i.e. drag), the latter being taken to be proportional to the square of the speed, with a_1 being a constant. The impact of an air jet on the grain's motion is considered next.

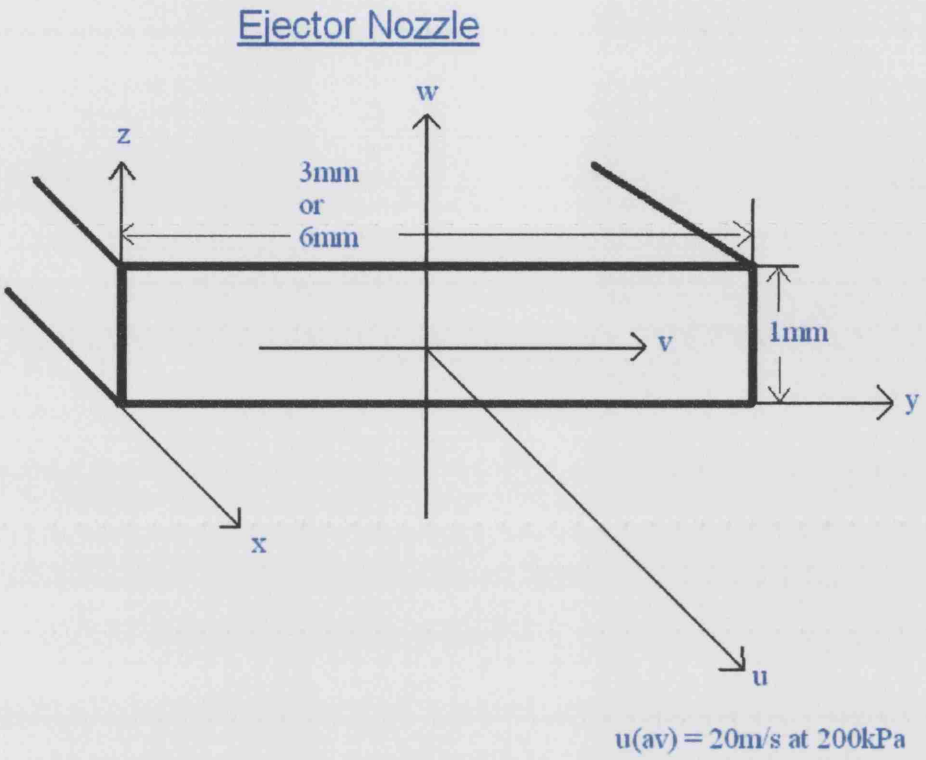

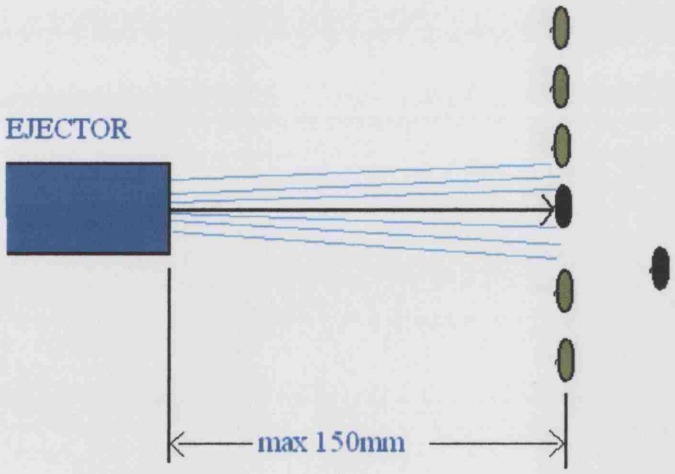

Figure 7.1: Above: typical Sortex ejector nozzles. Below: Jet impact with rice (particle).

7.1 Impact by a horizontal jet

Suppose firstly that the grain of rice enters and passes through a relatively thin horizontal jet of air of thickness h and relatively high air speed W. Assume also that the effect is an impulsive one such that the vertical velocity component of the grain remains u but the horizontal momentum produced is Mv, where v is the horizontal velocity component of the grain of rice as a result of the jet impact, i.e. immediately after impact. Then momentum and impulsive-force considerations imply that

$$a_1 W^2 Dt = Mv \tag{7.2}$$

is such a model.

Here the left-hand side comes from the resistive force evaluated as if instantaneous steady flow around the rice grain is set up and acts over the short time $Dt(= h/u)$ in which the rice grain remains in the jet. The right-hand side change of momentum balances this. Eliminating a_1/M between 7.1 and 7.2 leaves the relation

$$v = \frac{ghW^2}{u^3} \tag{7.3}$$

which serves to determine the horizontal speed provoked by impact, and hence the slope v/u.

The argument strictly holds for $W >> v$ and $W >> u$. If W and v are comparable then W^2 in 7.2 and 7.3 might reasonably be replaced by $(W-v)^2$,

giving

$$a_1(W-v)^2Dt = Mv \tag{7.4}$$

and hence

$$v = \frac{gh(W-v)^2}{u^3}, \tag{7.5}$$

but we will keep to the strict formulae of 7.2 and 7.3.

In his current PhD research project Mr Andrew Ellis gives the downward terminal velocity of the rice grains at the end of a chute (prior to any impact) in Sortex series 90000 sorting machines as between 5 and $10m/s$; Neve [35] places the jet speed in the target area, W, at between 7 and $16m/s$. Therefore, taking $g = 9.8m/s^2$ and $h = 1mm$ we plot, in figure 7.2, v against W for an appropriate range of grain downward velocity values u. We note that the linear relationship between v and h in 7.3 means that for jets of greater thickness v is easily found.

The results appear to make good physical sense. For instance, fast moving grains get deflected much less by a given jet, whereas 7.3 predicts that a thicker jet provides more deflection. However, it seems that in the case of Sortex jets the angle of deflection is very small even in the case of a jet with velocity $W = 20m/s$ and thickness $= 5mm$ hitting a grain which has terminal downward velocity $5m/s$. In that case the angle of deflection is still only around 1.8 degrees from vertical. Reducing the grain's downward velocity to $4m/s$ more than doubles the deflection angle to approximately 4.5 degrees. Similarly, increasing the jet velocity to $30m/s$ also more than doubles the angle of deflection, and combining both of these changes gives

an angle of almost 10 degrees from vertical. We note also that the gravity force acting on the effective projectile after jet impact should not alter u significantly, until the ground is reached, because the grain is at terminal vertical speed already and so tends to remain at constant downward velocity.

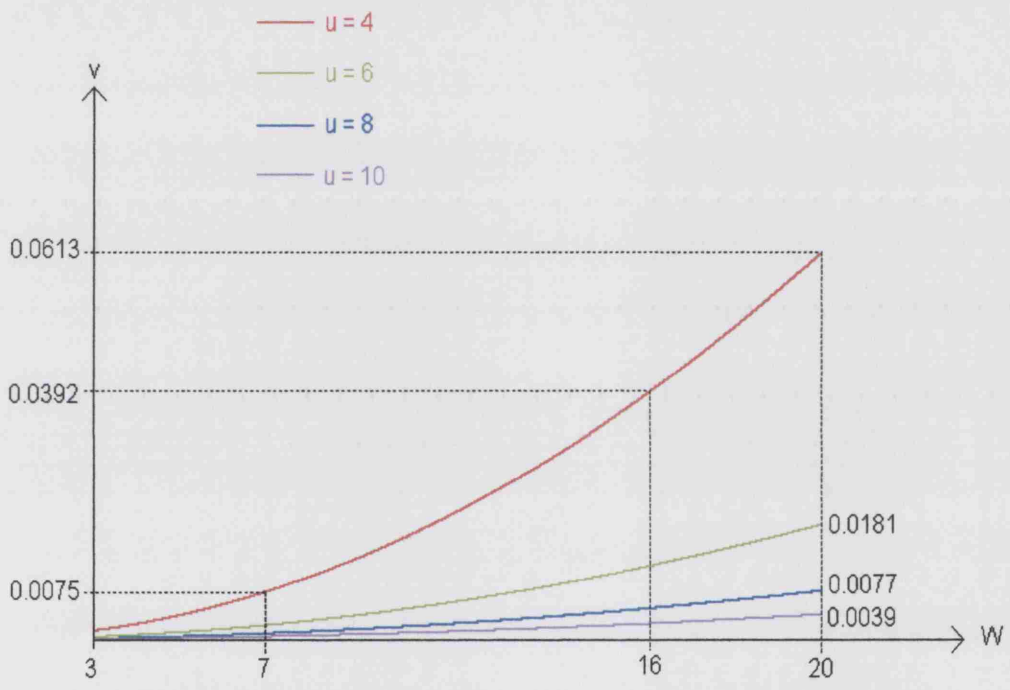

Figure 7.2: Horizontal velocity of grain v m/s plotted against jet speed on impact W m/s.

7.2 Impact by an inclined jet

We now extend the arguments of the previous section to inclined impact by a jet of speed W but at an angle α to the horizontal. The result for the slope

F of the grain trajectory, measured from the downward vertical direction, just after impact, is

$$F = \frac{ghW^2}{(u^4 - ghW^2 \tan(\alpha))}. \tag{7.6}$$

The general result 7.6 for the dependence of F on a general angle α agrees with 7.3 when α is zero, and supports figure 7.2 in such cases, as required. Again, strictly the approximation $W >> u$ is applied. The result 7.6 indicates a critical angle α_{crit} of the jet, given by

$$\tan(\alpha_{crit}) = \frac{u^4}{ghW^2}, \tag{7.7}$$

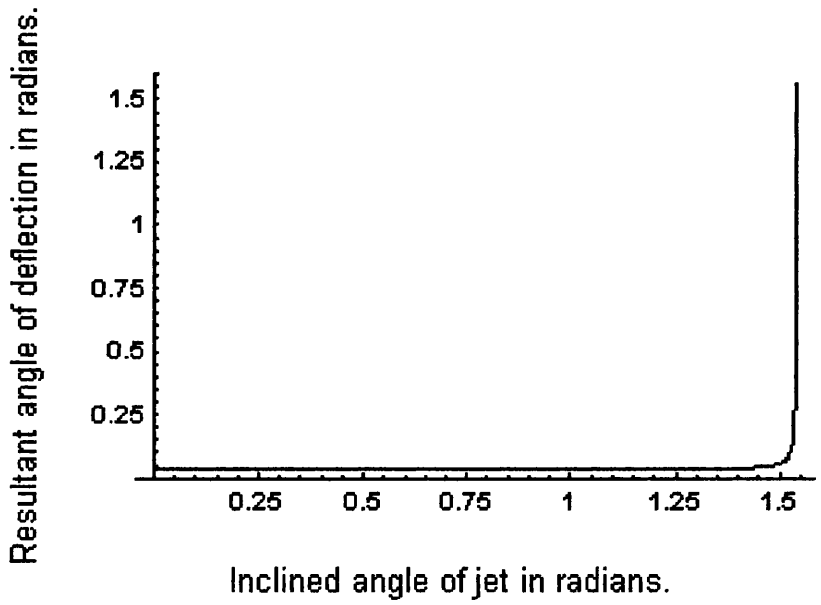

Figure 7.3: Angle of deflection from vertical downward direction against angle of jet inclination α (scales are in radians).

at which the grain would be driven horizontally by the jet impact, according to the model. In the case of a rice grain falling with a terminal velocity of $5m/s$ into an air-jet of thickness $5mm$ and speed $20m/s$, which is perhaps typical of this set-up, 7.7 yields an α_{crit} value of 88.2 degrees. Figure 7.3 plots the resultant angle of the grain's deflection from the vertical downward direction against jet inclination angles between 0 and 1.54 radians (88.2 degrees).

7.3 Comparison with physical study

A study of particle deflection properties has been carried out by Sortex for such particulates as frozen peas and sweetcorn. The results from physical tests that were conducted are contained in [45], [46], [47] and references therein. Figure 7.4 illustrates a typical set-up used to investigate the angle of deflection of frozen peas, which can be summarized as follows. The particles (peas) enter the sorting area via a chute angled at sixty degrees above horizontal and which terminates 230mm above the sorting area (measured along the plane of the chute). Measurements indicate that the particles fall from the chute with a velocity of 4m/s and are following a path at a decreased angle by the time they enter the target area, i.e. their paths are then more vertical. We assume here that this angle might be as much as ten degrees below that of the plane of the chute. The ejector nozzle is positioned 40mm away from the plane of the chute angled at 6 degrees below horizontal and hence inclined at 14 degrees above the perpendicular to the particulate flow. The chamber pressure of the air feeding the jet is between 80 and 100psi,

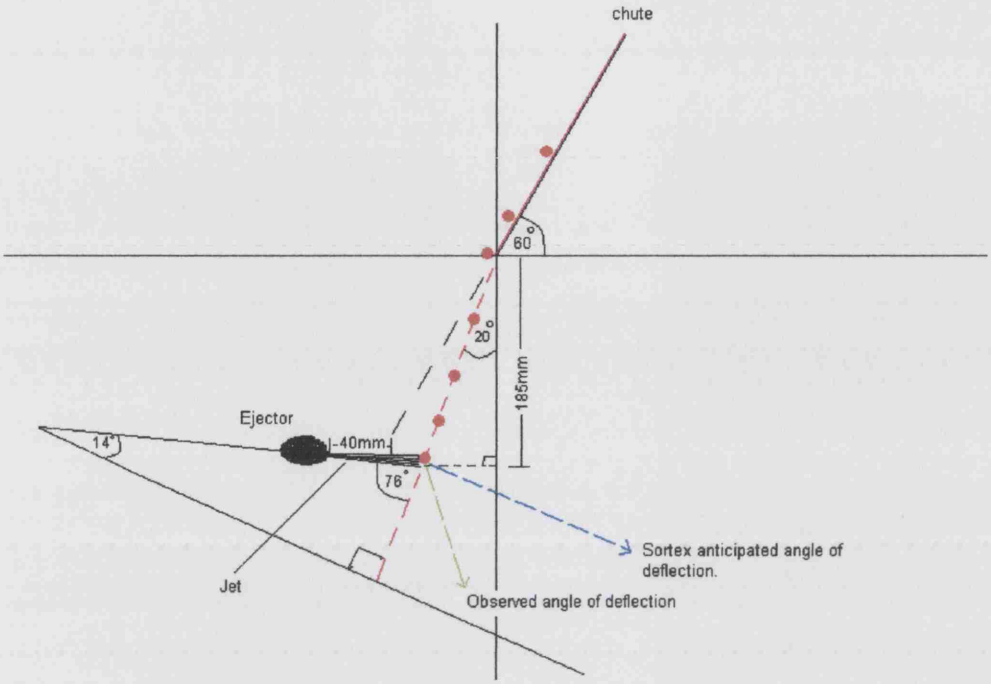

Figure 7.4: Schematic of a typical particle deflection test set-up.

giving an estimated jet exit velocity of between 50 and 70m/s. According to the Sortex model the predicted angle of deflection (blue path in figure 7.4) is perpendicular to the direction of particulate flow. However, the observed angle of deflection (following green path in figure 7.4) is approximately half the predicted angle of deflection, measured from the downward direction of the plane of the particulate flow.

Based on this configuration and assuming a jet thickness of 5mm our model predicts that the angle of deflection would be between 29 and 51 degrees from the vertical downward direction. This compares well with the observed angle of deflection given by the Sortex physical set-up and illustrated by the green path in Figure 7.4.

7.4 Summary

Clearly, any benefit from inclining the jet for the particular case of rice grains being impacted by jets with exit velocities of around 20m/s only comes from very steep angles, but of course these might result in a detrimental effect on the flow of particles following behind. However, if increased angle of particle deflection becomes a more important design consideration then increasing the jet velocity and/or thickness or slowing the particulate flow will all result in a reduced α_{crit} value and hence greater angle of deflection, as seen in the case of frozen peas discussed above. For instance, when considering rice grains, a 30 degree deflection can be obtained from a 60 degree jet inclination if the jet speed is $30m/s$ and the terminal velocity of the grains is $3.5m/s$. In general, improvements can be made by increasing the jet velocity, inclining the nozzle angle or slowing the flow of particles, or any combination of these.

Chapter 8

Summary

This work is mainly concerned with three distinct aspects of slender jets of air issuing from rectangular nozzles. The first aspect is a study of the development and flow characteristics of narrow jets over a relatively short range. The emphasis here is on producing reasonably accurate numerical velocity and pressure solutions for both steady and unsteady cases. This work is contained within Chapters 2, 4 and 5. In Chapters 3 and 6, the second aspect considers the interference associated with several or many narrow jets closely neighbouring each other in an in-parallel array. An unusual feature associated with the solution of a single steady jet makes it possible to use potential-flow theory to solve the multiple unsteady jet case. Comparisons between jets issuing from nozzles of various different cross-sections with various inter-nozzle gaps and time-delays between firing are then possible. Finally, in Chapter 7, jet impact properties on target items are considered. A simple particle deflection model is presented and a comparison with physical data is made. The combined results from this research have clear industrial

application, particularly with respect to food-sorting performance, and it is intended that they be used to help guide design considerations prior to the manufacture of future food-sorting machines.

The thesis can also be considered to have three distinct parts. Part One - Chapters 2 and 3 - investigates two-dimensional jets, employing and then extending previously documented work. The content of these chapters provides the underpinning framework for much of the rest of the thesis. In particular, Chapter 2 uses a classical similarity solution as a far-downstream asymptote to help validate a numerical scheme for the solution of the two-dimensional steady jet. This numerical scheme is, in later chapters, extended to solve the three-dimensional unsteady case. Modifications to the basic two-dimensional scheme to enable solution of the non-symmetric case are explored and small-distance and small-time analyses are conducted. The small-distance analysis is shown to complement the numerical solutions developing from 'smooth' initial profiles, such as those described by Neve [34], [35]. However, that particular analysis is found to be less appropriate for the analysis of jets found in the true industrial setting, as described by Smith [19], [20]. In this case, theory predicts the development of a Blasius type free-shear layer, which cannot be resolved by the above leading-order analysis. An alternative solution method is outlined however, and this might pose an interesting exercise in future study. The small-time analysis describes how we might expect the jet's profile to develop and how viscous forces are essential to contain the jet's lateral spread. Chapter 3 applies the numerical and analytical techniques of the previous chapter to conduct a two-dimensional study of interference

associated with multiple in-line jets. The methods employed are analogous to those used by Smith [9] to investigate interference aspects of multiple in-line two-dimensional wakes. The results confirm that interference is a major concern driven largely by edge effects, which should be studied further.

Part two - Chapters 4, 5 and 6 - is concerned with three-dimensional jets. Chapter 4 extends the two-dimensional numerical solution of Chapter 2 to include an iterative scheme for the solution of the three-dimensional steady jet problem, which is posed in what is essentially a vorticity-velocity formulation. Several tests are conducted to confirm the validity and robustness of the numerical scheme and a small-distance analysis, subject to the same limitations experienced in Chapter 2, is also performed. The pressure equation is derived and solved iteratively, but this is found to be subject to poor resolution in the very small-x range. This problem is overcome easily, however, by employing smaller streamwise steps.

In [20] and [22] it is shown that the growth in swirl throughout the fluid (air) feeding the jets in food-sorting machines can be quite considerable, due to valve properties at the upstream end and because of bends and imperfections in the piping carrying the fluid. Therefore, in Chapter 4, swirl is induced upon the initial jet profile with a range of values. The results predict no appreciable change in centreline jet velocity or pressure. However, the pressure profile does appear to become concentrated around the central streamwise axis. This should be regarded as a positive effect. The numerical solution scheme is extended further in Chapter 5 to include time-dependence. Essen-

tially, the solution to the unsteady problem is obtained by solving the steady jet problem at all points within the entire flow field for each particular time step and, obviously, this is subject to a time-dependent profile at the nozzle. For the present study a simple relationship which gives a symmetrical growth and decay in the initial profile over time is used. This is sufficient to allow ad hoc comparisons with physical results but should be replaced with data obtained empirically if more physically accurate results are required. The solution should also account for non-symmetric (misaligned) initial profiles (as predicted by Smith [20]) by considering a Prandtl transposition, as outlined in the two-dimensional case in Chapter 2.

Chapter 6 addresses the major issue of interference between three-dimensional steady and unsteady in-parallel jets. Small-x analysis of the 'smooth' irrotational case as it is transformed by means of a certain parameter to become less smooth, and ultimately near-discontinuous (so that it resembles the type of profiles of most interest in this study) predicts massive growth in cross-flow as the discontinuous 'top-hat' case is approached. This suggests that in such a case the streamwise velocity component u is constant mostly both within the jet's core and outside of it. Consequently, potential flow theory is applicable but is subject to an unusual feature. On the jet's core-edge boundary there exists a jump-discontinuity. This drives the whole solution and allows single jet solutions to be added linearly to construct solutions to the many jet problem, subject to axial displacement. The result is shown to hold for all nozzle cross-sections. For the present, we consider only rectangular and round nozzles. However, we suggest that elliptical and oval

cross-sections should be investigated as these, intuitively, occupy the middle-ground between the cases studied here and resemble the target items (rice grains) more closely.

Finally, Chapter 7 is concerned with the effect of the air jet flow on a representative falling grain of rice. We construct a simple model for the overall effects and first consider what happens when a particle (grain of rice) falls with terminal velocity into a thin horizontal jet of air. Taking estimated values for the grain's velocity from current research by Mr Andrew Ellis, at UCL, and characteristics of the jet flow from Neve [34], [35], we show that, according to this simplified model, the angle of deflection is actually very small. However, improvements in terms of increased angle of deflection are shown to be possible by: (1) increasing the jet exit velocity; (2) slowing the particulate flow; (3) increasing the jet thickness or (4) any combination of (1) - (3).

Impact by an inclined jet is also considered. Surprisingly, for the typical jet parameters described by Neve and particle velocities predicted by Ellis, the model predicts that the issuing nozzle must be inclined at a considerable angle for any appreciable benefit in terms of deflective angle to be realized. We suggest that such an angle of inclination would most probably lead to an adverse effect on the particulate in terms of slowing and disrupting the flow. However, a lesser angle of inclination can have a positive effect on deflection angle without disrupting the flow too greatly if allied with the considerations given above.

We conclude by comparing the model's prediction of deflection angle against results obtained from a physical test conducted by Sortex Ltd. In this test it was found that the particles (in this case frozen peas) exit the machine's feed-chute, which is inclined at sixty degrees, a short distance above the inspection/sorting area. By the time the particles arrive in the sorting area they are following a more vertical path. Hence, if the ejector nozzle is positioned perpendicular to the plane of the chute (as it was in the original Sortex test) it is actually declined to the plane of the flow of particles. This results in a smaller angle of deflection, as predicted by the model and observed in the experiment. The model's prediction of deflection resulting from an inclined nozzle compares favourably with that observed in the physical test. We contend, therefore, that the model has a clear potential benefit when considering new ejector set-ups.

Appendices

Appendix A

Further Illustrative Examples of Interference Between Multiple In-line Round Jets

We present here, with no discussion, example crossflow velocity plots obtained using the potential flow solution of Chapter 6, for multiple in-parallel steady and unsteady round jets.

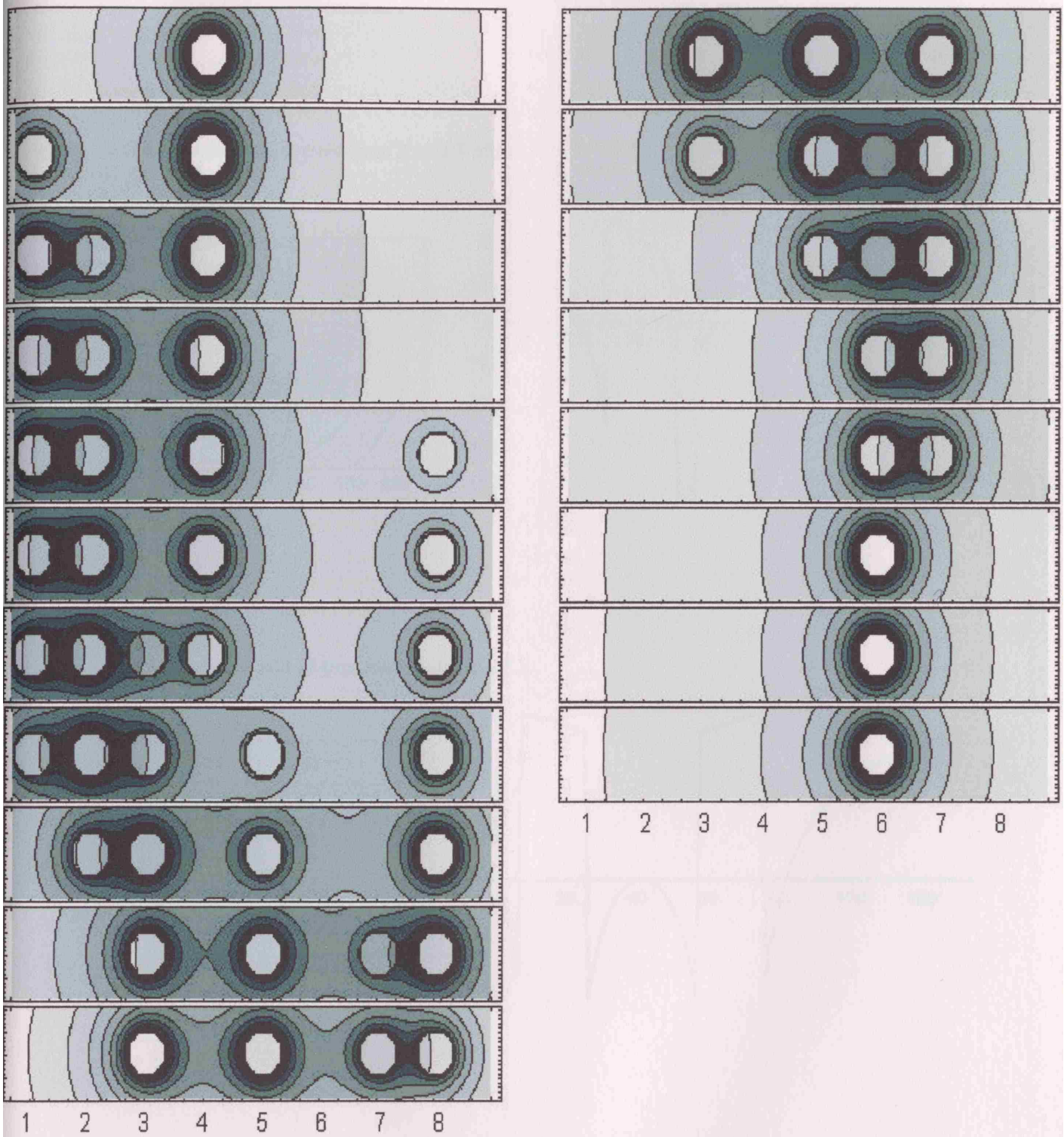

Figure A.1: Eight round jets with firing order: 4, 1, 2, 8, 3, 5, 7, 6 and time lags: 0.1, 0.2, 0.4, 0.6, 0.7, 0.9, 1.2, respectively.

Two round jets at positions 2 and 3 of 5.

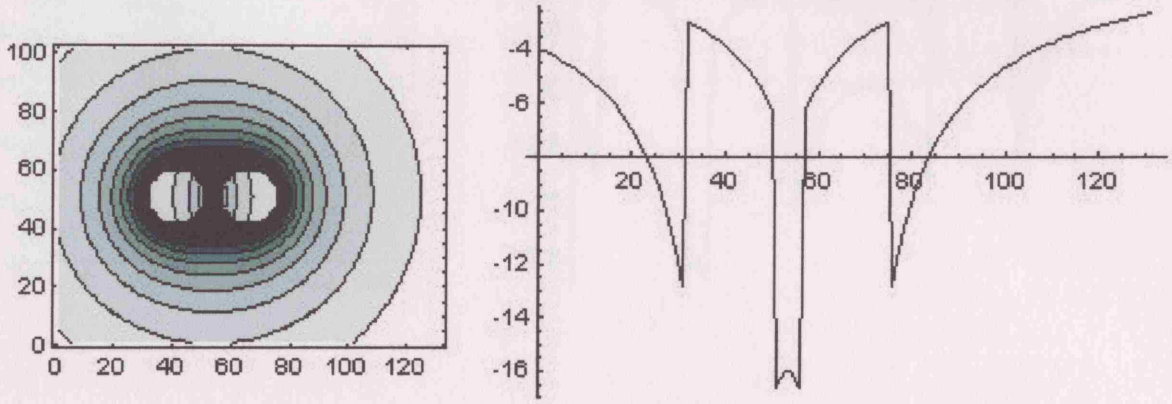

Two round jets at positions 1 and 3 of 5.

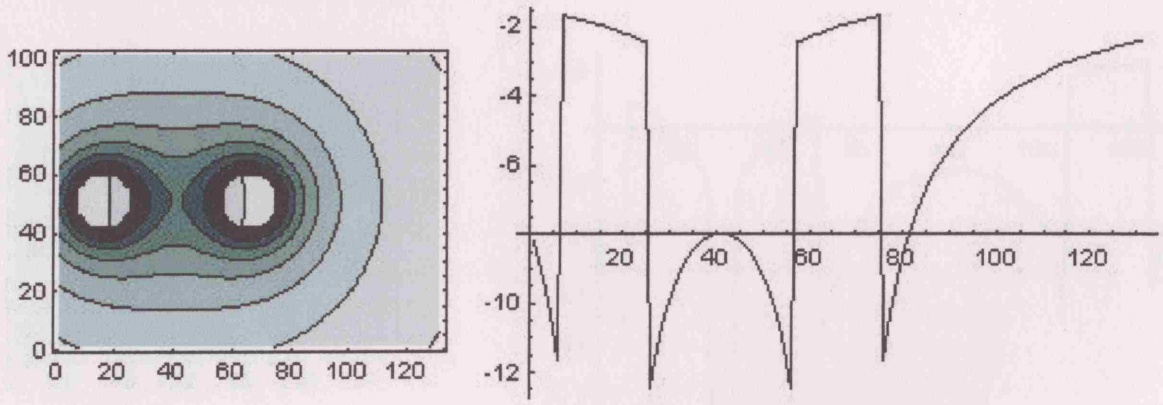

Figure A.2: (Top) two neighbouring steady jets. (Bottom) two steady jets, separated by an intermediate nozzle.

Three round jets at positions 1, 2 and 4 of 5.

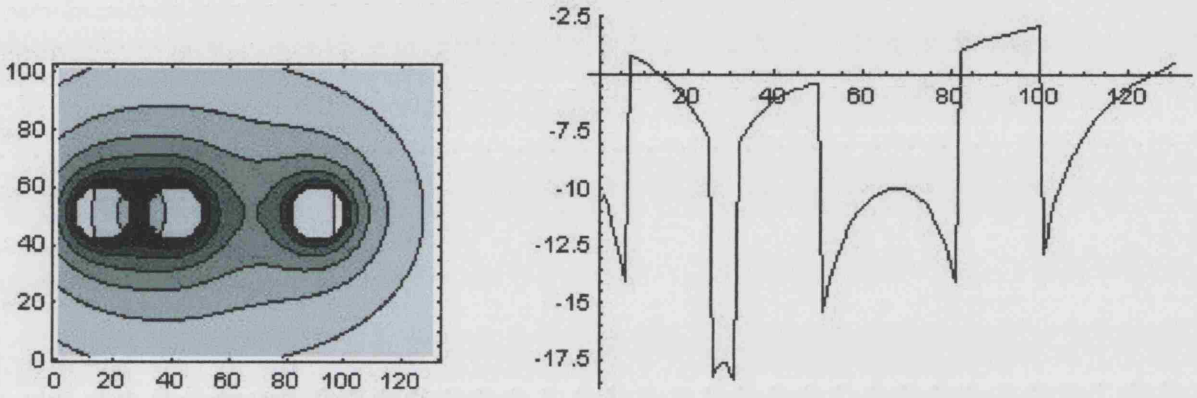

Three round jets at positions 1, 2 and 5 of 5.

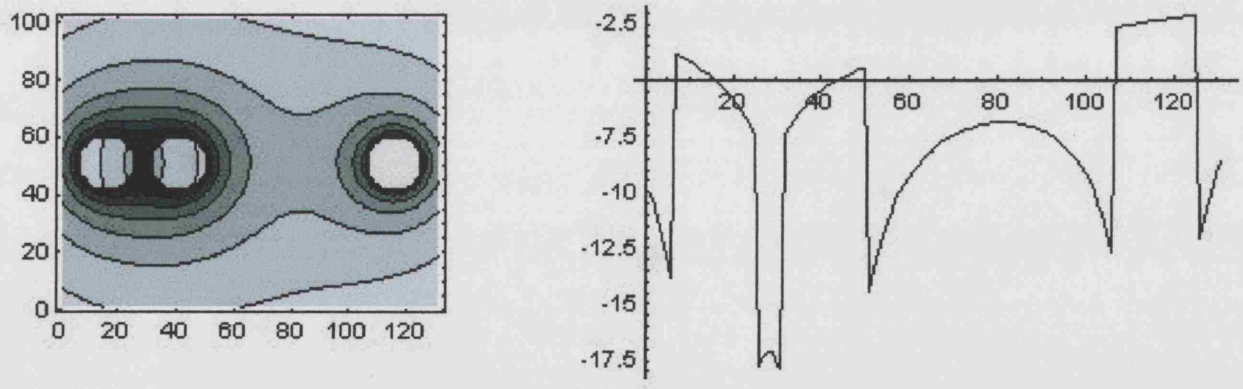

Figure A.3: (Top) three steady jets at positions 1, 2 and 4. (Bottom) three steady jets at positions 1, 2 and 5.

Four round jets at positions 1, 2, 3 and 4 of 5.

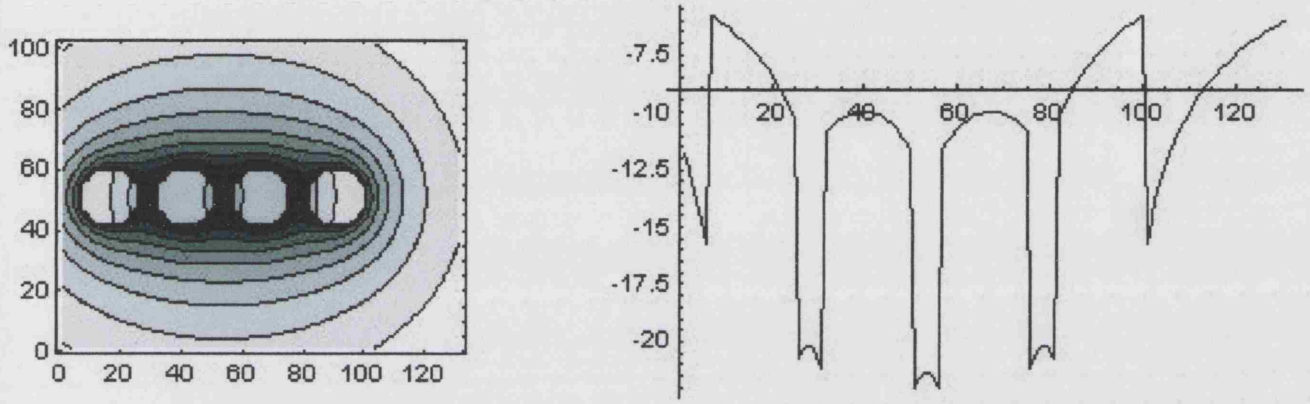

Four round jets at positions 1, 2, 4 and 5 of 5.

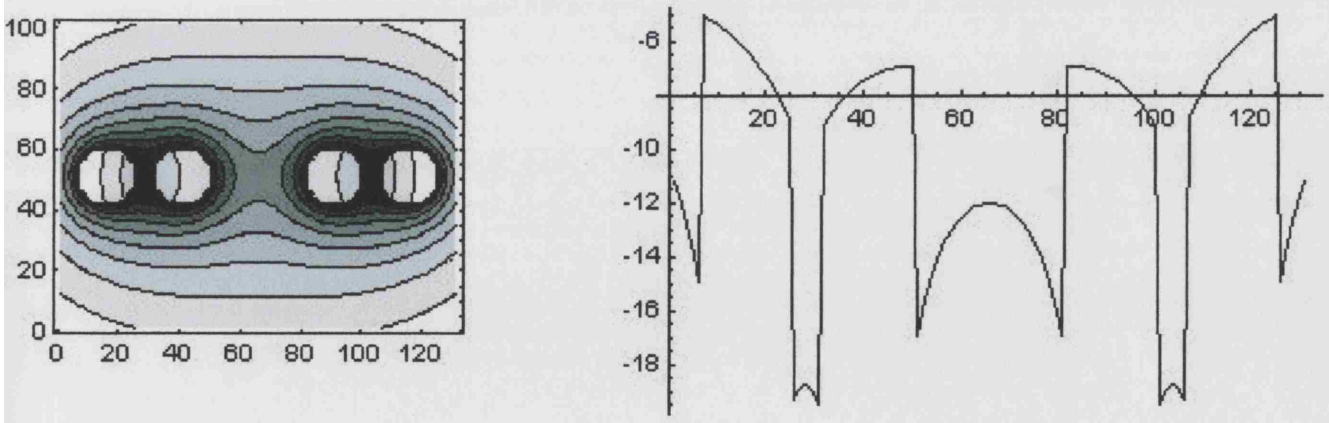

Figure A.4: (Top) four steady jets at positions 1, 2, 3 and 4. (Bottom) four steady jets at positions 1, 2, 4 and 5.

Appendix B

Further Illustrative Examples of Interference Between Multiple In-line Rectangular Jets

We present here various time-dependent cross-flow solutions for jets issuing from 4x1mm and 6x1mm rectangular nozzles. These are typical nozzle cross-sections used in some Sortex machines, but have not been illustrated in Chapter 6.

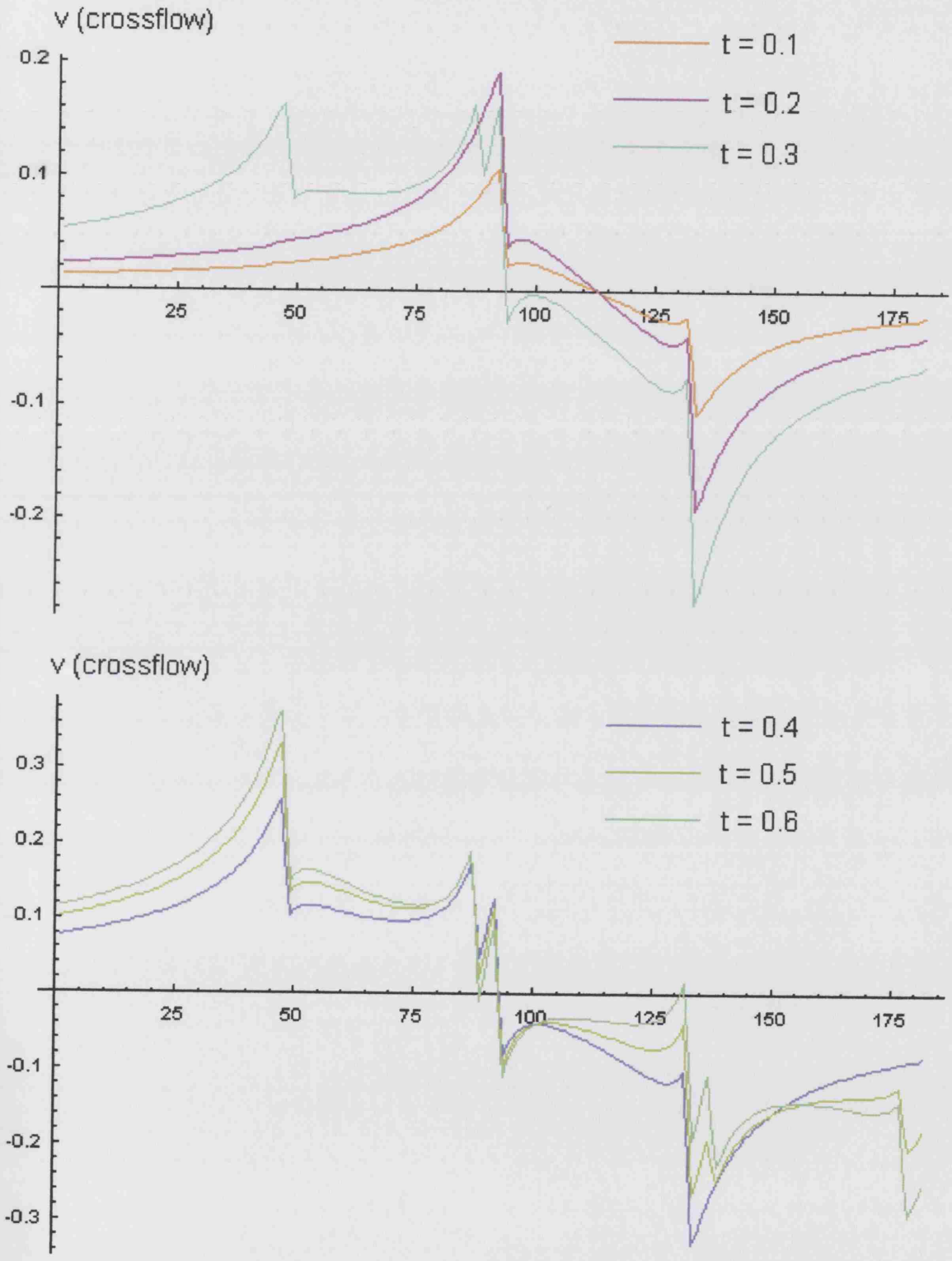

Figure B.1: 4x1mm jets separated by 0.5mm gaps. Jets 3, 2, 4 fired at t = 0, t = 0.2 and t = 0.5, respectively (illustration up to t = 0.6).

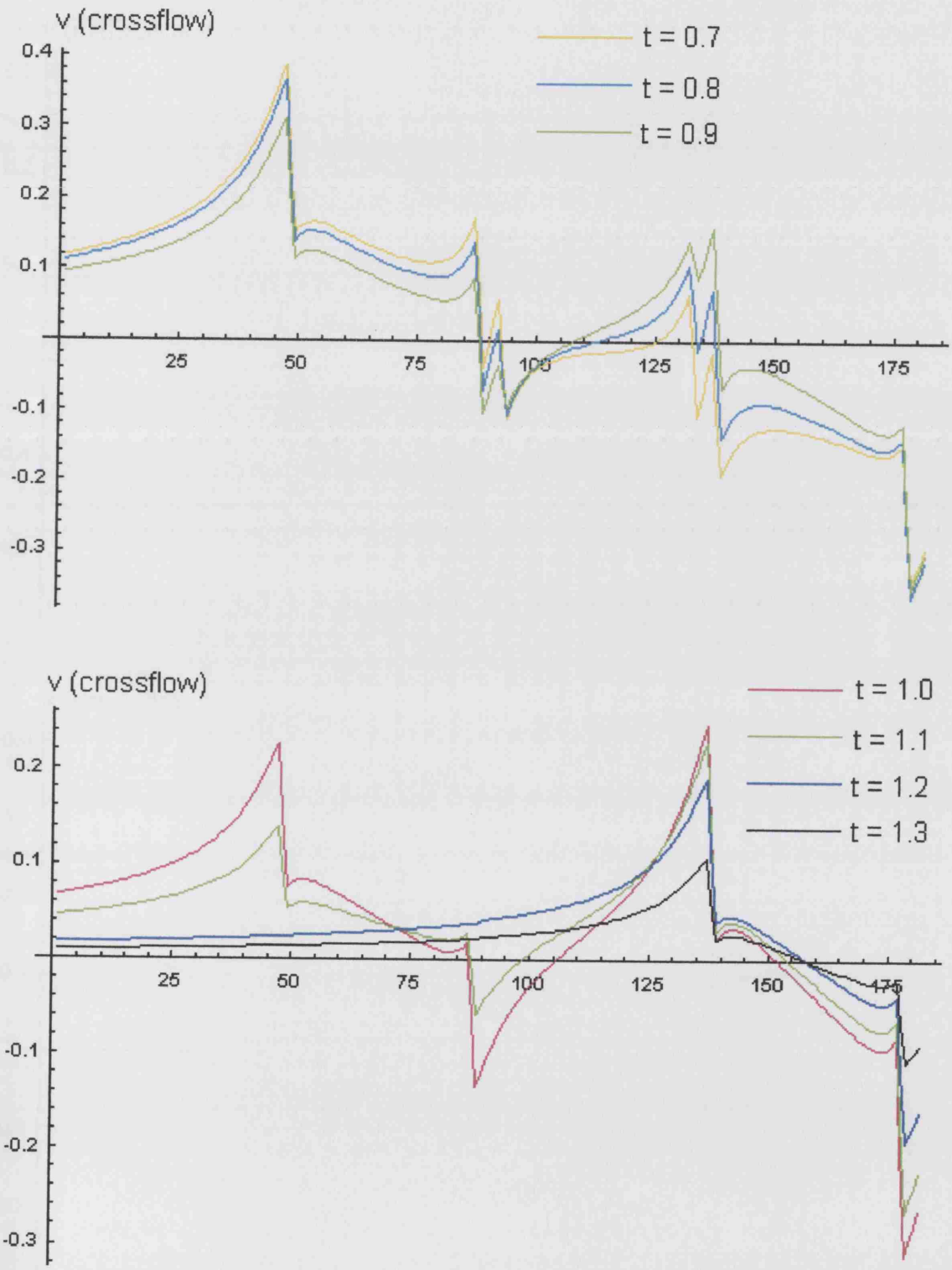

Figure B.2: 4x1mm jets separated by 0.5mm gaps. Jets 3, 2, 4 fired at t = 0, t = 0.2 and t = 0.5, respectively (illustration from t = 0.6 to t = 1.3).

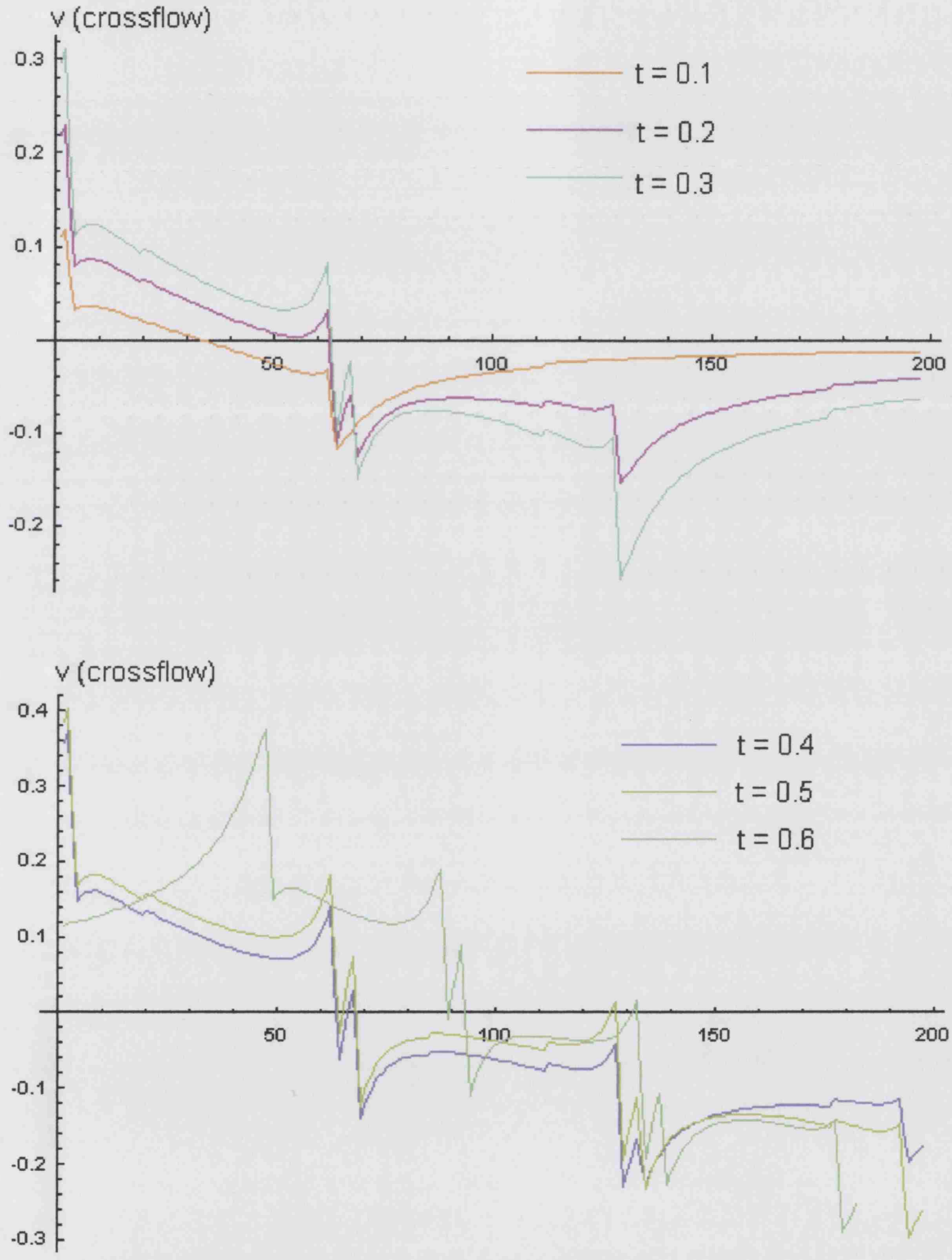

Figure B.3: 6x1mm jets separated by 0.5mm gaps. Jets 1, 2, 3 fired at t = 0, t = 0.1 and t = 0.3, respectively (illustration up to t = 0.6).

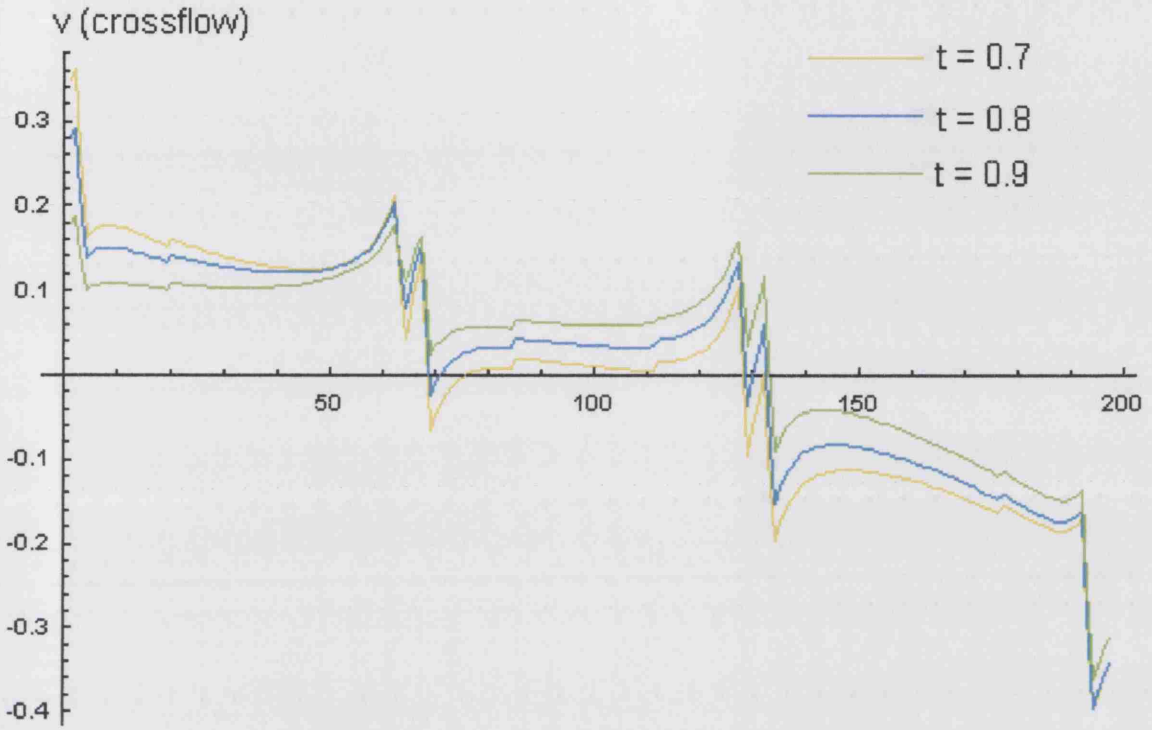

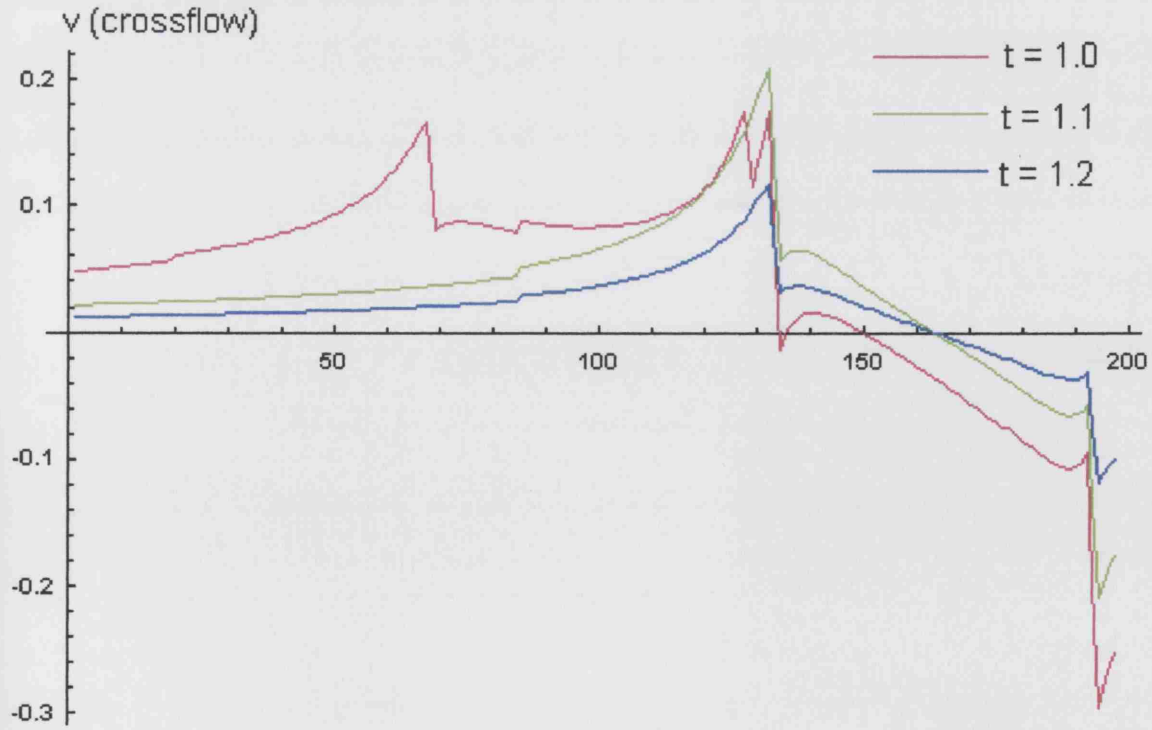

Figure B.4: 6x1mm jets separated by 0.5mm gaps. Jets 1, 2, 3 fired at t = 0, t = 0.1 and t = 0.3, respectively (illustration from t = 0.6 to t = 1.2).

Bibliography

[1] Douglas, J. F., Gasiorek, J. M. & Swaffield, J. A. *(2000) Fluid Mechanics* (fourth edition). Prentice Hall.

[2] Neve, R. S., Nelson, R. & Kotsiopoulos, P. *(1981) The drag force on spheres in thin jets.* **J. Fluid Mech.**, Vol 107, pp. 521-531.

[3] Neve, R. S. & Kotsiopoulos, P. *(1980)* **Aeronautical Journal.** November 1980.

[4] Fox, R. W. & McDonald, A. T. *(1985)* **Introduction to Fluid Mechanics** (third edition). Wiley.

[5] Reynolds, O. *(1883) 'On the Experimental Investigation of the Circumstances Which Determine Whether the Motion of Water Shall be Direct or Sinus, and the Law of Resistance in Parallel Channels.* **Phil. Trans. Roy. Soc.** , Vol 174, pp. 935-982.

[6, pp 112] Tritton, D. J. *(1977) Physical Fluid Dynamics.* Van Nostrand Reinhold.

[7] Smith, F. T. *(1979) Laminar flow of an incompressible fluid past a bluff body: the separation, reattachment, eddy properties and drag.* **J. Fluid Mech.**, Vol 92, part 1, pp. 171-205.

[8] Wu, J. C. *(1961) On the Finite Difference Solution of Boundary Layer Problems.* **Proc 1961 Heat Transfer & Fluid mech. Inst**, pp. 55-69.

[9] Smith, F. T. *(2002) Interference and turning of in-parallel wakes.* **Q. Jl Mech. Appl. Math.**, Vol 55 (1), pp. 49-67.

[10] White, F. M. *(1991) Viscous Fluid Flow* (second edition). McGraw-Hill International Editions.

[11] Acheson, D. J. *(1998) Elementary Fluid Dynamics* Oxford Applied Mathematics and Computing Science Series, Oxford University Press.

[12] Pozrikidis, C. *(2001) Fluid Dynamics Theory, Computation, and Numerical Simulation.* Kluwer Academic Publishers.

[13] Tritton, D. J. *(1977) Physical Fluid Dynamics.* Van Nostrand Reinhold.

[14, pp 304] Batchelor, G. K. *(1967) An Introduction to fluid Dynamics.* Cambridge University Press.

[15, pp 344] Batchelor, G. K. *(1967) An Introduction to fluid Dynamics.* Cambridge University Press.

[16] Prandtl, L. *(1905) Verhandlungen des III Internationalen Mathematiker Kongresses, Leipzig* 1904. pp. 484-91.

[17] Cebeci, T. & Bradshaw. *(1977) Momentum Transfer in Boundary Layers.* McGraw Hill.

[18, pp298] Birkhoff, G. & Zarantonello, E. H. *(1957) Jets, Wakes and Cavities.* Academic Press Inc, New York.

[19] Smith, F. T. *(1999) Modelling Air Flow Through An Ejector Duct.* A report to Sortex Ltd.

[20] Smith, F. T. *(2000) Air Flow Pulsing Through An Ejector Duct.* A second report to Sortex Ltd.

[21] Bowles, R. G. A. & Smith, F. T. *(2000). Interactive flow past multiple blades and wakes.***Q. Jl Mech. Appl. Math.**, Vol 53, pp. 207-251.

[22] Wilson, P. L. *(2003). On the Core Flow and Turbulent Boundary Layer in a Curved Duct,* PhD Thesis, University of London.

[23] Schlichting, H. *(1960). Boundary Layer Theory* (fourth edition). McGraw-Hill.

[24] Bickley, W.G. *(1937) Phil. Mag. 23,* pp. 727-31.

[25] Schlichting, H. *(1933). ZaMM 13,* pp. 260-3.

[26] DuChateau, P. & Zachmann, D.W. *(1986) Schaum's Outlines: Partial Differential Equations.* McGraw-Hill.

[27] Smith, F. T. & Li, L. *(2001). Swirl-flow effects in a duct bending through a substantial angle.* **Jl of Engineering Mathematics**, Vol 43, pp 315-346.

[28] Smith, F. T. & Tadjfar, M. *(2004). Direct simulation and modelling of basic three-dimensional bifurcating tube flows.* **J. Fluid Mech (2004),** Vol 519, pp 1-32.

[29] Caro, C. G., Doorly, D. J. et al. *(1996). Non-planar curvature and branching of arteries and non-planar type flow.* **Proc. R. Soc. London,** A452 (1996) 185-197.

[30] ESM Ltd *(1997). Good Processing Practice Using Colour Sorting.* **Food Technology Europe,** October 1997.

[31] Norris, K. H. *(1958). Measuring light transmittance properties of agricultural commodities.* **Agricultural Engineering,** pp. 640 - 643.

[32] Schaub, W. *(1965). Electronic colour sorting.* **Industrial Electronics,** pp. 462 - 464.

[33] Neve, R. S. *(1985). Particle deflection using air jets.* **Trans Inst M C,** Vol 7, No 1, Jan - Mar 1985.

[34] Neve, R. S. *(1999). CFD Analysis of Jets in Sorting Machines.* **An initial report to Sortex Ltd,** March 1999.

[35] Neve, R. S. *(1999). CFD Analysis of Jets in Sorting Machines.* **Report No. 2 to Sortex Ltd,** May 1999.

[36] Patankar, S. V. *(1980) Numerical Heat transfer and Fluid Flow.* Hemisphere, New York.

[37] Roache, P. J. *(1982) Computational Fluid Dynamics* (Revised Edition). Hermosa Publishers.

[38] Marsh, Adric. *(2003) Personal communication regarding Sortex physical test data.* May 2003.

[39] Caine, Steven. *(2003) Personal communication regarding Sortex physical test data.* December 2003.

[40] Neve, R. S. & Shansonga, T. *(1989). The effects of turbulence characteristics on sphere drag.* **Int. J. Heat and Fluid Flow**, Vol 10, No 4, December 1989.

[41] Neve, R. S. *(1986). The importance of turbulence macroscale in determining the drag coefficient of spheres.* **Int. J. Heat and Fluid Flow**, Vol 7, No 1, March 1986.

[42] Neve, R. S. & Jaafar, F. B. *The effects of turbulence and surface roughness on the drag of spheres in thin jets.* **The Aeronautical Journal of The Royal Aeronautical Society**, November 1982.

[43, pp 39-73] George, W. K. & Arndt, R.*(1989) Advances in Turbulence.* Hemisphere, New York.

[44] Mathieu, J. & Scott, J. *(2000) An Introduction to Turbulent Flow.* Cambridge University Press.

[45] Oakley, Matthew *(2003) Kepler Product Trajectory Prediction Report.* Sortex Ltd, December 2003.

[46] Marsh, Nick *(2004) Kepler Trajectory Prediction Update.* Sortex Ltd, February 2004.

[47] Marsh, Nick *(2004) Kepler Trajectory Prediction Results.* Sortex Ltd, April 2004.

[48] Goldstein, S. *(1938) Modern developments in fluid dynamics.* Oxford, Clarendon Press, 1938.

[49] McNown, S. S. & Yih, C. S.(editors)*(1953) Free-streamline analyses of transition flow and jet deflection,* State Univ. Iowa Studies in Eng., Bull. 35 (1953).

[50] Sobey, I. J. *(2000) Introduction to Interactive Boundary Layer Theory.* Oxford Applied and Enginering Mathematics. Oxford University Press.